Exploring the transport properties of the three-dimensional topological insulator material HgTe

Dissertation zur Erlangung des naturwissenschaftlichen Doktorgrades der Julius-Maximilians-Universität Würzburg

vorgelegt von

Cornelius Thienel
aus Tübingen

Würzburg, 2014

Eingereicht am: ....
bei der Fakultät für Physik und Astronomie

1. Gutachter: Prof. Dr. Hartmut Buhmann
2. Gutachter: Prof. Dr. Ralph Claessen
3. Gutachter: ....
der Dissertation

Vorsitzende(r): ....

1. Prüfer: Prof. Dr. Hartmut Buhmann
2. Prüfer: Prof. Dr. Ralph Claessen
3. Prüfer: ....
im Promotionskolloquium

Tag des Promotionskolloquiums: ....

Doktorurkunde ausgehändigt am: ....

True, This! -
Beneath the rule of men entirely great
The pen is mightier than the sword. Behold
The arch-enchanters wand! - itself is nothing! -
But taking sorcery from the master-hand
To paralyse the Caesars, and to strike
The loud earth breathless! - Take away the sword -
States can be saved without it!

Richelieu; Or the Conspiracy, Act II, Scene II.
Edward Bulwer-Lytton, 1839

Table of contents

List of abbreviations **7**

1. Introduction **9**

2. Properties of HgTe **13**
2.1. Band structure 14
2.2. Topological surface states 16

3. Manipulating the density in topological surface states **21**
3.1. Odd integer QHE 22
3.2. Subsets of Landau levels and gate influence 26
3.3. Hall quantization 32
3.4. Berry phase 36
3.5. Modelling the DOS of a two Dirac cone system 38

4. p-type transport in 3D HgTe **41**
4.1. Transiting the CNP 41
4.2. Improved layer structure: buffer and cap 47
4.3. Ambipolar QHE 49
4.4. Three carrier behaviour 64

5. Back gate measurements **83**
5.1. Top gate - back gate map 85
5.2. Higher magnetic fields 90

6. Surface Landau level spectrum and in-plane magnetic field **93**
6.1. Hall resistance for rotated sample 93
6.2. Isotropic Zeeman contribution 95

Summary **99**

Zusammenfassung **103**

A. Sample overview **107**

B. Mathematica code **109**
B.1. DOS calculation 109
B.2. Hall conductivity in rotated magnetic field 112

Bibliography 115

List of abbreviations

2D	Two-dimensional
2DEG	Two-dimensional electron gas
3D	Three-dimensional
ARPES	Angle-resolved photoemission spectroscopy
CNP	Charge neutrality point
DOS	Density of states
HFML	High field magnet laboratory
MBE	Molecular beam epitaxy
QHE	Quantum Hall effect
QSH	Quantum spin Hall
SdH	Shubnikov de Haas
TI	Topological insulator

1. Introduction

The basic interest of physics is to understand nature. This means not only to describe processes and substances, but also to be able to predict the outcome of possible experiments. In the field of condensed matter physics there exist very many different materials with an incredible variety of magnetic and electric properties. To be able to describe and predict the behaviour of these solids, standardized experiments can be carried out and the materials can be attributed to different categories. An example is the measurement of the electrical conductivity. By applying a voltage to a slab of a given material and probing the resulting current flow, the conductance can be determined. However, this physical quantity scales with the cross section and the length of the slab. Only when taking into account the geometrical dimensions, the conductivity as a material specific parameter is obtained. Utilizing this number, one easily identifies good conductors (metals) and poor conductors (insulators).
It turned out early that a third class of material exists, when M. Faraday discovered the conductivity of silver sulfide to strongly depend on temperature in 1833 (see Ref. [FT22], p.44). In detail he reports an increase of conductivity, when heating the specimen in his hand or with a lamp, in contrast to the temperature dependence known for metals. This temperature dependence of the conductivity is a feature of a third material class called semiconductors. For this class the number of charge carriers and with it the conductivity changes not only with temperature, but also with the purity of the specimen. Nowadays the impurity concentration in semiconductor materials can be controlled very precisely, such that intentional doping is well-established. In electronic devices semiconductors are inevitable, since transistors, the basic elements to perform logical operations, can be constructed in an integrated way from these materials.
To explain the electric properties of solids, the band structure, a description of all possible electron energies, is of fundamental importance. Especially the relation between energy gaps and the Fermi energy determines the attribution to one

of the material classes metal, insulator and semiconductor. This thesis deals with another material class named TIs that has been discovered recently. It is investigated, how the compound material HgTe can be identified as a representative of this class by the means of transport experiments. In this special material the large atomic weight of the mercury atoms leads to an irregular arrangement of bands. The reason are relativistic corrections to the electron energies some of which get large for high proton number ($Z = 80$ for Hg). Furthermore, due to its band structure, HgTe exactly represents the border between metals and semiconductors. Thus, an experimentally controlled crossover between three different material classes is possible, which makes HgTe interesting for a variety of experiments. The band structure of HgTe and the influence of strain is discussed in Ch. 2 of this thesis.
Soon after the discovery of the QSHE, that confirmed HgTe quantum wells to be the first experimental realization of a TI [KWB+07], attention was devoted to the extension of the concept to three dimensions. Evidence for the existence of topological states at the surface of a bulk crystal was found in an ARPES experiment on $Bi_{0.9}Sb_{0.1}$ by the authors of Ref. [HQW+08]. In the data the graphene-like linear dispersion of the surface states is confirmed. Indeed, comparing the surface of a TI to a monolayer of graphene, the band structure (for small momentum k) is similar. However, the Dirac cone of a TI surface state shows no degeneracy and the spin is oriented perpendicular to the momentum (see [HXW+09]). Naturally, this rises the question, if the signatures of Dirac fermions can also be identified in transport through TI surface states. The most considerable observation in graphene is that the ambipolar QHE plateau sequence is shifted by 1/2. Interestingly, the QHE from the surface of strained HgTe could be shown in 2011 [BLN+11a]. However, the influence of Dirac physics could not be demonstrated unambiguously, since the reported device was not equipped with a gate electrode. In this thesis the influence of gates on the properties of TI devices is investigated in detail.
In the condensed matter community manifold experiments are proposed to utilize the unique TI band structure and spin peculiarities. A famous example is related to the formation of Majorana fermions at the edge of TI-superconductor junctions. Controlling the superconductor phases in a trijunction device, these exotic quasi-particles could be confined in the center of the device [FK08]. The Majorana bound states are expected to show statistics different from fermions and bosons, i. e. an interchange of two identical particles would create a global phase factor $\neq \pm 1$. A quantum computer with high fault tolerance on the base of these Majorana bound states is proposed in [Kit03]. Other ideas want to make direct use of the spin momentum locking in Dirac surface states. To make HgTe available for

these kinds of applications, a substantial basic knowledge is required. This thesis contributes to the understanding of fundamental properties of HgTe as a 3D TI. Strained HgTe has a small band gap of the order of 20 meV. Therefore, one has to ask for the role of this gap in transport experiments. Since the features observed in HgTe transport devices are not yet understood to all detail, the present thesis tries to cover different possible explanations for a variety of observed features. In this sense the influence of top and back gate electrodes to low temperature transport is investigated. Magnetic fields up to $B = 30\,\mathrm{T}$ are applied in different orientations to probe the properties of HgTe devices. The effect of protective capping layers covering the HgTe interfaces is utilized to enable the demonstration of QHE features, that could not be observed for TI devices before.

2. Properties of HgTe

This chapter deals with the inverted band structure of HgTe and the ways to form a TI out of it. Two concepts of forming a TI were given in the past years. One regards the 2D TI with QSH edge states [BHZ06], while the second predicts a 3D TI [FK07]. Both concepts have in common, that a symmetry of the system has to be broken to open an energy gap and thereby provide the insulating properties of the bulk for a TI. Forming a quantum well, the translational symmetry is broken in growth direction and quantum mechanical confinement leads to reorganisation of the energy spectrum. In the proposal for 3D TIs the crystal symmetry is reduced to open a gap in the energy band scheme.
A milestone in the TI research field was the detection of the proposed QSH effect in HgTe quantum wells [KWB+07]. In carefully designed samples it could be demonstrated that the conduction is suppressed in the bulk of the 2D structure, while a pair of channels at the sample edge remains conducting. This was the first experimental realization of a (2D) TI. The concept of topology in semiconductor physics can also be used to explain the integer quantum Hall effect, discovered in 1980 [KDP80]. Thouless et al. derived a topological invariant, the Chern number, that explains the quantized Hall conductance for a Fermi energy between two Landau levels [TKNdN82]. In the case of QSH insulators a similar calculation can be done to classify them and to distinguish them from trivial insulators. The term "topological insulator" refers to the latter classification concept.
Also the 3D manifestation of the TI state could be realized experimentally by the authors of Ref. [BLN+11a]. Pronounced quantum Hall plateaus were identified as the transport response of the surfaces of strained HgTe. Since the present thesis concentrates on HgTe as a 3D TI, the formation of the TI state by imposing strain on the HgTe is presented here. The unique features are depicted, that are expected for 3D TI surface states.

2.1. Band structure

HgTe is a semimetal, i.e. conduction band and valence band are touching each other and there is no band gap between them. Due to the use in semiconductor physics one still wants to define a band gap as the energy difference $\Delta E = E_{\Gamma_6} - E_{\Gamma_8}$ at the Γ point ($k = 0$), which describes the fundamental gap for conventional direct semiconductors like GaAs. How these bands disperse for HgTe, can be seen in Fig. 2.1, where the detailed band structure is displayed, which was investigated by [CWC+72]. One notices that the bands with Γ_8-symmetry form the conductance and valence band in HgTe. Fig. 2.1 also reveals that ΔE for this material yields a negative number. If we ask the question if a given material is a

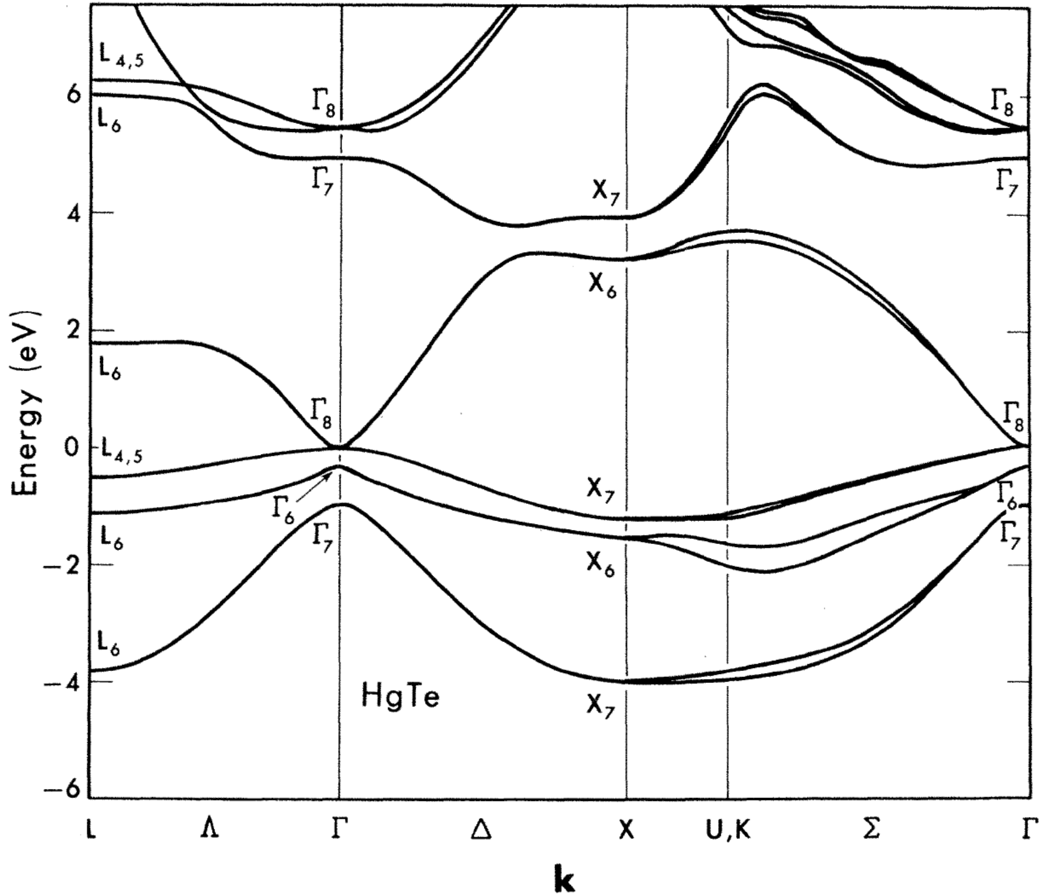

Fig. 2.1.: The inverted band structure of HgTe: The Γ_6 band lies lower in energy than the Γ_8 bands. At the position of the Fermi energy (0 eV) the Γ_8 bands touch, which makes HgTe a semimetal. Picture taken from [CWC+72].

TI, this inversion of two bands with respect to trivial materials is one prerequisite. In addition, there must be a gap in the band structure [FK07]. The latter can be achieved by applying strain to the HgTe as described in [BP74], where a gap opening between the degenerate Γ_8-bands is demonstrated. The effect of strain on Γ_8 and Γ_7 bands is schematically shown in Fig. 2.2. In the experiment, uniaxial strain is hard to achieve, but a gap opening is possible via growing the layer by MBE fully strained onto CdTe [BLN+11a], which has a lattice constant of $a_{\mathrm{CdTe}} = 0.6482\,\mathrm{nm}$. According to its lattice constant $a_{\mathrm{HgTe}} = 0.6462\,\mathrm{nm}$ (both lattice constants taken from [MDF11]) a lattice mismatch of $\epsilon = 0.3\%$ is created in the HgTe layer. In the zinc blende type HgTe grown on (001)-oriented CdTe the strain parameters will then be $\epsilon_{xx} = \epsilon_{yy} = \epsilon$ and in growth direction the strain ϵ_{zz} can be calculated using stiffness constants C_{11} and C_{12}. Because shear components of the strain tensor are zero and we are considering a cubic system, Hooke's law in the Voigt notation can be rearranged to the form ([Nye57]):

$$\sigma = \mathbf{C} \cdot \epsilon = \begin{pmatrix} C_{11} & C_{12} & C_{12} \\ C_{12} & C_{11} & C_{12} \\ C_{12} & C_{12} & C_{11} \end{pmatrix} \cdot \begin{pmatrix} \epsilon_{xx} \\ \epsilon_{yy} \\ \epsilon_{zz} \end{pmatrix} . \tag{2.1}$$

Because there is no stress in growth direction, for the third component of σ one finds

$$\sigma_3 = C_{12}\epsilon_{xx} + C_{12}\epsilon_{yy} + C_{11}\epsilon_{zz} = 0, \tag{2.2}$$

which using $\epsilon_{xx} = \epsilon_{yy} = \epsilon$ leads to

$$\epsilon_{zz} = -2\epsilon \frac{C_{12}}{C_{11}} . \tag{2.3}$$

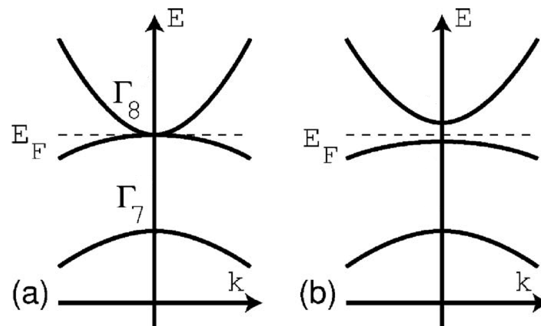

Fig. 2.2.: Schematics describing the change of the bands originating from p-orbitals at the Γ-point for (a) unstrained and (b) uniaxially strained HgTe. Taken from [FK07] and edited.

Knowing all non-zero strain components, one can estimate the gap opening between the Γ_8-bands by the formula [BP74]:

$$\delta E_{\mathrm{l,h}} = E_{\mathrm{l}} - E_{\mathrm{h}} = 2\,|b\,(\epsilon_{zz} - \epsilon_{xx})\,| = 2\,|b\,\epsilon\left(2\frac{C_{12}}{C_{11}} + 1\right)| \tag{2.4}$$

with the uniaxial deformation potential b and the energies of the light- and heavy-hole Γ_8-band edges $E_{\mathrm{l/h}}$ at the Γ-point. The numerical values are $b = 1.5\mathrm{V}$ [TOT79], $C_{11} = 59.7\,\mathrm{GPa}$ and $C_{12} = 41.5\,\mathrm{GPa}$ (values extrapolated to $0\,\mathrm{K}$, see [CS75]). Using these values and equation 2.4 one estimates a strain induced band gap of $\delta E_{\mathrm{l,h}} = 22\,\mathrm{meV}$ at the Γ-point (agreeing with [BLN+11a]). This gap is conceptually sufficiently large to position the Fermi energy in the gap and to achieve transport through the surface states of the TI only. However, with the calculation regarding only the gap at the Γ-point, it cannot be excluded that the system forms an indirect gap which is considerably smaller than the $\delta E_{\mathrm{l,h}}$ calculated above. The question, in which energy range pure surface transport can be achieved, will be discussed in this thesis on the basis of gate dependent magneto-transport measurements.

2.2. Topological surface states

As shown above, the band structure of HgTe is special in the way, that the energy gap $\Delta E = E_{\Gamma_6} - E_{\Gamma_8} < 0$ for $k = 0$. The reason is the large mass of the Hg atoms which leads to strong relativistic corrections in the energy spectrum. For many other materials including conventional semiconductors such as CdTe and $\mathrm{Hg}_{1-x}\mathrm{Cd}_x\mathrm{Te}$ with $x = 0.68$ and also for vacuum the band order is different and one finds $\Delta E > 0$. Naturally, if an interface of two materials with $\Delta E_1 \cdot \Delta E_2 < 0$ is established, there is a continuous connection of each band and a crossing takes place at the interface. This circumstance was recognized first by Chang et al. [CSB+85] and later O. A. Pankratov stated: "*[...] the basic feature of a band-inverted heterojunction [...] is the presence of spin-non-degenerate electron interface states with a linear dispersion law*"[Pan90].

For the example of a HgTe/CdTe layer sequence the band behaviour is sketched in Fig. 2.3. With the displayed Fermi energy the HgTe is insulating due to the

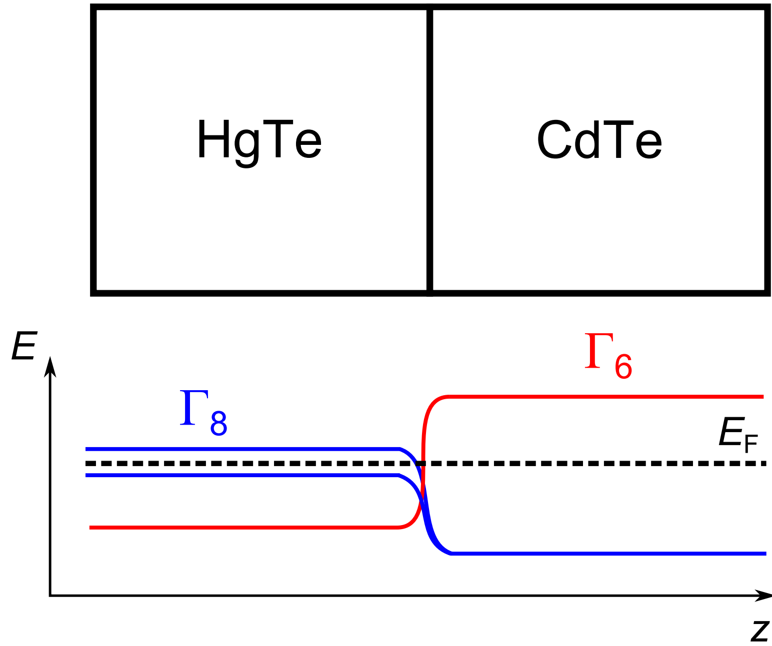

Fig. 2.3.: Sketch of the band behaviour at a HgTe/CdTe interface. The Fermi energy E_{F} can be placed inside the strain induced gap in the HgTe region and necessarily cuts bands at the interface leading to conducting surface states.

band gap $\delta E_{\mathrm{l,h}}$ whereas at the interface one obtains a conducting state. A more accurate substantiation of the existence of surface states in strong TIs is given for example in [HK10]. The Hamiltonian describing the surface state is:

$$H_{\mathrm{surface}} = -i\hbar v_{\mathrm{F}} \vec{\sigma} \cdot \vec{\nabla}, \tag{2.5}$$

with the Fermi velocity v_{F} and spin matrix $\vec{\sigma}$. The energy spectrum obtained from this Hamiltonian is the so called Dirac cone with the energy of the surface state $E_s \propto |k_{\|}|$. Here, the momentum $k_{\|}$ lies in the plane of the interface between the TI and the trivial insulator.

To discuss the energy spectrum in a magnetic field, a HgTe slab is considered, of which two surfaces are penetrated by the magnetic field $\vec{B} = B \cdot \hat{e_z}$, that defines the z-direction. The Hamiltonian and its solution are given in Ref. [BLN+11b]. In the basis $|\beta, \sigma\rangle$, where $\beta = 1, 2$ describes the two relevant surface states (perpendicular to the magnetic field) and $\sigma = \uparrow, \downarrow$ represents the spin, the Hamiltonian can be described as

$$H_{2D} = \hbar v_F \begin{pmatrix} k_x\,\sigma_y - k_y\,\sigma_x & 0 \\ 0 & -(k_x\,\sigma_y - k_y\,\sigma_x) \end{pmatrix}. \tag{2.6}$$

The eigen-energies of this basic problem are found to be

$$E_\beta^N = \pm\sqrt{2e\hbar v_F^2 BN}\,, \tag{2.7}$$

with the Landau level index $N = 1, 2, 3...$ and $E_\beta^0 = 0$. The result is independent of β and thus valid also for a single Dirac cone. In the two Dirac cone model the levels are doubly degenerate as long as no energy difference between the surface states is introduced.

We now additionally want to consider the Zeeman effect for the given model. The Hamiltonian for a magnetic field in z-direction according to Ref. [BLN$^+$11b] reads

$$H_Z = \begin{pmatrix} g^*\mu_B B\sigma_z & 0 \\ 0 & g^*\mu_B B\sigma_z \end{pmatrix}, \tag{2.8}$$

with an effective g-factor g^* and the Bohr magneton μ_B. The eigen-energies of the combined Hamiltonian $H = H_{2D} + H_Z$, calculated by the authors of Ref. [BLN$^+$11b], are

$$E_\beta^N = \pm\sqrt{2e\hbar v_F^2 BN + (g^*\mu_B B)^2}\,, \tag{2.9}$$

valid for $|N| > 0$. For $N = 0$ the result is $E_\beta^0 = -g^*\mu_B B$. The spectrum including the Zeeman energy is thus still independent of β indicating, that the top and bottom energy states are degenerate. To lift this degeneracy of the $\beta = 1, 2$ states, an energy difference $\delta = E_1^N(B = 0) - E_2^N(B = 0)$ between top and bottom state is needed. Such a difference is expected in the experiment due to different electrostatic environments of the two surfaces. The result is shown in Fig. 2.4, where the energy of the Landau levels with $-2 < N < 2$ is plotted vs. the magnetic field. The parameters for the plot are $v_F = 5 \cdot 10^5$ m/s and $g^* = 20$. Furthermore the energy shift has been chosen to be $\delta = 12.5$ meV. It is reasonable, that this

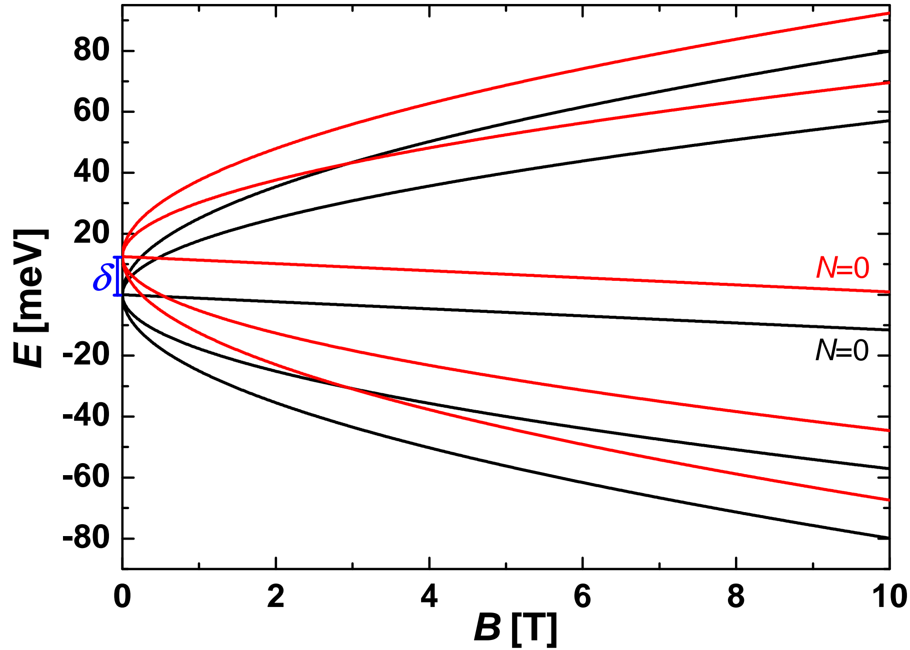

Fig. 2.4.: Landau level dispersion for two Dirac cones in a magnetic field. Only the levels with $-2 < N < 2$ are plotted. A constant energy shift of $\delta = 12.5\,\mathrm{meV}$ accounting for the different electrostatic environments of the surfaces lifts the degeneracy.

energy shift can be manipulated by gate electrodes close to the surfaces. However, for constant potentials in the system one finds that δ is constant in magnetic field, and the zero levels of top and bottom surface both exhibit identical slope $\partial E^0_\beta/\partial B < 0$. In the energy region between the two zero levels, that are marked by their Landau level index $N = 0$ in Fig. 2.4, an n-type edge channel on one surface coexists with a p-type channel on the second. These considerations are utilized in Ch. 4 to discuss the observed Landau level behaviour for low quantum Hall indices. Further, the Zeeman contribution is the key ingredient to describe the shift of the spectrum due to an in-plane magnetic field in Ch. 6.

3. Manipulating the density in topological surface states

To confirm the Dirac nature of the 3D TI surface states in strained HgTe, a sample of HgTe grown on CdTe has been shaped into a Hall bar and equipped with a top gate. Using a dilution refrigerator the transport depending on the gate voltage was studied in a magnetic field. In this chapter the magneto-resistance data is presented and analysed. The focus is set on the n-conducting part of the Dirac cones of the surfaces, where well-pronounced QHE and especially a Dirac-like sequence of Hall quantization can be found.

In the presented measurements the QHE results from two subsystems, which can be substantiated by a plot of the positions of all observed Landau levels in gate voltage and magnetic field. In general, the charge carrier densities of the two subsystems are different, so that special attention has to be paid to the nomenclature of indices that define the quantum Hall state. The quantum Hall index i is used to describe the observed Hall quantization, if the entire system exhibits a plateau with Hall resistance $R_{xy} = h/(i\,e^2)$, while the quantum state of the subsystems can be specified by their individual filling factor ν, which relates the charge carrier density to the number of states available per Landau level. Furthermore, the integer Landau level index N numbers these levels in one subsystem and it is useful to also define an index j that numbers the energy gaps between the Landau levels belonging to minima in SdH sequences. All these terms have to be distinguished carefully in order to clarify the situation of QHE in Dirac systems of a 3D TI.

Concerning the quality of Hall quantization and Berry phase of the given data, the two Dirac cone interpretation is sufficient to explain many of the observed features and therefore is used to describe the sample. An indication of parallel bulk conduction is not found from this dataset. Thus a model consisting of two Dirac-like 2DEGs only is presented, which allows for the computation of a DOS pattern that follows the SdH sequences.

3.1. Odd integer QHE

The investigation of the Dirac surface states in a transport experiment is carried out first on the MBE grown material Q2424. The simple layer stack is given in Fig. 3.1. It consists of the substrate, the active HgTe layer, and is completed by a multilayer insulator consisting of alternating SiO_2 and Si_3N_4 layers and a top gate fabricated of gold. Here the thickness of the HgTe layer, $d_{\mathrm{HgTe}} = 70\,\mathrm{nm}$, is large enough to ensure 3D behaviour of the HgTe layer. An upper limit for the thickness is given by the relaxation of HgTe which is estimated to start at $d_{\mathrm{HgTe,max}} \approx 200\,\mathrm{nm}$ [BLN+11a]. A Hall bar of length $L = 600\,\mu\mathrm{m}$ and width $W = 200\,\mu\mathrm{m}$ is produced by optical lithography. Fig. 3.2 presents a micrograph of the Hall bar. The way the Hall bar is contacted is of importance here, since it is not self-evident that a given contact is connected to both upper and lower surface state. In the present case a droplet of indium is melt into the bonding pad and therefore in this area diffuses to the bottom of the HgTe layer. In this sense, both surfaces are connected at every bonding pad.

In the cryostat a magnetic field is applied perpendicular to the HgTe layer, i.e. in growth direction. Thus, of the six surface normals of the HgTe slab the two belonging to the largest areas are oriented parallel to the magnetic field. It should be mentioned that the four remaining side surfaces conceptually are conducting likewise. The Hall and longitudinal resistance data is shown in Fig. 3.3. Remarkably the data shows very pronounced quantum Hall plateaus accompanied by minima in the SdH sequence. This fact proves the existence of at least one 2D subsystem

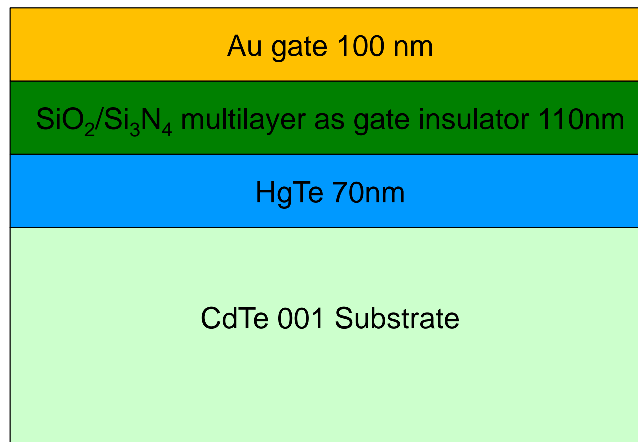

Fig. 3.1.: Layer stack of the sample Q2424. The HgTe layer is fully strained to the lattice constant of CdTe.

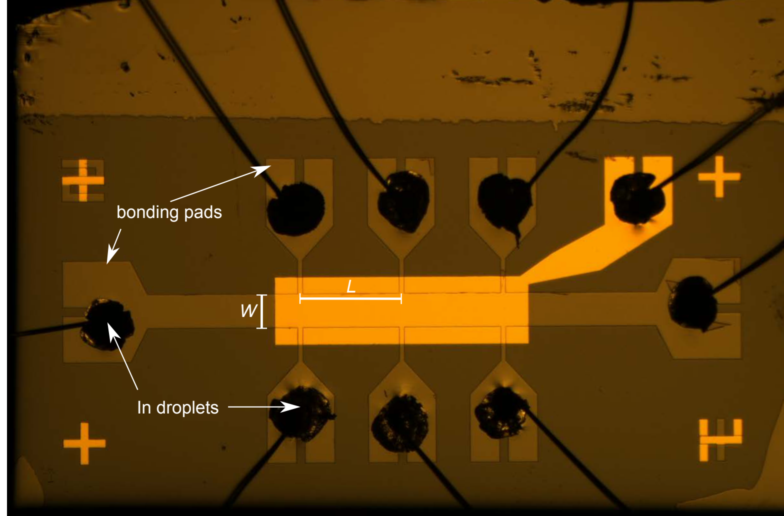

Fig. 3.2.: Optical micrograph of the Hall bar fabricated of the material Q2424. The bonding wires are glued to the bonding pads by indium which also is used to obtain ohmic contacts to the HgTe layer. It diffuses through the HgTe, why both upper and lower surface state are contacted.

in the structure. As in the reference [BLN+11a] this subsystem is interpreted to result from the topological nature of the device and to be located at the surface of the HgTe structure. This hypothesis will be examined on the basis of the transport data below. Fig. 3.3 a) shows that lowering the gate voltage increases the overall slope of the Hall trace, making Hall plateaus with smaller quantum Hall index i visible. For the gate voltage $V_\mathrm{g} = -1\,\mathrm{V}$ an odd integer plateau sequence can be observed. The Hall and SdH data of this gate voltage is plotted together in Fig. 3.4 where the dashed lines give the theoretical fractions of the von Klitzing constant $R_\mathrm{K} = h/e^2$ [KDP80] expected for an odd integer quantum Hall sequence. The red trace shows Hall plateaus for $i = 1$ and $i = 3$, while for the higher indices only indications of plateaus are visible. However, it is a clear observation, that all odd integer indices are much more pronounced than the even ones. The observed odd sequence can be understood in analogy to the extraordinary QHE in single layer graphene, where on the plateaus one finds a quantized Hall conductivity of

$$\sigma_{xy} = m(j + \frac{1}{2})\frac{e^2}{h} \; ; j = 0, \pm 1, \pm 2 \ldots \tag{3.1}$$

Here, the minimum index j is used, because it is integer for plateaus in R_{xy} (corresponding to minima in R_{xx}). For graphene a degeneracy of $m = 4$ can be observed [NGM+05]. The anomalous sequence shifted by 1/2 with respect to conventional

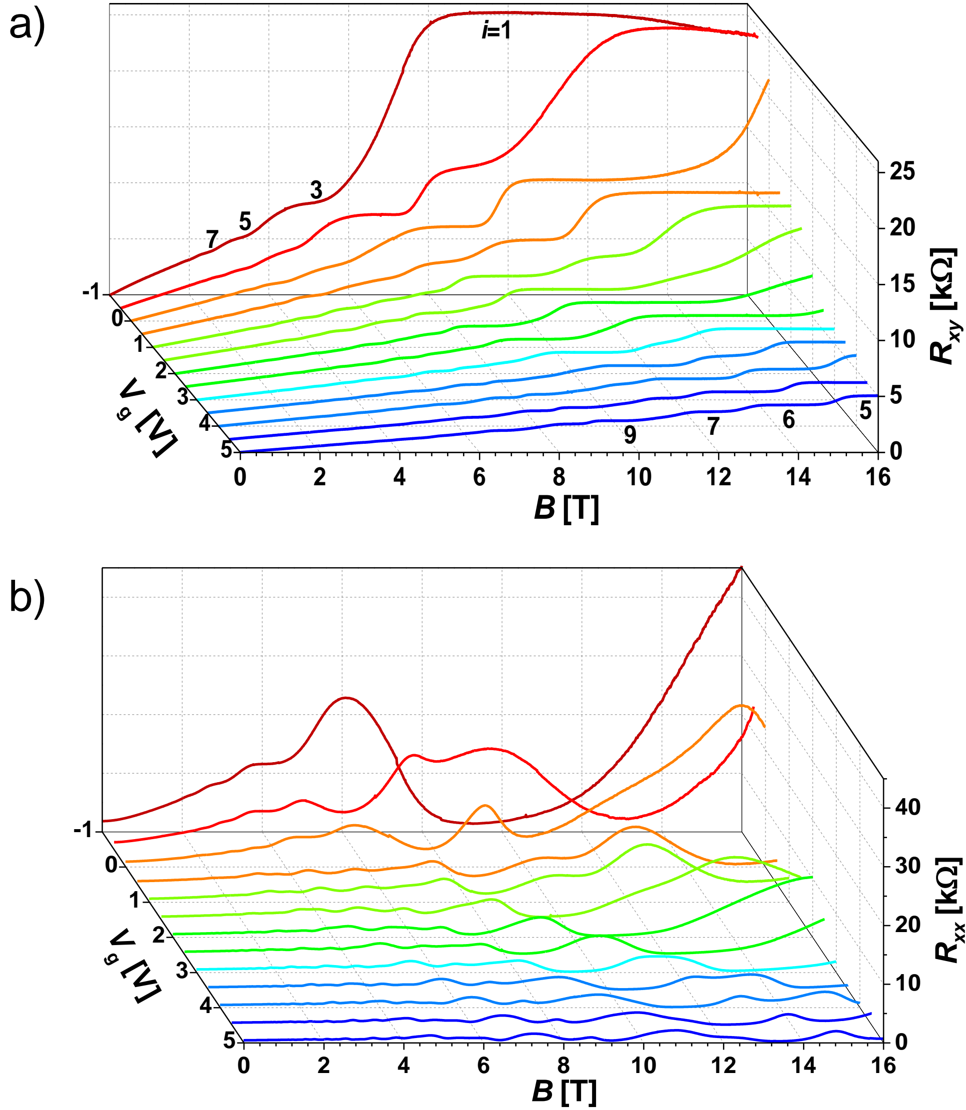

Fig. 3.3.: Magneto-resistance data for the Hall bar sample Q2424 for different gate voltages at a nominal temperature of 20 mK. a) Hall resistance of the n-region and b) corresponding longitudinal resistance. Numbers in a) denote the quantum Hall plateaus with index i. At $V_\mathrm{g} = -1\,V$ an odd integer quantum Hall sequence can be observed.

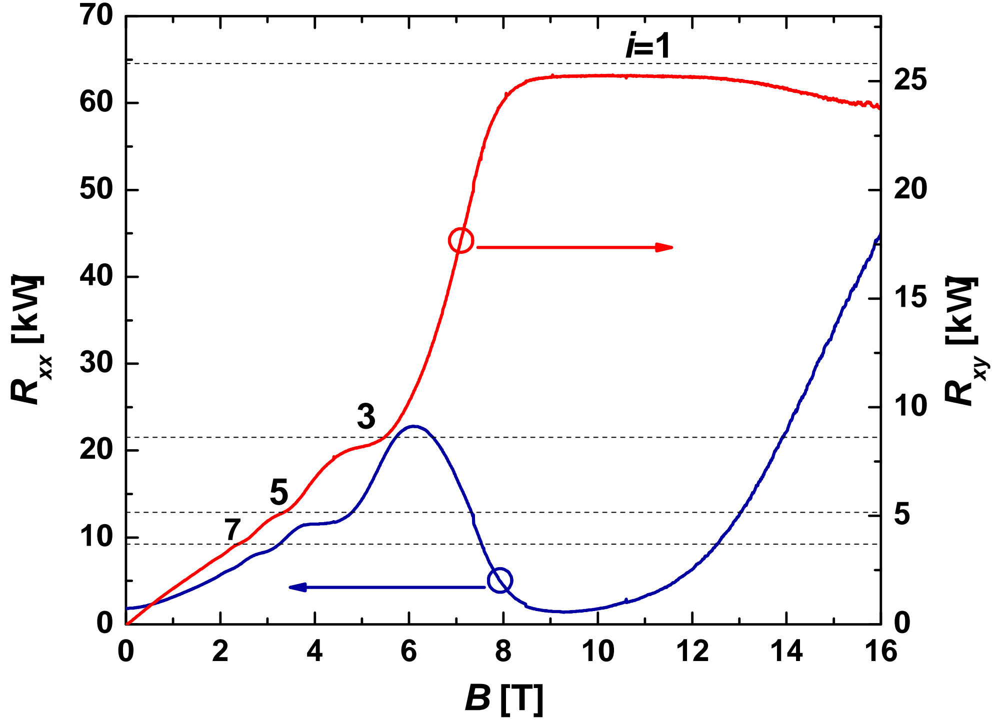

Fig. 3.4.: Hall (red) and longitudinal (blue) resistance of Q2424 for the gate voltage $V_{\mathrm{g}} = -1\,\mathrm{V}$. Numbers denote the quantum Hall index i assigned to the dashed lines. An odd integer quantum Hall sequence can be observed in the data.

quantum Hall systems can de derived from the Dirac Hamiltonian (Eq. 2.5) when using minimal coupling to the magnetic field [CPNG09]. The outcome is a Landau level at zero energy which has the same degeneracy as other Landau levels but counts half to the n- and p-conducting sequence, respectively. It also shall be mentioned here, that the integer j belonging to minima in R_{xx} does not equal the integer Landau level index N which is assigned to maxima in R_{xx} and is numbering the Landau levels. On a single surface of a TI degeneracies of valley and spin, found for graphene, are not present. However, having two surfaces perpendicular to the magnetic field one expects $m = 2$ in Eq. 3.1, if the charge carrier densities on both surfaces are equal. Assuming, that the influence of the gate electrode on top and bottom surface is different, there must be exactly one gate voltage $V_{\mathrm{g}}^{\mathrm{e}}$ for that the two densities are equal and thus an odd integer sequence of Hall plateaus develops. The Hall trace in Fig. 3.4 thus gives rise to suppose, that the corresponding gate voltage $V_{\mathrm{g}} = -1\,\mathrm{V}$ is close to $V_{\mathrm{g}}^{\mathrm{e}}$. However, taking into account the considerable broadening of the SdH trace, $V_{\mathrm{g}}^{\mathrm{e}}$ may well be shifted a bit with respect to $V_{\mathrm{g}} = -1\,\mathrm{V}$.

3.2. Subsets of Landau levels and gate influence

To obtain a rough estimate of the sample properties, one can use the Hall slope to calculate a total 2D charge carrier density n_{tot}. Together with the longitudinal resistance $R_{xx}(0\,\mathrm{T})$ one is able to find a mean mobility $\overline{\mu}$ for the system. However, an observation from Fig. 3.4 is the clearly non-linear Hall trace for low magnetic fields (see close up in Fig. 3.5). In a system with more than one carrier type, this can occur, if the mobilities of the carriers are different. This can be motivated in a simple Drude-Sommerfeld picture, where the resistivity matrices $\boldsymbol{\rho}_i$ of the individual carrier types with charge carrier density n_i (the sign of the charge is included) and mobility μ_i are given by (see for example [BvH91])

$$\boldsymbol{\rho}_i = \begin{pmatrix} \rho^i_{xx} & \rho^i_{xy} \\ \rho^i_{yx} & \rho^i_{yy} \end{pmatrix} = \begin{pmatrix} 1/\sigma_i & R_i B \\ -R_i B & 1/\sigma_i \end{pmatrix}, \tag{3.2}$$

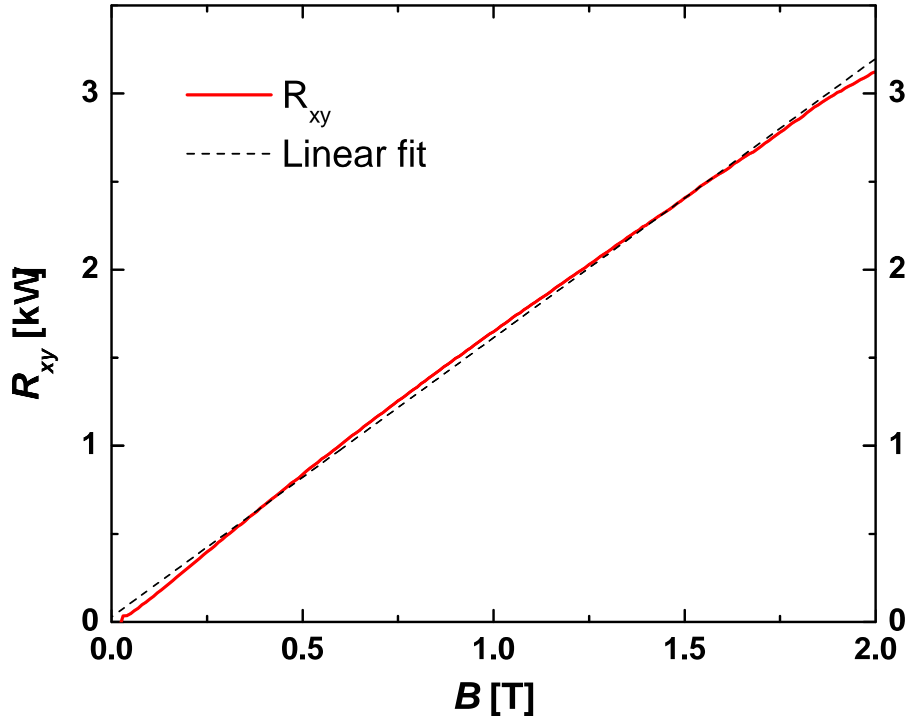

Fig. 3.5.: Close up of the Hall resistance of Q2424 for the gate voltage $V_{\mathrm{g}} = -1\,\mathrm{V}$ together with a linear fit (dashed line). The non-linearity of the Hall trace is ascribed to more than one carrier types with different mobilities.

with the Hall coefficient $R_i = 1/(n_i e)$, the longitudinal conductivity $\sigma_i = |n_i e \mu_i|$ and the magnetic field B. The total resistivity matrix is then given by

$$\boldsymbol{\rho}_{\text{tot}} = \left(\sum_i \boldsymbol{\rho}_i^{-1} \right)^{-1} . \tag{3.3}$$

If one is interested in the total Hall resistance $R_{xy} = \rho_{xy}^{\text{tot}}$ for a two carrier system, one finds from Eqns. 3.3 and 3.2

$$R_{xy} = \frac{\mu_1^2 n_1 + \mu_2^2 n_2 + \mu_1^2 \mu_2^2 (n_1 + n_2) B^2}{e((\mu_1 |n_1| + \mu_2 |n_2|)^2 + \mu_1^2 \mu_2^2 (n_1 + n_2)^2 B^2)} \cdot B. \tag{3.4}$$

Omitting the quadratic terms in B in the nominator and denominator of the fraction in this expression reproduces a standard formula for the study of semiconductors [Zim60]. However, to explain the non-linear behaviour, one has to consider the quadratic terms. Furthermore, for two n-type carrier species with $\mu_1 = \mu_2$ Eq. 3.4 yields $R_{xy} = B/(en_1 + en_2)$, which also is linear in B and does not explain the data. One therefore can conclude, that two carrier species with different mobilities must exist for the gate voltage $V_{\text{g}} = -1\,\text{V}$. This means, that a description by total density and mean mobility is useful only for rough comparisons of sample quality, but misleading for the understanding of the detailed physical properties of the 3D TI HgTe. In consequence, these quantities will be avoided as much as possible below.

To further investigate the top and bottom states, the other gate voltages are regarded. Naturally, for any voltage $V_{\text{g}} \neq V_{\text{g}}^{\text{e}}$ the densities are different and Eq. 3.1 becomes invalid for the combined system. As the Hall conductivity σ_{xy} is additive for parallel existing subsystems, one can number the minima j^{t} and j^{b} according to the carrier densities n^{t} and n^{b} in the top and bottom subsystems and finds for the plateaus of the combined system

$$\sigma_{xy} = (j^{\text{t}} + \frac{1}{2} + j^{\text{b}} + \frac{1}{2}) \frac{e^2}{h} \ ; \ j^{\text{t}}, j^{\text{b}} = 0, \pm 1, \pm 2 \ldots . \tag{3.5}$$

This equation yields a quantum Hall sequence in magnetic field, where steps of $2e^2/h$ in σ_{xy} can be generated if two Landau level positions are very close or equal

and thus j^{t} and j^{b} exhibit steps at the same B-field, but in general steps of e^2/h are expected due to transitions of only j^{t} or j^{b}.

This behaviour is observed if the gate voltage is changed to $V_{\mathrm{g}} = -0.5\,\mathrm{V}$ as displayed in Fig. 3.6. Here the positions of the maxima in the SdH sequence of the dashed line at $V_{\mathrm{g}} = -1\,\mathrm{V}$ and the measurement at $V_{\mathrm{g}} = -0.5\,\mathrm{V}$ (blue) can be compared. While for $V_{\mathrm{g}} = -1\,\mathrm{V}$ at $B = 6.1\,\mathrm{T}$ the two peaks lie on top of each other due to $n^{\mathrm{t}} = n^{\mathrm{b}}$, they have moved to larger B-values for $V_{\mathrm{g}} = -0.5\,\mathrm{V}$ according to a higher n-type carrier density. However, the two peaks have moved by different amounts in accordance with the assumption that $\partial n^{\mathrm{t}}/\partial V_{\mathrm{g}} > \partial n^{\mathrm{b}}/\partial V_{\mathrm{g}}$, because the top surface is closer to the gate (see Fig. 3.1). Furthermore one observes in Fig. 3.6 for the blue trace that the broadening of the maximum at $B = 9.4\,\mathrm{T}$ is stronger than the broadening of the one at $B = 7.5\,\mathrm{T}$. This is in agreement with the disparity of the carrier mobilities discussed above referring to Fig. 3.5. Also, stronger broadening of the peaks is correlated to a worse interface quality of the surface. Therefore one expects the maximum at $B = 9.4\,\mathrm{T}$ to belong to the top surface that after MBE growth is exposed to oxygen and chemicals, whereas the bottom interface is protected by the HgTe layer. So both observations mentioned above consistently connect this maximum to a Landau level originating from the

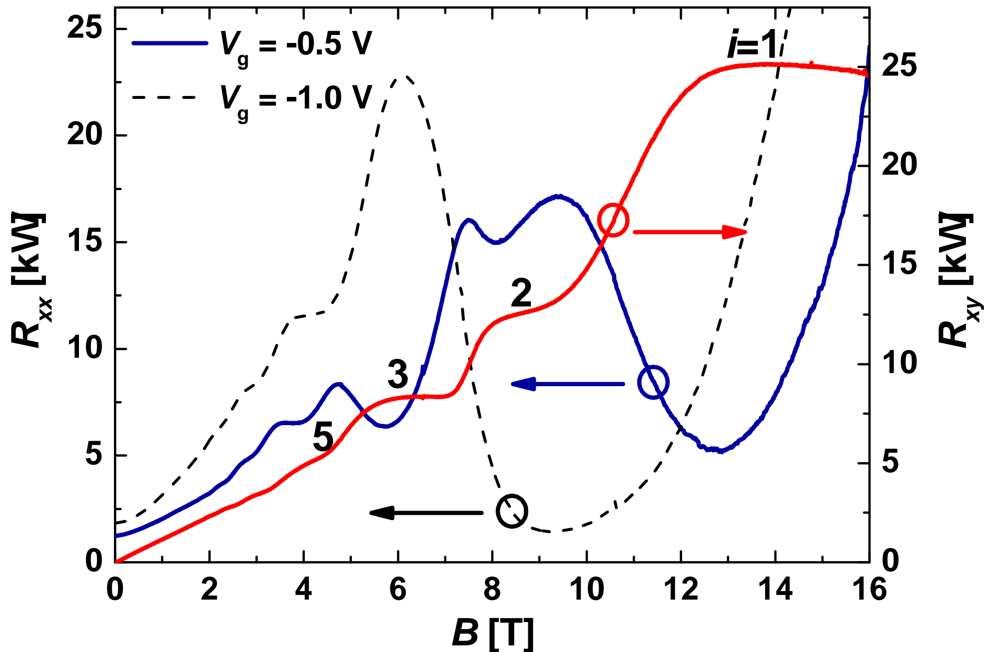

Fig. 3.6.: Hall (red) and longitudinal (blue) resistance of Q2424 for the gate voltage $V_{\mathrm{g}} = -0.5\,\mathrm{V}$. Numbers denote quantum Hall indices, the dashed line is the longitudinal resistance at $V_{\mathrm{g}} = -1\,\mathrm{V}$ for comparison.

top surface state of the HgTe Hall bar. As expected from Eq. 3.5 also the even plateau value $i = 2$ starts to become visible again in Fig. 3.6. Following the R_{xy}-traces in Fig. 3.3 a) when detuning the surface densities n^{t} and n^{b}, i.e. for increasing gate voltage, this behaviour can also be found for the $i = 4$ plateau which starts to appear at $V_{\mathrm{g}} = 0.5\,\mathrm{V}$. To further analyse the properties of Landau

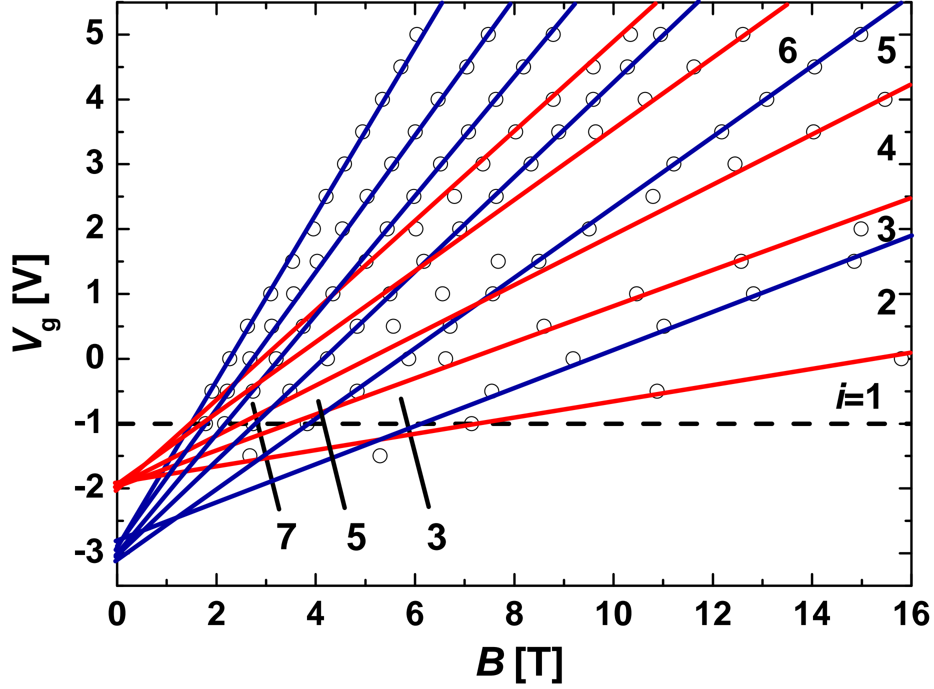

Fig. 3.7.: Open circles represent positions of Landau levels obtained by finding the maxima in $\partial R_{xy}/\partial B$. The blue and red lines correspond to two subsets of Landau levels as expected from the two surfaces perpendicular to the magnetic field. Numbers between two lines denote Hall plateaus of index i in that region.

levels in the system, the derivative $\partial R_{xy}/\partial B$ is calculated for all $R_{xy}(B)$ traces shown in Fig. 3.3 a). Transitions between Hall plateaus in R_{xy} result in maxima of the derivative $\partial R_{xy}/\partial B$ and therefore one can mark the positions of Landau levels in magnetic field and gate voltage. A plot of the Landau level positions (open circles) is shown in Fig. 3.7. These positions can be understood within a two Dirac cone model, which results from two sets of Landau levels (blue and red lines) that have different origins. The numbers give the plateau index i of Hall resistance that is found between two levels. Consequently, the dashed line at $V_{\mathrm{g}} = -1\,\mathrm{V}$ recovers the odd integer sequence.

From the level spacings estimates about the gate voltage dependence of the subsystems can be made. For a constant magnetic field B we obtain a fixed degeneracy for each Landau level and the charge per level is $n_{\mathrm{LL}} = eB/h$. Therefore the filling factor

$$\nu = \frac{n}{n_{\mathrm{LL}}} = \frac{nh}{eB} \tag{3.6}$$

grows proportional to the charge carrier density n. For a single gated 2DEG one expects to find $n \propto V_{\mathrm{g}}$, based on a simple plate capacitor model. This will result in an equal spacing of the gate voltage between adjacent Landau levels.

Landau level index N	1	2	3	4	5	6
V_{g} for red sequence / V	-1.64	-0.93	-0.10	0.68	1.35	2.26
V_{g} for blue sequence / V	-1.41	-0.84	-0.40	0.25	0.76	-

Tabelle 3.1.: Gate voltages of the Landau levels read from red and blue lines of Fig. 3.7 at a fixed magnetic field of $B = 4\,\mathrm{T}$.

To compare to a plate capacitor model, the gate voltage positions of the red and blue levels in Fig. 3.7 were determined at a fixed field of $B = 4\,\mathrm{T}$. The results are given in Tab. 3.1. Additionally, they are plotted in Fig. 3.8 against the Landau level index N together with a linear fit. A different gate influence on the two series of levels can be observed from the slopes of the straight lines. The slopes give the gate voltage ΔV_{g} needed to move the Fermi energy by one Landau level, which means that a charge n_{LL} is added to n. Using Eq. 3.6 one can calculate the change in charge carrier density Δn and thus finds the gate efficiency $\Delta n/\Delta V_{\mathrm{g}}$ at the specific magnetic field of $B = 4\,\mathrm{T}$. The red sequence of levels is associated with the top surface state (closer to the gate) because the level spacing is smaller, so one obtains the same Δn with less voltage applied. A density change $\Delta n^{\mathrm{t}}/\Delta V_{\mathrm{g}} = 1.78 \times 10^{11}\,\mathrm{V}^{-1}\mathrm{cm}^{-2}$ is computed from the slope of the red line in Fig. 3.8, while for the blue line representing the bottom surface an efficiency of $\Delta n^{\mathrm{b}}/\Delta V_{\mathrm{g}} = 1.24 \times 10^{11}\,\mathrm{V}^{-1}\mathrm{cm}^{-2}$ is found.

These numbers are now compared with the results of a simple plate capacitor

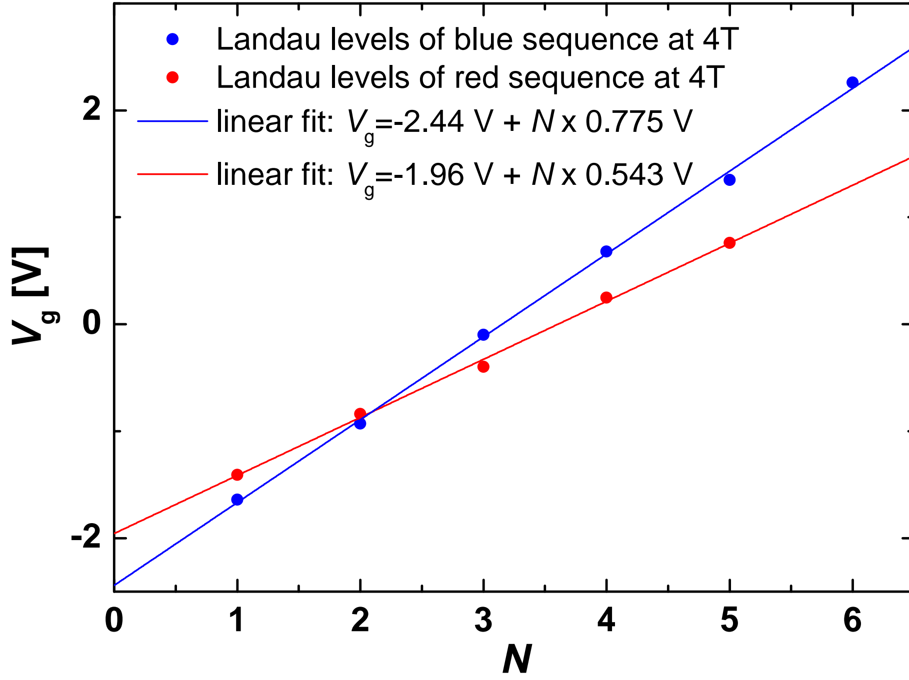

Fig. 3.8.: Gate voltage positions of Landau levels taken from Fig. 3.7 plotted against Landau level index N. The different slopes of the linear fits reflect different gate influence on the two surfaces.

model. In this model we only want to calculate the gate effect on the upper surface. The insulator consists of 11 alternating layers of SiO_2 and Si_3N_4 each of thickness $d_0 = 10\,\mathrm{nm}$ starting with SiO_2. For the total gate capacitance C_{tot} therefore one can use

$$\frac{1}{C_{\mathrm{tot}}} = \frac{6}{C_{\mathrm{SiO}}} + \frac{5}{C_{\mathrm{SiN}}} = \frac{d_0}{A\epsilon_0}\left(\frac{6}{\epsilon_{\mathrm{SiO}}} + \frac{5}{\epsilon_{\mathrm{SiN}}}\right), \tag{3.7}$$

with the capacitances of a single insulator layer C_{SiO} and C_{SiN} and the corresponding permittivities $\epsilon_{\mathrm{SiO}} = 3.9$ and $\epsilon_{\mathrm{SiN}} = 7.5$ (values taken from Ref. [KS05]). Using the capacitance C_{tot} the applied gate voltage can be translated to

$$V_{\mathrm{g}} = \frac{Q}{C_{\mathrm{tot}}} = \frac{Qd_0}{A\epsilon_0\left(\frac{6}{\epsilon_{\mathrm{SiO}}} + \frac{5}{\epsilon_{\mathrm{SiN}}}\right)} = \frac{en^{\mathrm{t}}d_0}{\epsilon_0\left(\frac{6}{\epsilon_{\mathrm{SiO}}} + \frac{5}{\epsilon_{\mathrm{SiN}}}\right)}, \tag{3.8}$$

where the charge Q imposed by the gate concentrates in the top surface. One finds a change in density $\Delta n^{\mathrm{t}}/\Delta V_{\mathrm{g}}|_{\mathrm{theo.}} = 2.51 \times 10^{11}\,\mathrm{V^{-1}cm^{-2}}$, which exceeds the

experimentally determined value. One possible explanation is a redistribution of charges between the two surfaces, which are topologically connected and might act as a single state. This could also explain the relatively large gate influence onto the lower surface. However, the dielectric constant of the insulator layer can vary depending on the layer quality and the deposition conditions. The total density change of $\Delta n_{\mathrm{tot}}/\Delta V_{\mathrm{g}} = 3.02 \times 10^{11}\,\mathrm{V}^{-1}\mathrm{cm}^{-2}$ gained from the experiment is slightly higher than the value estimated for the top surface only within the capacitor model, indicating that a small direct gate effect on the lower surface is existing.

Although the data can consistently be described by the two Dirac cone interpretation, it is a legitimate question, if there additionally are conducting bulk states present. Having in mind, that the size of the direct gap is $\approx 22\,\mathrm{meV}$, one could ask for the gate voltage range, in which the bulk carriers are not yet activated. To find answers to these questions, the quality of Hall quantization is investigated in the following section.

3.3. Hall quantization

One clear observation from Hall data is the non-perfect quantization of Hall plateaus. As a trend, most of the plateaus in Hall resistance lie below the theoretical value, while a few also exceed the expected value. In Fig. 3.9 the resistance values of the plateaus are plotted against V_{g} for the n-conducting regime. The $i = 1$ plateau is excluded in Fig. 3.9, because it is observable only for the voltages $V_{\mathrm{g}} = -1\,\mathrm{V}$ and $V_{\mathrm{g}} = -0.5\,\mathrm{V}$. Thus, the focus is set here on the stability of quantization especially at high voltages V_{g}. Analysing the quantization in Fig. 3.9, one finds, that the deviation of Hall quantization is of the order of 3% for all gate voltages (this is also valid for the $i = -1$ plateaus, see Figs. 3.4 and 3.6) and extremely stable up to the highest gate voltages investigated in the dataset.

A deviation to lower plateau values can be explained by any parallel conducting channel. If such a channel is active, a part of the current is bypassed and does not flow through the top and bottom surfaces. However, for the calculation of R_{xy} the total flow and therefore a too large current is used. With $R_{xy} = U_{xy}/I_{\mathrm{tot}}$ one finally obtains underestimated values of R_{xy}. As conduction channels parallel to

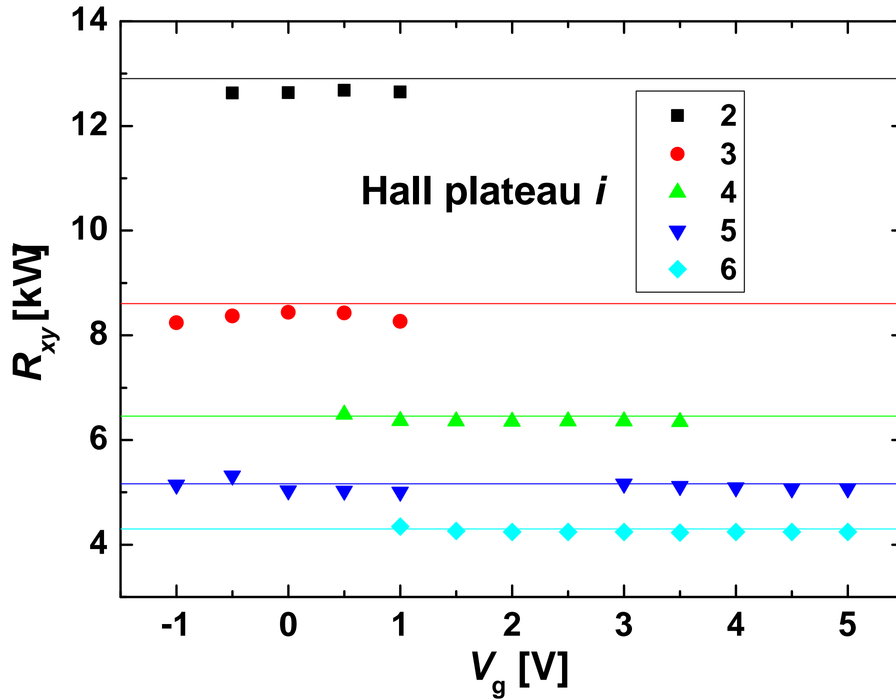

Fig. 3.9.: Plateau values of quantized Hall resistance. The lines give the theoretical values according to [KDP80], symbols represent measurement data. The deviations are mostly negative and do not increase with gate voltage, which implies a zero or constant bulk contribution to transport.

the top and bottom surfaces the conducting side surfaces of the 3D TI as well as bulk states might be considered. From Fig. 3.9 the presence of occupied bulk states can not be excluded. What can be excluded is an increasing influence of the additional channel with increasing V_g, because the deviations are stable. Increasing influence though is expected for bulk states if a higher Fermi energy can enhance the occupation of the conduction band. Thus, it is discussed, if the Hall signal can be explained by a current flowing in the side surfaces. Therefore it must be clarified, that the side surfaces can carry enough current.

In order to estimate a lower limit for the resistance of the side surfaces, the lowest accessible resistivity of the system is chosen. It is reasonable to assume, that the HgTe side surfaces exhibit a resistivity lower than the top and bottom layer, because they are exposed to indirect argon bombardment during the fabrication process. It is known, that argon ion milling of $Hg_{0.8}Cd_{0.2}Te$ dopes the sample n-type (see for example Ref. [BF89] or Ref. [BHG+94]). This means, that one should as well consider a possible doping effect by ion milling of pure HgTe. Therefore

the four-terminal resistivity at $V_\mathrm{g} = 5\,\mathrm{V}$ of the complete system is determined from Fig. 3.3 and taken as the lowest estimate of the side surface resistivity. One finds $\rho(5\,\mathrm{V}) = 147\,\Omega$, leading to a resistance $R_\mathrm{side} = \rho \cdot L/W = 1.26\,\mathrm{M}\Omega$, where $L = 600\,\mu\mathrm{m}$ and $W = 70\,\mathrm{nm}$ are used. If now the two-terminal sample resistance at non-zero magnetic field is approximated by the resistance of a 2DEG in the quantum Hall regime with a single conducting channel, one finds $R_\mathrm{2DEG} = R_\mathrm{K}$ (see Ref. [FS83]). R_K is thus a good estimate for the case of few edge channels. The current flowing in a single side surface is now related to the current in one surface 2DEG by the simple equation

$$\frac{I_\mathrm{side}}{I_\mathrm{2DEG}} = \frac{R_\mathrm{2DEG}}{R_\mathrm{side}} = 2.0\%. \tag{3.9}$$

This value represents the upper limit of current flowing in the side surfaces and indeed is comparable with the observed deviations. One could argue now, that the resistance R_2DEG will drop, if the number of edge channels is increased by a change of gate voltage or magnetic field. Thus, the fraction of current in the side surface would decrease for growing i. However, also the side surfaces are affected by the gate and in a parallel magnetic field (as applied in this work) they should exhibit a quadratic magneto-resistance. Therefore the conducting side surfaces are the reason for the deviations more likely than bulk states.

Another evidence for this is the observation, that even for high gate voltages the Hall plateaus are still well quantized. To emphasise this, in Fig. 3.10 the magneto-resistance data for $V_\mathrm{g} = 5\,\mathrm{V}$ is presented. From an additional Hall contribution stemming from bulk carriers with similar mobility one would expect a significant slope on the Hall plateaus. Such a tilt of the plateaus in addition to a deviation of the theoretical value is not observed. In contrast to bulk states the side surfaces should not tilt, but only lower the Hall plateaus and therefore are the more appropriate candidate for the additional channel. The longitudinal resistance for the observed SdH-minima in Figs. 3.4, 3.6 and 3.10 does not vanish completely. This as well might indicate a parallel conducting channel, although a non-zero minimum resistance can also result from strong broadening of the maxima.

Surprisingly, to the question when bulk conduction would become important in the sample, the above arguments and analysis of the data lead to the answer, that there is no clear evidence for bulk conduction. One possible conclusion is that

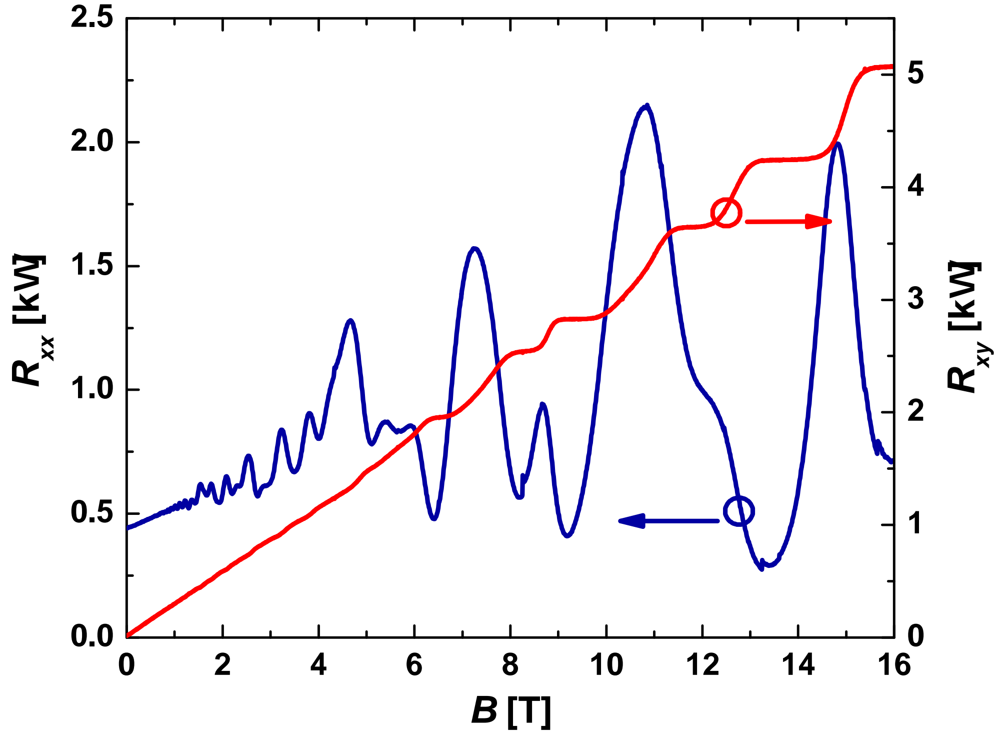

Fig. 3.10.: Hall (red) and longitudinal (blue) resistance of Q2424 for the gate voltage $V_g = 5\,V$. The Hall plateaus exhibit no slope as expected for an additional Hall contribution from bulk conduction.

bulk and surface states are strongly decoupled. If bulk states are occupied, they do not significantly contribute to transport and do not influence the character of the surface states. Following this hypothesis the bulk occupation is allowed to be changed by means of gate voltage, but one can not observe it.

Another way of explaining the measurements is that the Fermi level in the bulk can barely be changed. Possible mechanisms are screening of the bulk by the metallic surfaces around or a pinning of the Fermi energy due to preferential filling of surface states. If the Fermi energy is located in the bulk band gap for $V_g = 0\,V$, it remains there for all applied voltages according to this scenario.

A complete understanding consistent with theoretical models can not be presented yet and is a task for future research.

3.4. Berry phase

The aim of this section is to analyse the absolute position of the extrema in R_{xx} shown in Fig. 3.3 b) and to deduce the phase of the SdH-oscillations. This phase can be related to the Berry phase which is different for normal and Dirac-like charge carriers. A Berry phase of 1/2, that most prominently was shown in graphene [NGM+05], is also expected for surface states of three-dimensional TIs [FKM07] and is in agreement with the shift of the Landau levels as described by Eq. 3.1. If one is interested in the phase only, one can describe the oscillatory behaviour of the longitudinal resistance by

$$\Delta\rho_{xx} \propto \cos\left(2\pi\left[\frac{F}{B} + \frac{1}{2} - \gamma\right]\right) , \tag{3.10}$$

as shown in [TA11]. Here F is the frequency of the oscillating sequence in $1/B$ and γ is the Berry phase. It was shown above (see Fig. 3.7), that both Landau level sequences are influenced by the gate voltage and the distance between adjacent levels and thereby the period $\Delta\left(\frac{1}{B}\right)$ is changed by means of gate voltage. Using Eq. 3.6 one can calculate the frequency F for any pair of neighbouring minima in a single SdH sequence from

$$\Delta\nu = 1 = \frac{nh}{e}\Delta\left(\frac{1}{B}\right) , \tag{3.11}$$

which leads to

$$F = \frac{1}{\Delta\left(\frac{1}{B}\right)} = \frac{nh}{e} . \tag{3.12}$$

Thus, this equation allows for a determination of the carrier density, that corresponds to the oscillations. To obtain a more accurate value, one should plot ν vs $1/B$ and extract n from the slope $\Delta\nu/\Delta\left(\frac{1}{B}\right)$, as evident from Eq. 3.11. However, the filling factor ν, defined as a continuous quantity, can only be determined for certain values of the magnetic field, i.e. for minima ($\nu = 0.5, 1.5, 2.5...$ for n-type Dirac systems) or maxima ($\nu = 1, 2, 3...$ respectively) of an SdH sequence. If therefore integer numbers with arbitrary starting point are plotted against $1/B$ values

belonging to minima positions, the slope of a linear fit according to Eq. 3.11 yields nh/e and n can be extracted. It should be emphasised, that the described method can be applied to a single series of oscillations only. If, like in the case discussed above, two subsets of oscillations exist, one can still use Eq. 3.12 if $n^{\mathrm{t}} = n^{\mathrm{b}}$, because the extrema of both sequences lie on top of each other. From the QHE data one finds this case close to $V_{\mathrm{g}} = -1\,\mathrm{V}$. Furthermore, the two densities are treated to be equal for low magnetic fields, where steps of 2 in the plateau index i (odd sequence) can be observed.

To obtain the phase γ from Eq. 3.10, one has to work out the condition for minima:

$$\cos\left(2\pi\left[\frac{F}{B_{\mathrm{min}}} + \frac{1}{2} - \gamma\right]\right) \overset{!}{=} -1 \tag{3.13}$$

$$\Leftrightarrow\ 2\pi\left[\frac{F}{B^{j}_{\mathrm{min}}} + \frac{1}{2} - \gamma\right] = \pi(2j+1)\,, \tag{3.14}$$

with integers $j = 0, 1, 2...$. This can be reduced to the form

$$j = \frac{F}{B^{j}_{\mathrm{min}}} - \gamma\,. \tag{3.15}$$

For a Dirac system the term $F/B_{\mathrm{min}} = nh/(eB_{\mathrm{min}})$ at the minima positions yields half integers, because the zero level has only half the number of states available. One directly finds, that γ also has to be half integer, meaning $\gamma = 1/2$, to obtain an integer j. However, if the phase γ of an observed oscillation is unknown and shall be taken as an indicator of a Dirac-like sequence, it is possible to plot the integers j, which number the minima, against $1/B^{j}_{\mathrm{min}}$ and to extract the phase from the y-intercept [TA11] as seen from Eq. 3.15.

In Fig. 3.11 a plot of the integers j vs. $1/B^{j}_{\mathrm{min}}$ is depicted for several gate voltages. This is done only for the region of the magnetic field, where an odd integer quantized Hall resistance is observed, which predominantly is the region of small magnetic fields. The j-value has been found assuming that the jth minimum in this field region belongs to a quantum Hall plateau of resistance $R_{xy} = h/\left[e^2(2j+1)\right]$ for a degeneracy of $m = 2$ (c.f. Eq. 3.1). For $V_{\mathrm{g}} = -1\,\mathrm{V}$ the position $1/B^{j=0}_{\mathrm{min}}$ associated with a Hall resistance of $R_{xy} = h/e^2$ was taken as the intersect of the

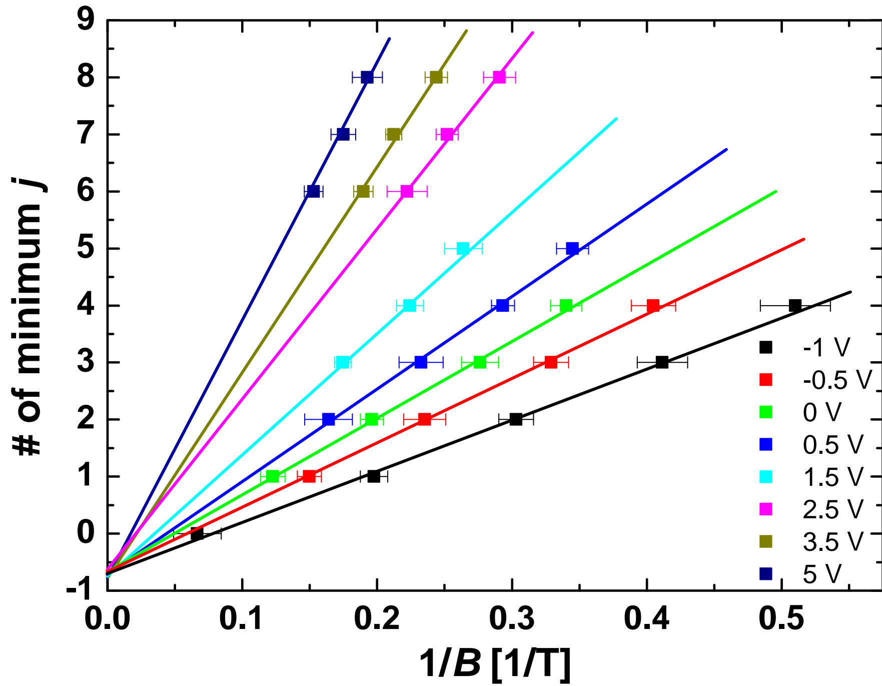

Fig. 3.11.: Plot of integers j numbering the minima of R_{xx} vs. the $1/B$ positions of the corresponding minima. For each gate voltage only the B-region was analysed, in which steps of $\Delta i = 2$ in the Hall plateau sequence (odd integers) can be observed. The negative of the y-intercept equals the Berry phase γ.

Hall plateau with a straight line corresponding to the slope of the low field Hall trace, that hits the middles of visible plateaus of lower index i. This is necessary, because the plateau is expected to be widely prolonged in B and therefore the center position of the plateau and the minimum in R_{xx}, respectively, can not be extracted. The Berry phase γ in Fig. 3.11 is clearly non-zero for all gate voltages within the indicated errors. However, $\gamma = 1/2$ is a possible result with the given uncertainty. This strengthens the interpretation given above, that the observed QHE originates from two Dirac-like surface states.

3.5. Modelling the DOS of a two Dirac cone system

A simple model to fit experimental data can be obtained from a computation of the DOS, that can be compared to the SdH sequence. Both traces will exhibit extrema at the same positions in magnetic field. If the interactions between Landau levels

of the separated surfaces are neglected and a constant charge carrier density n^{t} (and n^{b} respectively) is assigned to a surface, it is possible to calculate the DOS separately and to identify maxima and minima of each sequence. Therefore the Fermi energy E_{F} depending on B is computed from the charge carrier density n^{t} exemplarily. Assuming n-type transport in a single Dirac cone, one can use Eq. 2.7 for the positive branch of the energy spectrum as

$$E_{+}^{N} = \sqrt{2e\hbar v_{\mathrm{F}}^{2} B N}\,,\; N = 0, 1, 2\dots . \tag{3.16}$$

For simplicity, the Zeeman contribution was omitted. However, it can be included easily by changing the spectrum according to Eq. 2.9. With the charge per Landau level $n_{\mathrm{LL}} = eB/h$ for $N > 0$ and $n_{\mathrm{LL},N=0} = eB/(2h)$ one finds the charge located on one surface to be depending on the Fermi energy as

$$n^{\mathrm{t}}(E_{\mathrm{F}}, B) = -\frac{e\,B}{h}\left(-\frac{1}{2} + \sum_{N=0}^{\infty} f(E_{+}^{N}, E_{\mathrm{F}})\right) \tag{3.17}$$

$$\Leftrightarrow n^{\mathrm{t}}(E_{\mathrm{F}}, B) = -\frac{e\,B}{h}\left(-\frac{1}{2} + \sum_{N=0}^{\infty}\left(1 + \exp\left[\frac{E_{+}^{N} - E_{\mathrm{F}}}{kT}\right]\right)^{-1}\right)\,, \tag{3.18}$$

where the sum counts the occupation of all Landau levels and the extra $-1/2$ compensates for a completely filled zero-level (as treated in the sum). The contribution to the charge carrier density of all Landau levels is weighted by the Fermi function $f(E_{+}^{N}, E_{\mathrm{F}})$. To obtain the Fermi energy, an experimentally determined density $n^{\mathrm{t}}_{\mathrm{exp.}}$ is set equal to $n^{\mathrm{t}}(E_{\mathrm{F}}, B)$ from Eq. 3.18 and the value of $E_{\mathrm{F}}(B)$, which is thereby uniquely defined, is calculated numerically [Nov10] for discrete values of B. The shape of the DOS for high magnetic fields can be modelled by Gaussian peaks (see for instance [Ger76]) at the crossings of $E_{\mathrm{F}}(B)$ with E_{+}^{N}:

$$D(B) = \frac{1}{\pi\, G(B)} \sum_{N=0}^{\infty} \exp\left(-\frac{\left(E_{+}^{N} - E_{\mathrm{F}}(B)\right)^{2}}{G^{2}(B)}\right)\,, \tag{3.19}$$

where $G(B) = G_0 \cdot \sqrt{B}$ is a field dependent broadening parameter. The Mathematica code used for these calculations is given in the Appendix B.1.

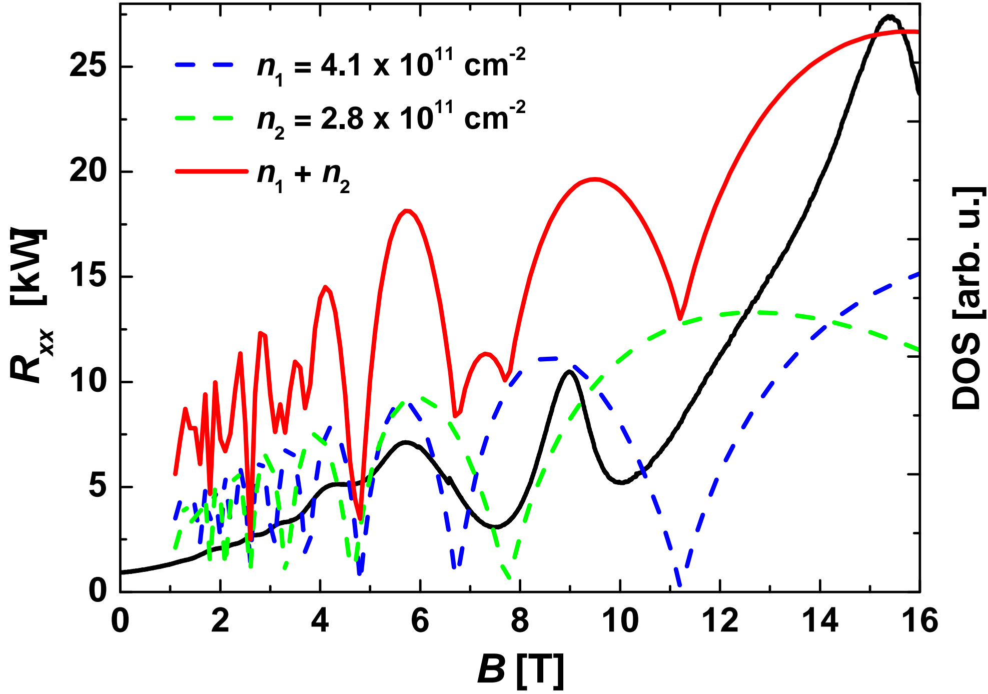

Fig. 3.12.: Longitudinal resistance R_{xx} (black) and calculated DOS for the measurement at $V_\mathrm{g} = 0\,\mathrm{V}$. The green and blue traces show the DOS for single Dirac surfaces at charge carrier densities given by the legend, the red trace is the sum.

In order to verify the method, a gate voltage is chosen for that the two densities are different. Together with the longitudinal resistance (black line) at the gate voltage $V_\mathrm{g} = 0\,\mathrm{V}$ the calculated $D(B)$ is plotted in Fig. 3.12 for the two densities $n_1 = 4.1 \cdot 10^{11}\,\mathrm{cm}^{-2}$ (blue dashed line) and $n_2 = 2.8 \cdot 10^{11}\,\mathrm{cm}^{-2}$ (green dashed line). The red trace is generated by adding up the two independent dashed lines. One notices, that for high magnetic fields $> 4\,\mathrm{T}$ the extrema of the red and black trace roughly coincide, whereas for lower fields a strong damping seems to be present for the experimental data, that is not covered by the Gaussian peak form of the calculated DOS. However, the strong maximum at $B = 5.7\,\mathrm{T}$, that corresponds to a transition from $i = 3$ to $i = 5$ in R_{xy}, is correctly reproduced, as both dashed lines develop a maximum at that magnetic field.

4. p-type transport in 3D HgTe

The focus in this chapter lies on the behaviour of 3D HgTe for negative gate voltages, where the Hall effect exhibits negative sign. By comparing measurements in the conversion region to simple transport equations, a basic understanding of the gated system is achieved. A change is introduced in the layer stack, that improves the surface state quality. As a result it is possible to observe clear pronounced QHE from the surfaces also for the lower half of the Dirac cones. This feature is presented for the first time for a 3D TI. Furthermore the band structure of HgTe with its surface states for devices gated to negative voltages is discussed. The Dirac nature of the p-type carriers is confirmed by an analysis of longitudinal and transverse resistance. A Landau level fan chart, obtained from the derivative of the Hall conductivity with respect to the gate voltage, gives insight to the interplay of the individual surface fillings. In addition, the Hall and longitudinal resistance are investigated in the low magnetic field range, where transport data of high quality samples reveal a rapidly oscillating component, that shows no gate voltage dependence. The measurements are fitted by a model taking into account 3 types of carriers and cosine shaped magneto-oscillations. While this confirms the existence of a third carrier species with high mobility in the system, the explanation of it's origin is not obvious. Different interpretations are applied and evaluated.

4.1. Transiting the CNP

Samples with the so far described layer structure CdTe/HgTe/insulator show for $V_\mathrm{g} = 0\,\mathrm{V}$ total charge carrier densities (obtained from Hall slope at low B) in the range of $3 \cdot 10^{11}\,\mathrm{cm}^{-2}$ to $4 \cdot 10^{12}\,\mathrm{cm}^{-2}$. Therefore, it was not possible for most of them, to deplete this amount of carriers and to achieve p-conductance by a topgate. In this section the reaction to the top gate of two prominent examples

are presented. The sample Q2424 is used as an example for low total carrier density at $V_g = 0\,\mathrm{V}$. For this sample it was possible to change the carrier type by applying a negative gate voltage. In Fig. 4.1 the longitudinal resistance is plotted vs. V_g

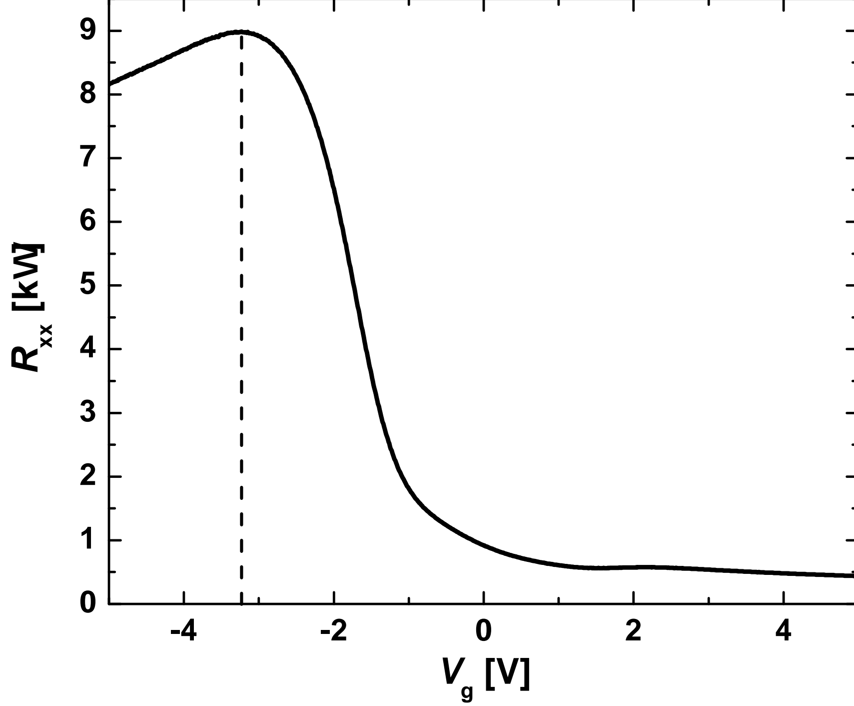

Fig. 4.1.: Zero B-field resistance R_{xx} for the sample Q2424. By means of gate voltage the resistance can be increased to $\approx 9\,\mathrm{k\Omega}$ at $V_g = -3.23\,\mathrm{V}$, marked by the dashed line. For lower voltages the resistance starts to decrease again.

over the entire investigated range. It can be seen, that there is a maximum in the resistance trace at $V_g \approx -3.23\,\mathrm{V}$. Because we assume the two surface dispersions to be shifted against each other in energy, we expect, that a two carrier behaviour will be observed in the gate voltage region of this maximum. Using Eqs. 3.2 and 3.3 we can calculate the longitudinal resistivity $\rho_{xx} = W/L\, R_{xx}$ for such a system,

$$\rho_{xx} = \frac{\mu_1\,|n_1| + \mu_2\,|n_2| + \mu_1\,\mu_2\,(|n_1|\,\mu_2 + |n_2|\,\mu_1)B^2}{e((\mu_1|n_1| + \mu_2|n_2|)^2 + \mu_1^2\,\mu_2^2\,(n_1+n_2)^2B^2)}, \tag{4.1}$$

which for $B = 0$, as given for Fig. 4.1, reduces to

$$\rho_{xx} = \frac{\mu_1\,|n_1| + \mu_2\,|n_2|}{e((\mu_1|n_1| + \mu_2|n_2|)^2)} = \frac{1}{e(\mu_1|n_1| + \mu_2|n_2|)}. \tag{4.2}$$

This result is understandable in a simple parallel conductance picture with the total conductivity $\sigma_{xx} = \sigma_1 + \sigma_2$. If the resistance in Fig. 4.1 follows Eq. 4.2, it is reasonable, that close to the gate voltage, where the top and bottom carriers convert into hole conductance, a maximum in resistance is found due to small values for $|n_1|$ and $|n_2|$ in the denominator. The details of the trace then still are affected by the mobilities μ_1 and μ_2 and their dependence on carrier densities.

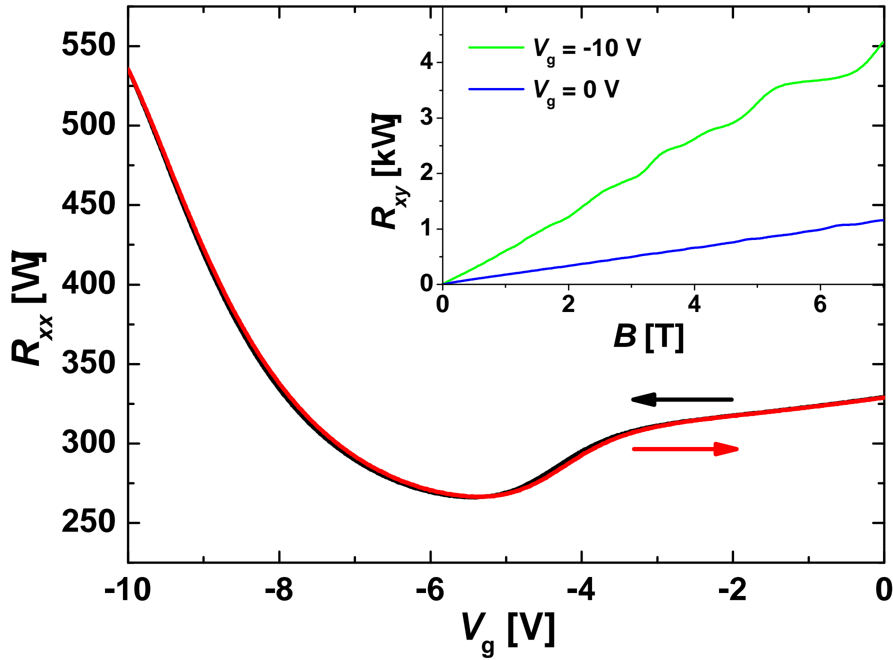

Fig. 4.2.: Zero B-field resistance R_{xx} for the sample Q2451_2 measured back and forth at $T = 1.8\,\mathrm{K}$. In the range of $0\,\mathrm{V} < V_\mathrm{g} < -10\,\mathrm{V}$ the resistance maximum is not reached. Remarkably, no hysteretic effect can be observed in this range. The inset shows the B-field dependence of R_{xy} for the outermost gate voltages of the given range.

Turning now to samples with notably higher charge carrier density, the sample Q2451_2 is considered. In Fig. 4.2 a gate voltage dependent measurement is depicted. The growth characteristics of this sample differ from Q2424 only by the thickness of the HgTe, which is $d_\mathrm{HgTe} = 128\,\mathrm{nm}$. As indicated by the arrows, the sweep direction of the black and red trace are different. From the low field Hall behaviour (the Hall trace is shown in the inset of Fig. 4.2) a total n-type charge carrier density of $3.9 \cdot 10^{12}\,\mathrm{cm}^{-2}$ at $V_\mathrm{g} = 0\,\mathrm{V}$ was determined. The investigation of the conversion of carrier type would thus require significantly lower voltages, than applied in Fig. 4.2, which would imply the risk of a possibly destructive

gate breakthrough. Therefore, the only property of the sample that shall be highlighted here is the non-hysteretic behaviour of the bidirectional measurement. Following Ref. [HBS+06], trap states at the interface of HgCdTe compounds with the SiO_2/Si_3N_4 insulator are expected to screen the gate influence on underlying structures for gate voltages over a certain threshold $|V_g| \gtrsim 2.5\,\mathrm{V}$. Thus, a hysteretic gate action is observed in Ref. [HBS+06], if the threshold voltage is exceeded and instead of the desired manipulation of carrier density, additional trap states are charged. From the starting point at $V_g = 0\,\mathrm{V}$, the charge carrier density can be increased and decreased only by $\Delta n \simeq \pm 6 \cdot 10^{11}\,\mathrm{cm}^{-2}$. This is not the case for the presented sample Q2451_2 and other samples built of CdTe/HgTe/insulator. Only an insulator breakthrough of the gate is limiting the accessible density range for these samples. The total density change of Q2451_2 in the voltage range displayed in Fig. 4.2 with $n(V_g = -10\,\mathrm{V}) = 1.1 \cdot 10^{12}\,\mathrm{cm}^{-2}$ was $|\Delta n| = 2.8 \cdot 10^{12}\,\mathrm{cm}^{-2}$.

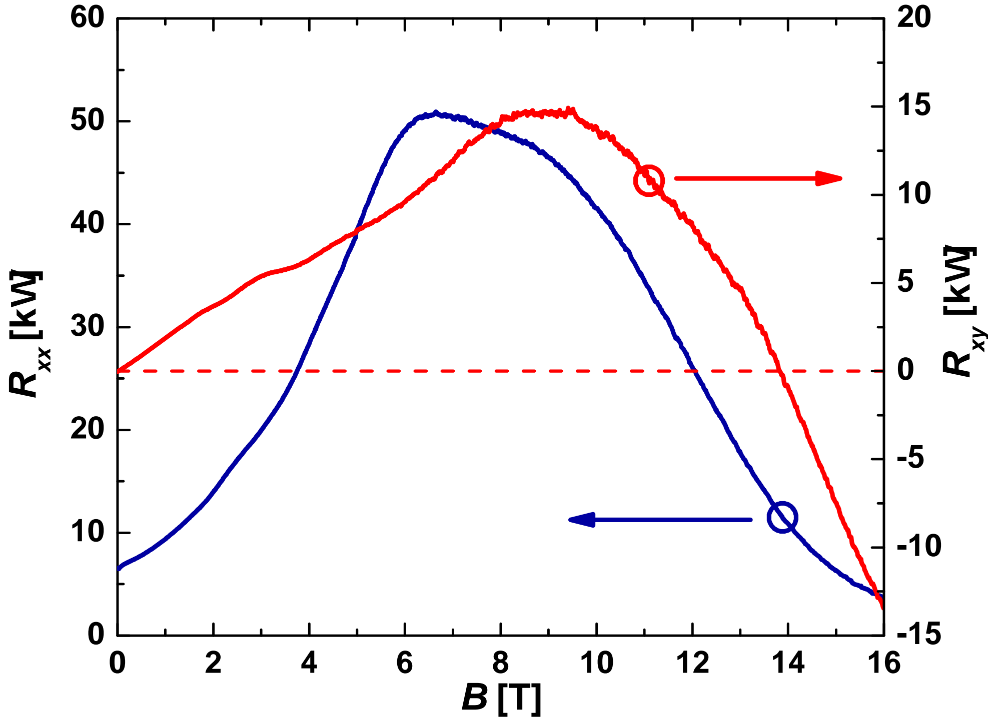

Fig. 4.3.: Longitudinal (blue) and Hall resistance (red) of the sample Q2424 at $V_g = -2\,\mathrm{V}$. After an increase to positive values, a breakdown to lower Hall resistance can be observed. For $B > 13.82\,\mathrm{T}$ the negative Hall resistance indicates a dominating p-type charge carrier density.

For the sample Q2424 an indication of the transition of one type of carriers to p-type can first be observed for $V_g = -2\,\mathrm{V}$ for large magnetic fields ($B > 9\mathrm{T}$), as shown in Fig. 4.3. The Hall signal can not be explained by a gradual decrease

of the current to zero (freeze-out of contacts), because this should push the Hall resistance to infinity. However, here the signal goes to zero and changes sign, while staying finite. With R_{xx} in addition dropping for the regarded B-field region, insulating behaviour can be excluded. The conversion of R_{xy} is therefore attributed to p-type carriers with a considerably smaller mobility, that in the high field limit gain bigger influence onto the combined Hall signal. This can be motivated by the classical description of the two carrier Hall resistance, expressed by Eq. 3.4. It should be mentioned, that this classical equation is basically not valid for high magnetic fields, where the formation of Landau levels defines transport (in Fig. 4.3 we find indications of Hall plateaus for $B = 3\,\mathrm{T}$). The following formulas still help, to qualitatively describe the data. The Hall resistance of a two carrier system in a slightly rewritten form with respect to Eq. 3.4 is given by

$$R_{xy} = \frac{\mu_1^2\, n_1\, B + \mu_2^2\, n_2\, B + \mu_1^2\, \mu_2^2\, (n_1 + n_2) B^3}{e((\mu_1 |n_1| + \mu_2 |n_2|)^2 + \mu_1^2\, \mu_2^2\, (n_1 + n_2)^2 B^2)}, \tag{4.3}$$

which first is approximated for low magnetic fields and $\mu_2 << \mu_1$, where we model carriers of p-type with density $n_2 < 0$ and mobility μ_2. To do so, B^k shall be treated to be 0 for $k > 1$ and terms of order μ_2^2 shall be neglected against μ_1^2. The result is

$$R_{xy} = \frac{\mu_1^2\, n_1\, B}{e(\mu_1 |n_1| + \mu_2 |n_2|)^2} = \frac{n_1\, B}{e(|n_1| + \mu_2/\mu_1 |n_2|)^2} \simeq \frac{B}{e\, n_1}. \tag{4.4}$$

The last equality only holds, if also μ_2/μ_1 is neglected against one. In the end we find, that the Hall behaviour for small magnetic fields can roughly be approximated to go linear with the Hall coefficient of only the charge carrier species with density n_1.

If for high magnetic fields one treats $B^k = 0$ for $k \leq 1$ in Eq. 4.3, one finds, that the Hall resistance

$$R_{xy} = \frac{\mu_1^2\, \mu_2^2\, (n_1 + n_2) B^3}{e\, \mu_1^2\, \mu_2^2\, (n_1 + n_2)^2 B^2} = \frac{B}{e\, (n_1 + n_2)} \tag{4.5}$$

indeed can yield negative numbers irrespective of the mobility ratio μ_2/μ_1, if

for the carrier densities $|n_1| < |n_2|$ is true ($n_2 < 0$). Although the presented approximations are oversimplifications of Eq. 3.4, the Hall resistance in Fig. 4.3 can be understood to result from n-type carriers with density n_1 and high mobility μ_1, that dominate transport for low magnetic fields and p-type carriers, which become significant in the high field limit.

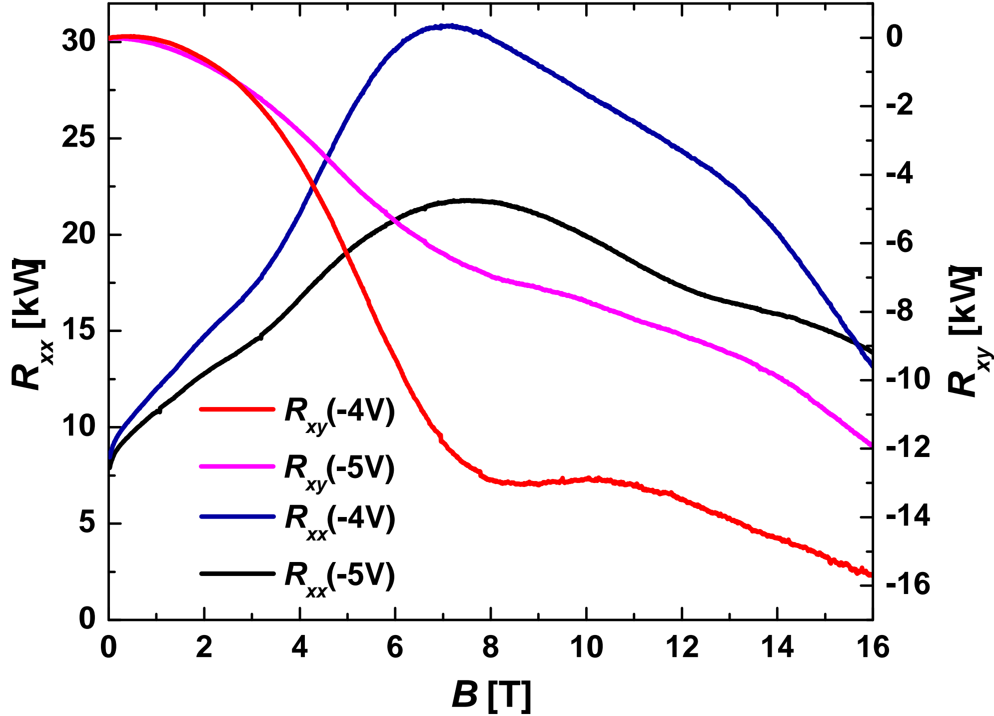

Fig. 4.4.: Hall- and longitudinal resistance of the sample Q2424 for $V_g = -4\,V$ and $V_g = -5\,V$. Indications of Hall plateaus can be seen in the traces.

Fig. 4.4 presents measurements at the even lower gate voltages $V_g = -4\,V$ and $V_g = -5\,V$ of the sample Q2424. In the R_{xy} traces the multi carrier behaviour remains visible and indications of Hall plateaus can be found. One can conclude, that at least one surface state must have been changed to p-type by the gate voltage. This is not self evident, because ARPES investigations on the energetic position of surface bands locate the inversion point of the Dirac cone at or even below the valence band edge [BLN+11b],[COB+13]. Thus it could also be possible, that instead of the conversion of surface carriers one would obtain an increased bulk conductance for negative gate voltages. The negative voltage regime is investigated in more detail in the following sections.

4.2. Improved layer structure: buffer and cap

In Chap. 3 evidence was found from magneto-resistance measurements, that the top surface state exhibits a lower mobility than the bottom one. Naturally, one could ask if a protecting CdTe layer on top of the HgTe enhanced the symmetry of the device. However, from the growth side it is not possible, to achieve a crystalline

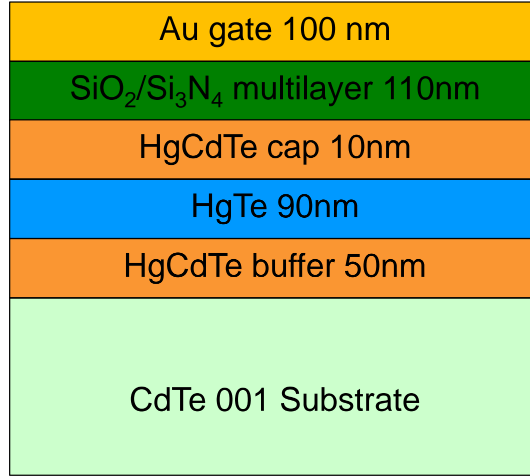

Fig. 4.5.: Layer stack of sample Q2761 as an example for a structure including a $Hg_{1-x}Cd_xTe$ buffer and cap layer, where $x = 0.7$.

CdTe layer with reasonable quality on top of HgTe. Therefore topologically trivial $Hg_{1-x}Cd_xTe$ with $x = 0.7$ can be chosen as a cap material to protect the upper surface. That does not mean, that the idea of symmetrizing the structure has to be dropped, since the $Hg_{1-x}Cd_xTe$ can also be used as a buffer layer underneath the HgTe. For better readability, 'HgCdTe' hereafter will be used as a synonym for $Hg_{1-x}Cd_xTe$ with $x = 0.7$. In Fig. 4.5 an example for the layer structure is including a buffer and a cap. The stacking order belongs to the sample Q2761. While the buffer thickness is only restricted by the onset of relaxation, we find, that the presence of a HgCdTe cap with thickness $d_{\text{cap}} > 10\,\text{nm}$ starts to activate the above mentioned hysteresis effect. This can be seen in Fig. 4.6, where a gate sweep from $V_{\text{g}} = 10\,\text{V}$ to $V_{\text{g}} = -10\,\text{V}$ and vice versa for the HgTe bulk sample Q2763 with a cap of $d_{\text{cap}} = 13\,\text{nm}$ is displayed. A hysteretic shift of $\Delta V = 1.25\,\text{V}$ between the two traces is found. This means a total density difference of $\Delta n \approx 3 \cdot 10^{11}\,\text{cm}^{-2}$ between the two traces with $\delta V_{\text{g}} < 0$ (black) and $\delta V_{\text{g}} > 0$ (red) at a certain gate voltage point. To avoid this hysteresis effect, that leads to non-unique mapping of V_{g} to n, many of the produced structures have a cap of $d_{\text{cap}} = 5 - 10\,\text{nm}$. The

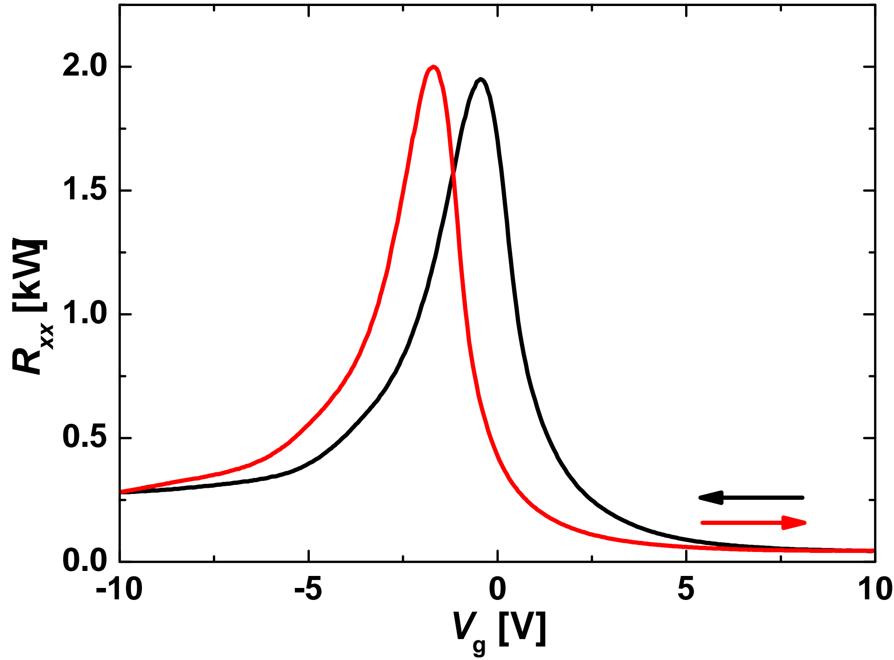

Fig. 4.6.: Longitudinal resistance R_{xx} for a bidirectional gate sweep of the sample Q2763 with $d_{\mathrm{cap}} = 13\,\mathrm{nm}$. A hysteretic shift of the trace is observed due to screening of the gate effect by charged impurities.

conclusion is applicable also for HgTe quantum wells with HgCdTe barriers, if absent hysteresis is more important than a high mobility in the HgTe layer.

In order to demonstrate the consequences of the additional buffer and cap layers (see layer stack in Fig. 4.5), a standard Hall bar of the sample Q2761 for an applied top gate voltage of $V_{\mathrm{g}} = 2\,\mathrm{V}$ is investigated. The results are plotted in Fig. 4.7. A total n-type density of $n = 6.4 \cdot 10^{11}\,\mathrm{cm}^{-2}$ is obtained by fitting the Hall slope for small B-fields, comparable to the value of the above discussed sample Q2424 at 0V. The total sheet resistance $\rho_{\mathrm{Q2761}}(0\,\mathrm{T}, 2\,\mathrm{V}) = 44\,\Omega$ is nearly an order of magnitude smaller than the one of the reference Q2424 without additional HgCdTe layers, that shows $\rho_{\mathrm{Q2424}}(0\,\mathrm{T}, 0\,\mathrm{V}) = 307\,\Omega$. According to Eq. 4.2 this can for equal carrier concentrations only result from a massively increased mobility in at least one of the surface states at the HgTe interfaces. Accordingly, the broadening of the SdH peaks in Fig. 4.7 is much smaller compared to the ones of Q2424 at the same carrier concentration (the trace is shown in Fig. 3.3). The small broadening moreover is similar for all the peaks including neighbouring ones, which indicates, that the mobilities of the two surfaces are close to each other. Thus, the attempt to

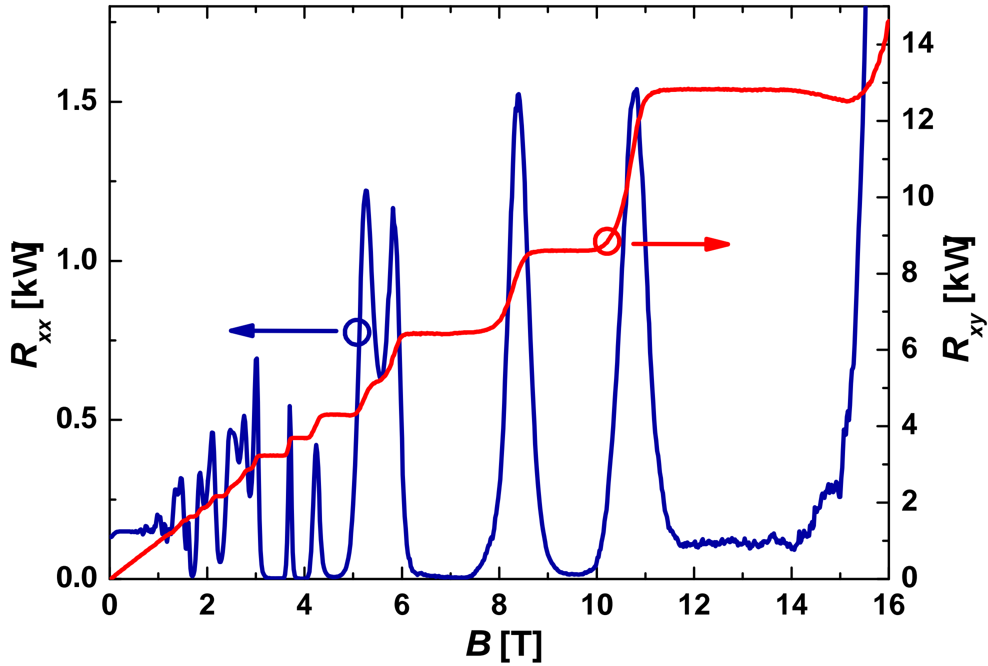

Fig. 4.7.: n-type Hall (red) and longitudinal (blue) resistance of Q2761 with HgCdTe buffer (50 nm) and cap (10 nm) at $V_g = 2\,\mathrm{V}$. The broadening of neighbouring SdH peaks is similar and a low total sheet resistance can be observed.

increase the symmetry regarding the environment of the upper and lower surface state was successful.

What nicely can be seen for the presented SdH sequence are the zero resistance minima, that are present, if the Fermi energy resides in an energy region, where both Landau level sequences are gapped. This confirms the in Chap. 3 given interpretation, that bulk conduction plays a negligible role in the devices.

4.3. Ambipolar QHE

The higher mobilities and lower mean carrier concentrations for samples with the modified layer structure described above enable more detailed investigations of the transport properties of p-type carriers in HgTe 3D TI samples. For this purpose, the sample Q2584$^{\mathrm{Nij}}$ with a layer structure of HgCdTe/HgTe/HgCdTe of thickness 100 nm/60 nm/5 nm from the bottom was measured to high magnetic fields at the HFML in Nijmegen in the Netherlands. All measurements of samples labelled with the addend $^{\mathrm{Nij}}$ were taken at a temperature of $T = 300\,\mathrm{mK}$ in a ^{3}He cryostat. The

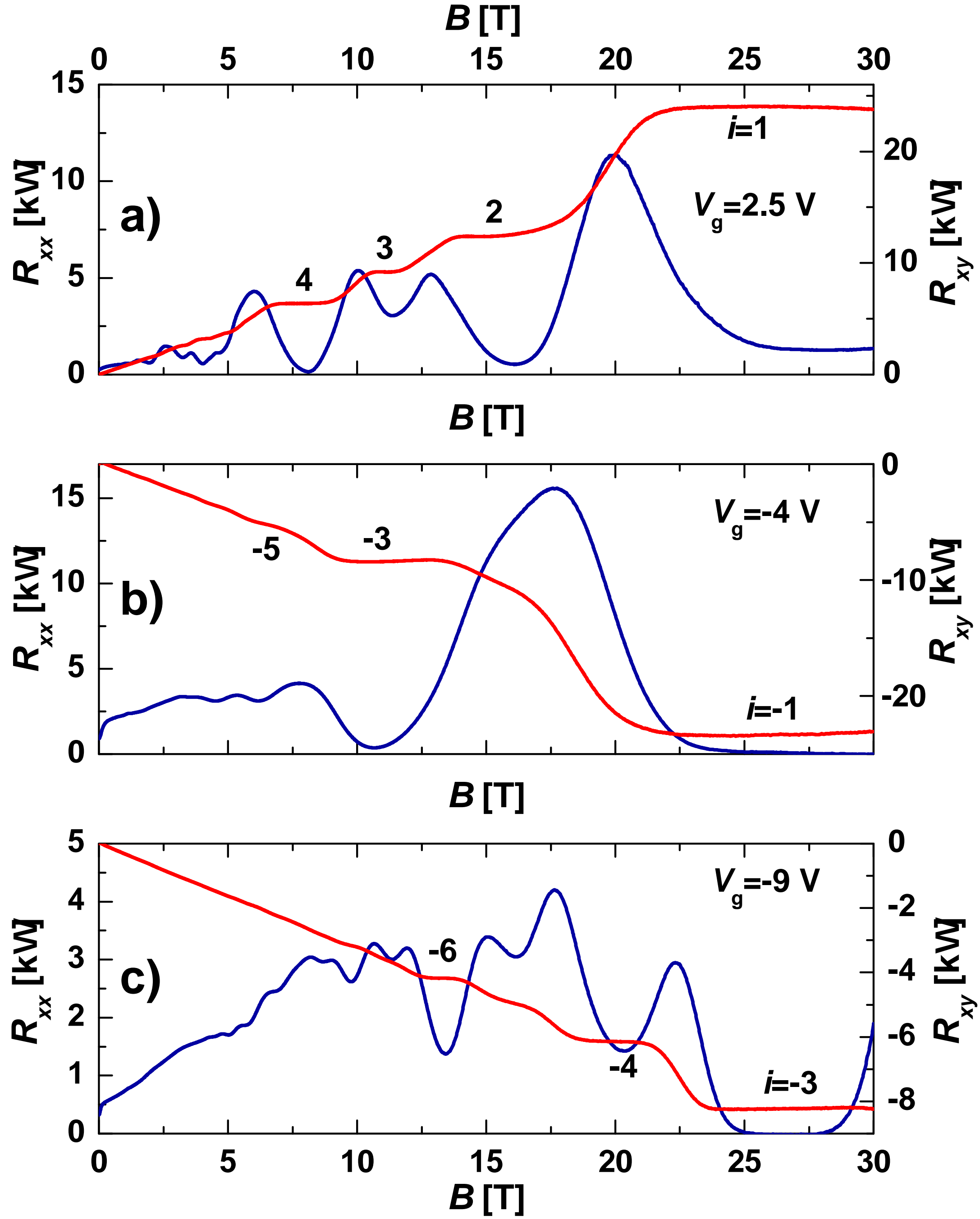

Fig. 4.8.: Hall (red) and longitudinal (blue) resistance for the sample Q2584[Nij] measured at the HFML in Nijmegen. The applied gate voltage is indicated in the figures. By indices i the quantum Hall plateaus for n-type [a)] and p-type [b),c)] transport are labeled.

most striking results are given in Fig. 4.8, where magnetic field dependent measurements of the Hall bar sample for different gate voltages are depicted. While Fig. 4.8 a) shows n-type surface transport with the properties already discussed in Chap. 3, one also finds remarkably well developed quantum Hall plateaus for negative voltages [Fig. 4.8 b) and c)]. The corresponding SdH minima are going to zero for large enough Landau level spacing (see for example $B > 25\,\mathrm{T}$). In Fig. 4.8 b) an odd integer sequence of quantum Hall indices can be observed, indicating, that the gate voltage position V_g^e of equal carrier densities for top and bottom surface for this sample is realized in the p-regime. For other voltages even plateaus are found again. The p-type QHE with zero resistance minima is interesting, because the gate behaviour of the surface states expected from self-consistent band structure considerations does not match the experimental observation. The position of the apex of the Dirac cone (in analogy to graphene here also referred to as CNP) in HgTe is estimated to be close to the valence band edge. Fig. 4.9 shows an ARPES measurement of an undoped, ungated sample including a sketch of the energetic

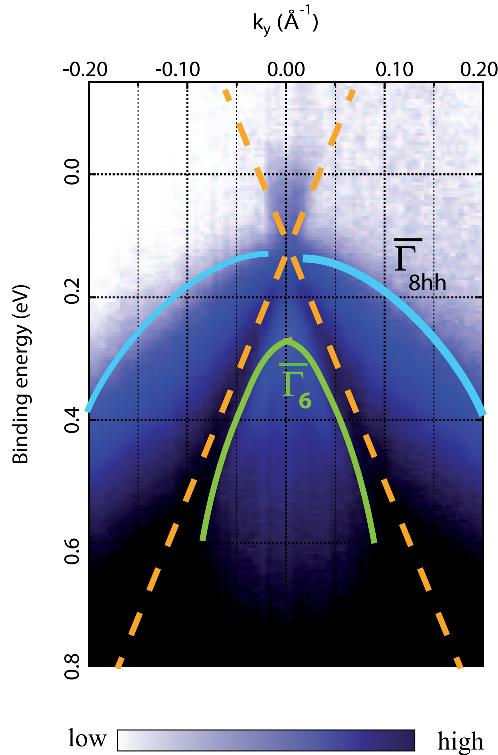

Fig. 4.9.: ARPES measurement of strained HgTe oriented in [001] direction. The surface states are indicated by a dashed line. The blue line highlights the valence band edge. The Fermi energy is located at 0 eV. Picture taken from Ref. [COB+13].

positions of bulk and surface bands, given by the authors of Ref. [COB+13]. The CNP according to the sketched lines lies 100 meV below the Fermi energy (0 meV) and around the valence band edge (blue line). However, the position has an uncertainty of at least 50 meV. This position in relation to the valence band edge can depend on the surface chemistry of the sample. Thus, in theoretical models there is also some freedom of choice for the position of the CNP. In Ref. [COB+13] the experiment is supported by a theoretical calculation of the band structure using an 8 band Kane model. The model yields a CNP slightly below the valence band

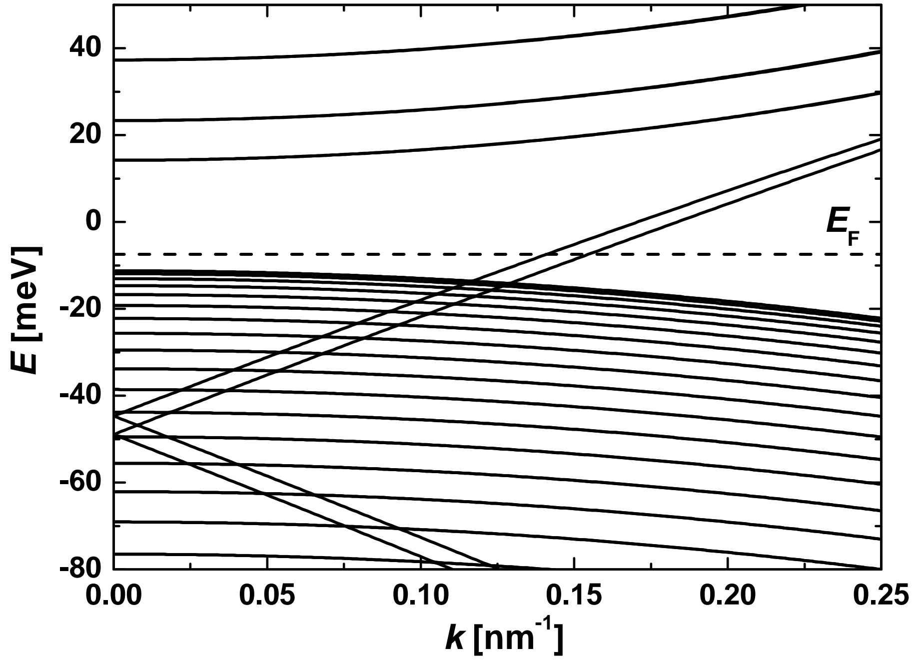

Fig. 4.10.: Band structure obtained by an 8 band $k \cdot p$ calculation with hybridisation terms between Γ_8 heavy holes and surface states set to zero. The linear dispersing surface states are populated by nearly equal numbers of n-type carriers.

edge, and can be considered consistent with the CNP position of Fig. 4.9. Also this model basically agrees with other models regarding the energetic position of the CNP, described in Refs. [DHQ+08],[BLN+11b] and [CSLS11]. For the valence band structure all the self-consistent calculations utilizing the Kane model yield closely spaced bulk sub bands, that should pin the Fermi energy before p-type surface transport would be achieved. In this picture, a high p-type carrier density on the surface and thus a low Fermi energy is accompanied by a significant bulk state occupation.

However, if the p-type QHE stems from the surface states, strongly populated

bulk states are not consistent with the observation of nicely flat quantum Hall plateaus and zero R_{xx} for $V_\mathrm{g} = -9\,\mathrm{V}$ ($n = -1.8 \cdot 10^{12}\,\mathrm{cm}^{-2}$) in Fig. 4.8. An interesting feature of Fig. 4.9, emphasised in Ref. [COB+13], is the weak hybridisation between surface states and Γ_8 bands, evident from the impressively large range of linear dispersion of the Dirac state. This could be a key observation to explain, why p-type transport is measurable at all. If the surface states do not couple to the nearby Γ_8 bands different mobilities would be expected for the bulk and the surface states. As a result, conduction through the surface states is possible without strong bulk contributions. To test this hypothesis with a toy model, in the $k \cdot p$ Hamiltonian the coupling terms between surface state and heavy hole Γ_8 band can be artificially suppressed.
An example for the band structure resulting from a calculation as described is given in Fig. 4.10. Here the surface states are dispersing perfectly linear, as there is no interaction with the bulk valence band levels. The gate range of pure surface occupation is bigger in this model, however, for large positive or negative gate voltages also bulk states would be occupied. It should be emphasised that the switch-off of hybridisation terms cannot be motivated by a physical understanding and the result may suggest that the self-consistent 8 band Kane model is not an appropriate model to describe the combined system of coexisting surface states and bulk bands.

A more physical approach to explain the surprisingly robust QHE is to incorporate the screening of bulk states by the surfaces. For positive gate voltages one can show that a gate induced potential, strongly confined to the surface of the HgTe, changes the position of the Dirac cone relative to the Fermi energy, but does not affect the bulk properties. An example for such a potential is given in Fig. 4.11 a) where we assumed symmetrically charged surfaces for $V_\mathrm{g} = -1\,\mathrm{V}$. When a $k \cdot p$ calculation is run with this (non-self-consistent) potential, one obtains indeed states which are well confined to the surface. The probability density is shown in Fig. 4.11 b) where the red traces describe the bottom surface, and the top surface is represented in blue. Most importantly, the band structure result of the calculation yields a Fermi level that is located in the bulk band gap for a large range of gate voltages. This can be seen in Fig. 4.12 b) for a reasonably large voltage $V_\mathrm{g} = 5\,\mathrm{V}$. The case of degenerate surfaces is depicted in Fig. 4.12 a), respectively. We want to note, that the presented model does not give an explanation, why the potential is confined so distinctly to the HgTe surfaces. To explain the shape of the potential a first

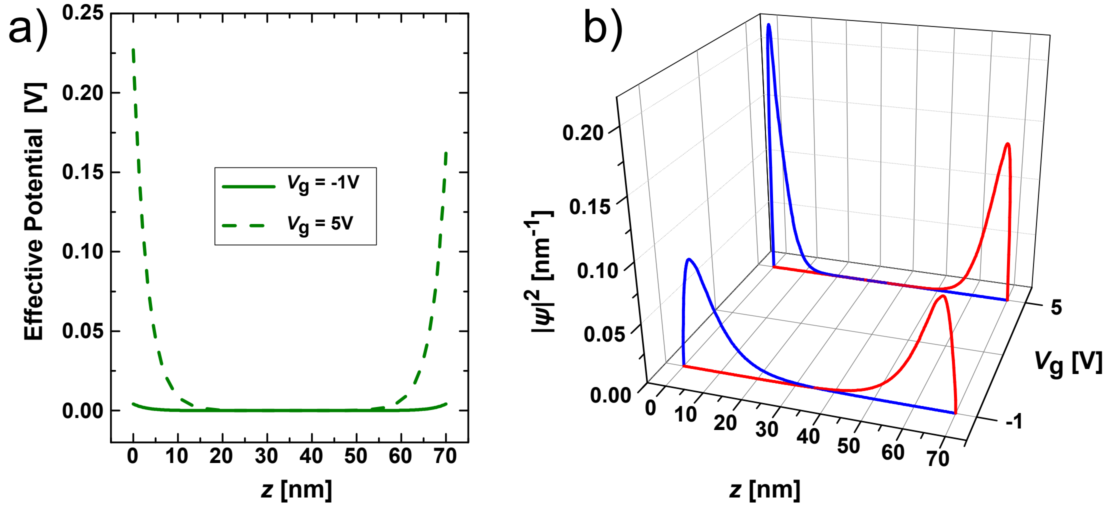

Fig. 4.11.: a) gives the effective potential constructed to populate the surfaces of the device only. For $V_g = -1\,\mathrm{V}$ the bands are flat with a nearly vanishing potential. An increased gate voltage ($V_g = 5\,\mathrm{V}$) is modelled by a steep potential at the surface. In b) the corresponding evolution of the probability density of the top (blue) and the bottom (red) surface state at the Fermi level E_F is shown.

approach could be a study of the dielectric properties of bulk and topological surfaces in the material. A difference in the dielectric constant ϵ for bulk and surface would directly influence the interplay of the potential Φ and the charge density ρ via the Poisson equation of the electric field (see e.g. Ref. [Jac75]):

$$\triangle\,\Phi = -\frac{\rho}{\epsilon}\,. \tag{4.6}$$

There is no obvious reason why the presented model utilizing a steep potential at the surfaces should not be applicable also for negative voltages. Thus, the stability of the p-type QHE could be motivated in the same framework of screening of the bulk by the topological surface states. This would imply, that the relative position of the Dirac cone can be freely adjusted by the gate voltage, while the bulk occupation stays zero or constant.

To unambiguously proof the observed QHE features to originate from the TI surface states, the Hall conductivity for Q2584$^{\mathrm{Nij}}$ at different gate voltages is presented. It can be calculated in the following way:

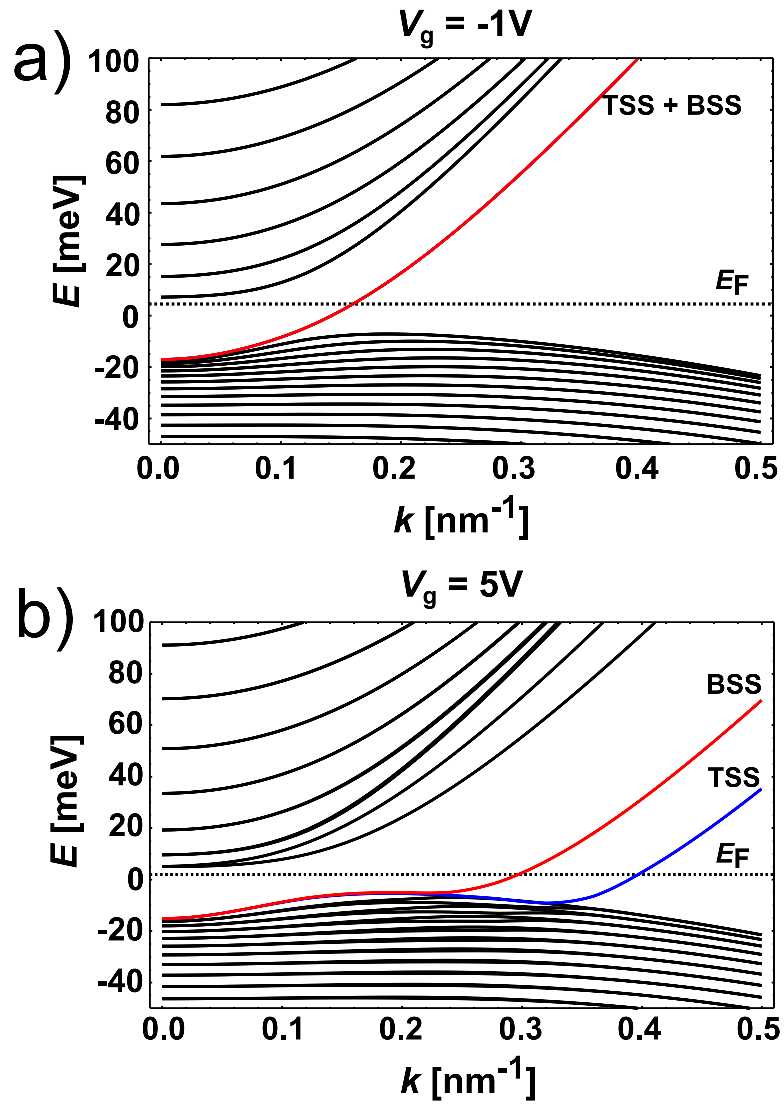

Fig. 4.12.: a) Band structure for the potential shown in Fig. 4.11 at $V_g = -1\,\mathrm{V}$ (a) and $V_g = 5\,\mathrm{V}$ (b). The top (TSS) and bottom (BSS) surface state are coloured in blue and red, respectively. Black lines represent bulk states.

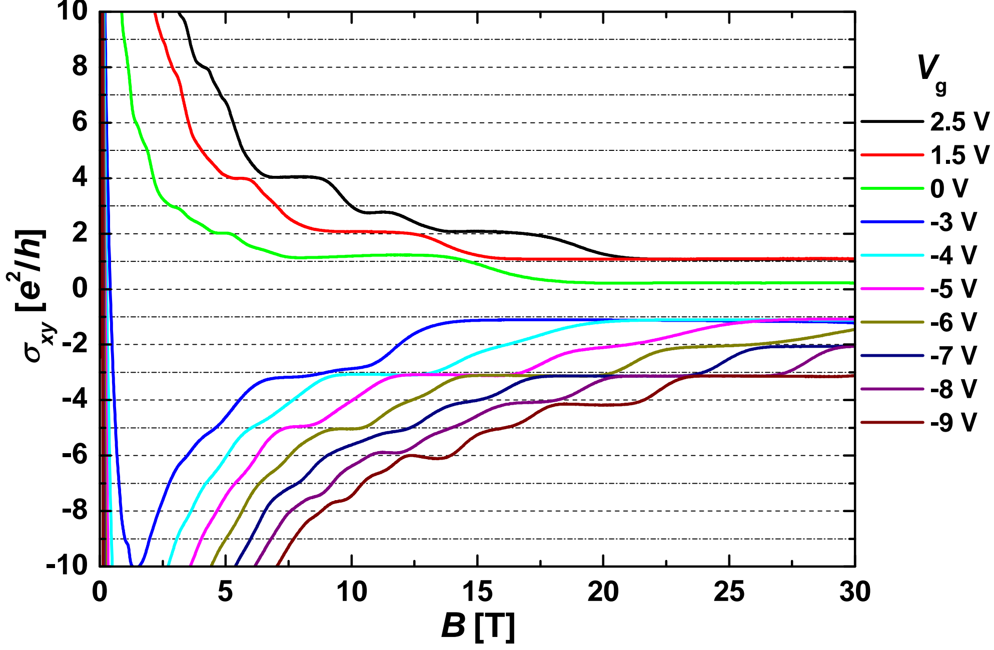

Fig. 4.13.: Hall conductivity σ_{xy} for a wide gate voltage range for the sample Q2584$^{\mathrm{Nij}}$. The n-type and p-type traces show decent quantization in values of e^2/h.

$$\sigma_{xy} = \frac{R_{xy}}{R_{xy}^2 + \rho_{xx}^2}\,, \tag{4.7}$$

with the longitudinal resistivity $\rho_{xx} = W/L \cdot R_{xx}$ in a 2D system (see for example Ref. [BvH91]). In Fig. 4.13 the Hall conductivity is plotted for the sample Q2584$^{\mathrm{Nij}}$ for the whole investigated gate voltage range. The traces decently quantize to the expected multiples of e^2/h, however, as discussed in Chap. 3, deviations are observable. It should be emphasised, that these deviations do not differ for n-type and p-type transport. Following the lines of constant Hall conductivity at $\sigma_{xy} = -2e^2/h$ and $\sigma_{xy} = -4e^2/h$, one finds plateaus evolving with decreasing gate voltage, meaning, that difference between the top and bottom surface carrier concentration is steadily increased.

For a more accurate study, the carrier densities of top (n^{t}) and bottom surface (n^{b}) are determined from the SdH frequencies of the measurements at different gate voltages using Eq. 3.12. The result is plotted in Fig. 4.14 together with the density n_{Hall} obtained from the low field Hall data. Both surface densities show a linear dependence on the gate voltage and approximately add up to the total density n_{Hall}. One further can analyse the phase of the SdH oscillations for

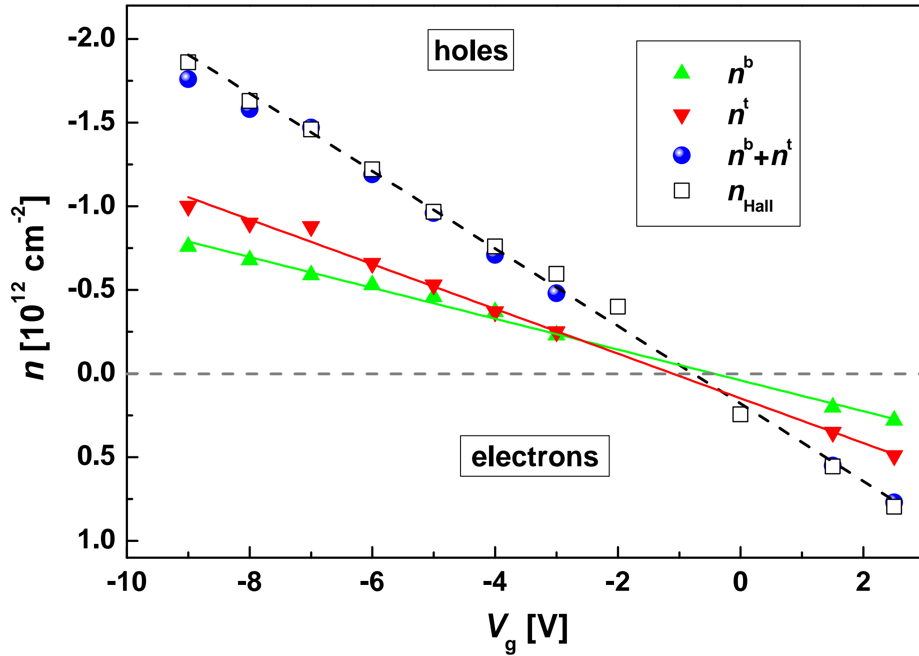

Fig. 4.14.: Gate voltage dependence of different surface densities n^{t} and n^{b} obtained from the analysis of frequencies in the SdH patterns. The sum of the two is matching the total density n_{Hall} in the system, calculated from the Hall slope.

the case of degenerate sets of Landau levels utilizing Eq. 3.15. In Fig. 4.15 the longitudinal resistance for $V_{\mathrm{g}} = -4\,\mathrm{V}$ is plotted vs. $1/B$. The minimum values and the corresponding uncertainty are indicated in the plot. The position of the minimum for $j = 0$ was taken as the intersection of the extrapolated low field Hall trace with the plateau at $i = -1$. All minima are numbered by indices j and in the inset of Fig. 4.15 it is depicted how this minimum index j goes with the $1/B$ coordinate. By a linear fit (dashed blue line) the expected non-zero Berry phase of $\gamma = -0.5$ is sustained. From the analysis above there is plausible experimental evidence that the QHE traces shown in Fig. 4.8 for p-type transport are arising from the Dirac-like dispersing surface states. The linear gate dependence of both states including the conversion to n-conducting behaviour confirms that these states not only dominate the magneto-transport for the whole accessible range of gate voltage, but also are not affected by Fermi level pinning at the edge of the valence band or perturbed significantly by its closely spaced sub bands.

Another method to gain insight to the Landau level structure was already introduced in Chap. 3. A Landau fan diagram can be created from gate and B-field dependent resistance data. For this purpose an additional Hall bar of Q2584 was

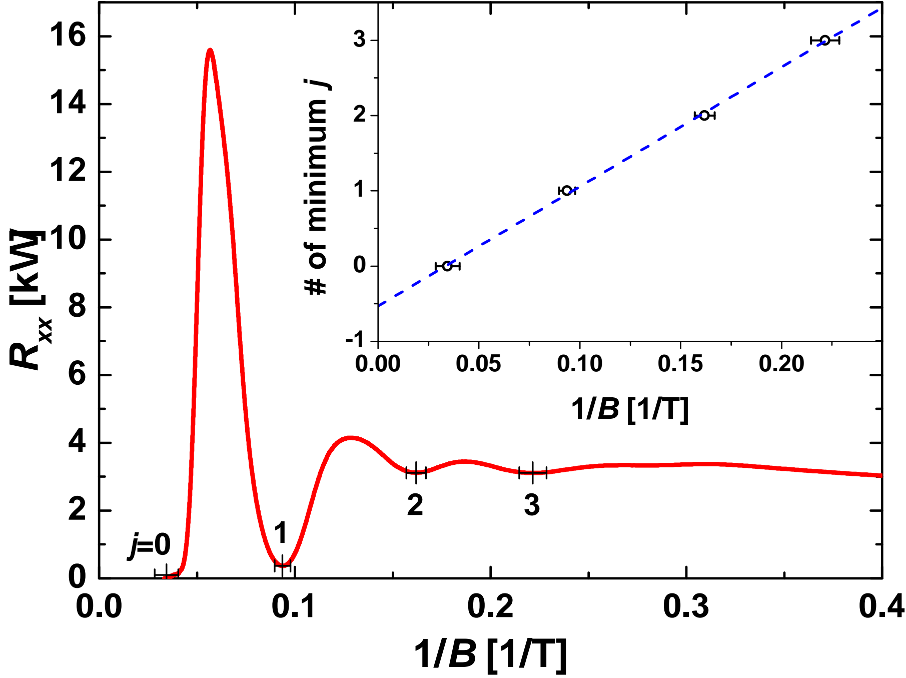

Fig. 4.15.: Longitudinal resistance R_{xx} of Q2584$^{\mathrm{Nij}}$ at $V_{\mathrm{g}} = -4\,\mathrm{V}$ plotted vs. the inverse magnetic field $1/B$. The minima positions and indices j are marked. Inset: index j assigned to minima of the trace are extrapolated to $1/B \rightarrow 0$ (dashed blue line is a linear fit to the data) yielding the non-zero berry phase $\gamma \approx -0.5$.

fabricated with the aim to measure this device in all detail at the base temperature of a dilution refrigerator. For high resolution datasets it is possible to plot the derivative of the Hall conductivity $\partial\sigma_{xy}/\partial V_{\mathrm{g}}$, which exhibits a high value for transitions between plateaus in σ_{xy}, corresponding to Landau level positions, and zero between the levels (corresponding to plateaus in σ_{xy}). Thus, it is possible to visualize Landau level traces. In Fig. 4.16 a) the derivative $\partial\sigma_{xy}/\partial V_{\mathrm{g}}$ is plotted in blue for low values and in red for high values of the derivative, respectively. The numbers denote the quantum Hall index i, which is found from σ_{xy}, and confirm that the observed red areas (high values in $\partial\sigma_{xy}/\partial V_{\mathrm{g}}$) indeed belong to non-degenerate Landau levels resulting in a change of $\Delta\sigma_{xy} = e^2/h$, if crossed by the Fermi energy.

By the white dashed and straight lines the Landau levels for higher indices N of the individual sequences are approximated. These converge to two gate voltage positions for $B = 0$, that can be interpreted as the CNPs of the individual surface states. Analysing the intersections of dashed lines with straight ones, the $i = -4$ -plateau on the p-conducting side is most striking. In Fig. 4.16 b), c) and

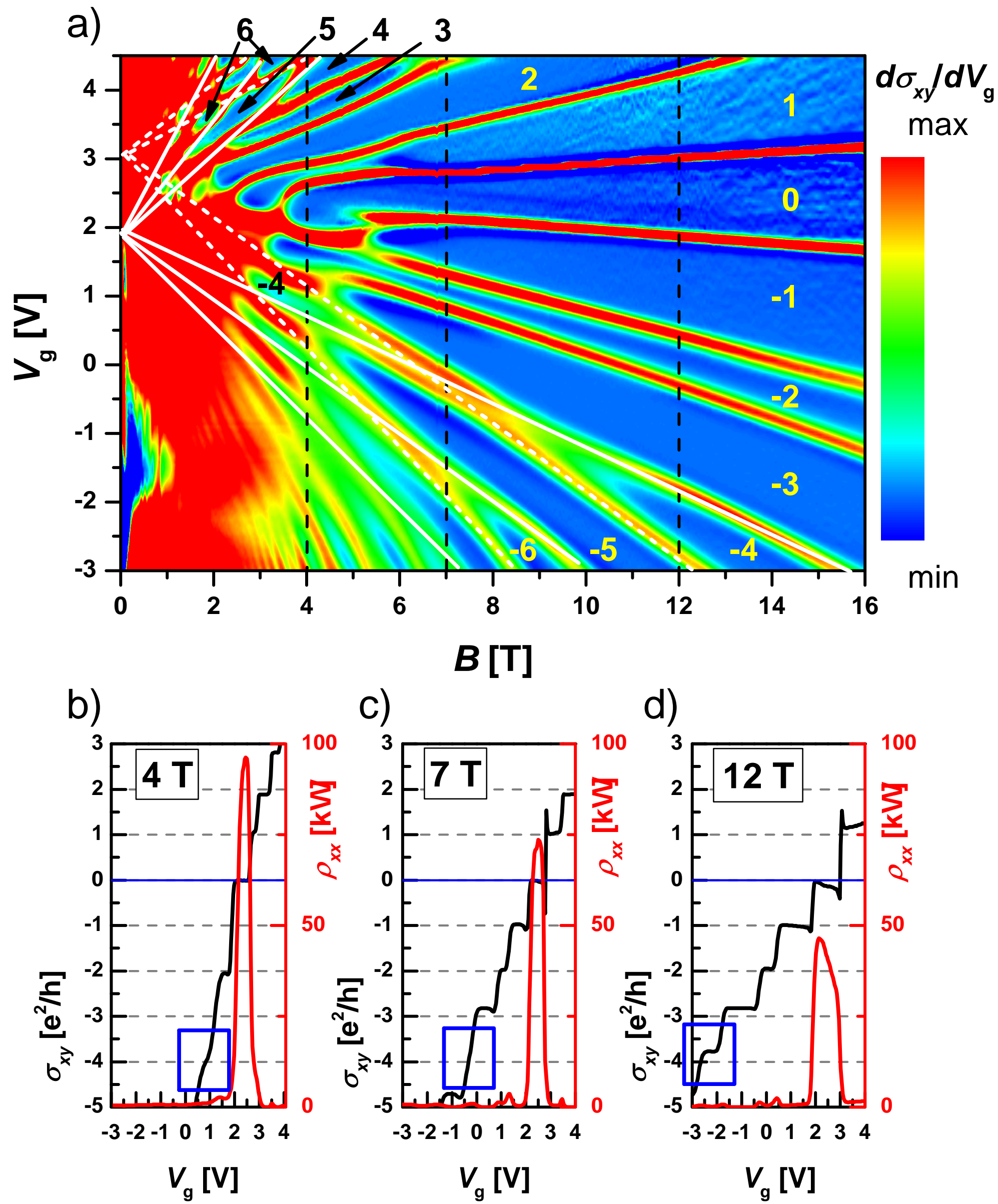

Fig. 4.16.: a) Landau level chart of the sample Q2584: The derivative $\partial\sigma_{xy}/\partial V_\mathrm{g}$ yields high values (red) at the positions of Landau levels in B and V_g. Numbers denote quantum Hall indices i, white lines indicate the two fans originating from two surfaces for higher fillings. b) - d) Line cuts of σ_{xy} (black) and ρ_{xx} (red) at the magnetic fields indicated in a) by dashed black lines. The reappearance of $i = 4$ (emphasised by the blue boxes) is taken as a proof that two independent sequences exist (see main text). By blue lines the zero in Hall conductivity is marked.

d) line cuts of σ_{xy} (black) and ρ_{xx} (red) are shown along the black dashed lines of Fig. 4.16 a) at $B = 4\,\mathrm{T}$, $B = 7\,\mathrm{T}$ and $B = 12\,\mathrm{T}$, respectively. The plateau of $\sigma_{xy} = -4\,e^2/h$ is weakly marked in Fig. 4.16 b) and vanishes completely at $B = 7\,\mathrm{T}$ in Fig. 4.16 c), highlighted by the blue boxes. For a higher magnetic field, the plateau is well-pronounced, even though not perfectly quantized to $-4\,e^2/h$ [see Fig. 4.16 d)]. Thus, it can be concluded that indeed a crossing of Landau levels is observed, as indicated by the white lines in Fig. 4.16 a). On the n-side the same phenomenon is visible e. g. for $i = 6$. Together with the fact that the Landau fans have p-type and n-type Landau levels, the crossings give strong evidence that two independent zero gap systems are probed. Thus, the Landau level behaviour in Fig. 4.16 is another confirmation of the two Dirac cone interpretation given above, that explains the B-field dependence.
However, for lower fillings on the surfaces the levels seem to deviate from the origin of the dashed and straight lines. This might be due to changed screening properties of the topological surfaces if only one or two quantum Hall edge channels are present. Also the voltage V_g^e at that top and bottom carrier density are equal is changed in comparison to Q2584$^\mathrm{Nij}$, as can be concluded from the non-vanishing plateau exhibiting $i = -2$ in Fig. 4.16 a).

In Fig. 4.16 b), c) and d) additionally the longitudinal resistivities ρ_{xx} (red traces) are plotted for the displayed values of the magnetic field. An interesting feature is the presence of a distinct resistivity maximum, generating a region of vanishing Hall conductivity. By a blue line, the zero of Hall conductivity is marked in Fig. 4.16 b), c) and d). The region of quantum Hall index $i = 0$, corresponding to the plateaus at $\sigma_{xy} = 0$, is also labelled in Fig. 4.16 a). The observed index in the gate voltage range $2\,\mathrm{V} < \mathrm{V_g} < 3\,\mathrm{V}$ is interpreted to result from the individual fillings of $\nu^\mathrm{t} = -1/2$ and $\nu^\mathrm{b} = 1/2$, that add up to a total Hall conductivity of $\sigma_{xy} = 0$. However, the red areas limiting the region with $i = 0$ in Fig. 4.16 a) can not be interpreted as direct representation of the zero levels of the two Dirac systems. This can be understood from Fig. 4.16 b)-d) and Eq. 4.7. A high longitudinal resistivity gives rise to a plateau of $\sigma_{xy} = 0$ due to $\sigma_{xy} \propto 1/\rho_{xx}^2$. A low σ_{xy} thus is already observed, before the maximum of the peak and therefore the energetic LL position is reached. In the derivative $\partial\sigma_{xy}/\partial V_\mathrm{g}$, however, the first decrease of σ_{xy} arising from the flank of the peak in ρ_{xx} is highlighted. One can conclude that the zero levels must lie slightly inside the region labelled by $\sigma_{xy} = 0$ in Fig. 4.16 a).
Turning to the resistance peaks in Fig. 4.16 b), c) and d) one notes, that for

$B = 4\,\mathrm{T}$ the resistivity nearly reaches $\rho_{xx} = 100\,\mathrm{k}\Omega$, while it decreases with increasing B, where the plateau of $i = 0$ gets wider in V_g [see Fig. 4.16 a)]. This, however, is an unexpected result. The observation of an increasing plateau with $i = 0$ requires that the zero levels of the two cones move differently in gate voltage and thus in energy. The dispersion $E(B)$ given by Eq. 2.9 is plotted in Fig. 2.4 for two Dirac cones. This plot, however, can not be compared directly to the measured Landau level chart in Fig. 4.16 a), because the y-axis denotes gate voltage for the experimental plot while in the calculation energy is taken as the dependent variable. For the top surface, the applied gate voltage is proportional to the charge carrier density if a simple capacitor model is used. This leads to a linear trace of the Landau levels in gate voltage (proportional to the carrier concentration) and magnetic field because a constant filling factor according to Eq. 3.6 yields $n \propto B$. The linearity is lost if the relation $n(V_\mathrm{g})$ is changed. One might expect this for the lower surface state, where n^b could besides the gate voltage depend on the screening properties of the top surface. At least for high magnetic fields, the dispersion of the Landau levels in Fig. 4.16 a) contradicts this idea, because the linear proportionality of carrier concentration and B-field holds for all levels. Thus, one can expect, that a constant energy distance between the two zero levels is mapped to a constant distance in gate voltage. This means, that the energy dispersion E^0_α of the Landau levels for $N = 0$ observed in Fig. 4.16 is not correctly described by Eq. 2.9.

Further one would expect the maximum resistance $\rho_{xx,\mathrm{max}}$ to increase with the magnetic field if a real energy gap was present and the levels limiting the gap diverged as observed in Fig. 4.16 a). However, due to the Dirac states, there is conceptually no energy gap in the band structure, that completely suppresses transport in a magnetic field. In any energy region between Landau levels there should be quantum Hall edge states present on both topological surfaces. This in principle should also be the case between the two zero levels of the top and bottom surface i.e. for $V_\mathrm{g} \approx 2.5\,\mathrm{V}$ in Fig. 4.16 b)-d). If though the zero levels lie close to each other, the region of low resistivity in between might not be visible. An indication on this is the decrease of maximum resistance for growing magnetic field, when the peak in ρ_{xx} gets broader. The peak is interpreted as the sum of two maxima producing a high value of ρ_{xx} when close to each other and a lower but broader peak for bigger separation of the maxima. For even higher magnetic field and thus energy distance between the zero levels a double peak structure is expected to form. Furthermore, the peak height should saturate as soon as the zero levels are well separated. To check if this is the case the resistivity at $B = 16\mathrm{T}$ in

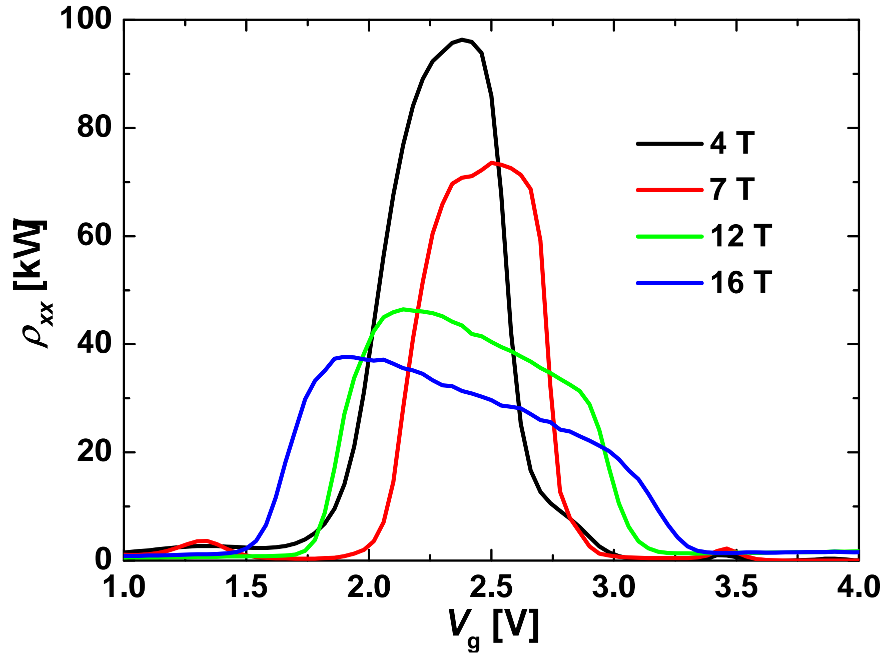

Fig. 4.17.: Longitudinal resistivity ρ_{xx} of sample Q2584 for different constant magnetic fields.

Fig. 4.17 is compared to the ρ_{xx} traces already given in Fig. 4.16 b)-d). The trend of a reduced peak height and increased broadening is continued up to $B = 16\,\mathrm{T}$. A double peak, however, can not be observed. What can be found is an asymmetry of the peak that could originate from different mobilities in top and bottom surface state yielding unequally broadened zero Landau levels. Nevertheless, the fact that the resistivity does exhibit high values between the zero levels shall be discussed.

A high sample resistivity can occur in quantum Hall systems, if edge channels are allowed to backscatter. This is the case on the individual surfaces, if the Fermi energy hits a Landau level. Further one can imagine backscattering due to the existence of states on the second surface. In this context, a possible understanding of the large longitudinal resistivity between the zero levels observable in Fig. 4.17 is presented: In the discussed energy region there are n- and p-type edge channels coexisting in the device [see Fig. 4.18 a)]. The red (electron) and blue (hole) channel have different chirality, however, electrons in both surfaces flow in the same direction. Therefore it is not obvious, how a possible coupling between upper and lower surface could lead to backscattering of carriers. A mechanism that can be considered to hinder transport is the recombination of electrons and holes from the two surfaces. It is plausible, that the conducting side surfaces enable the car-

riers to change between the TI surfaces. In the single channel QHE regime, the n-

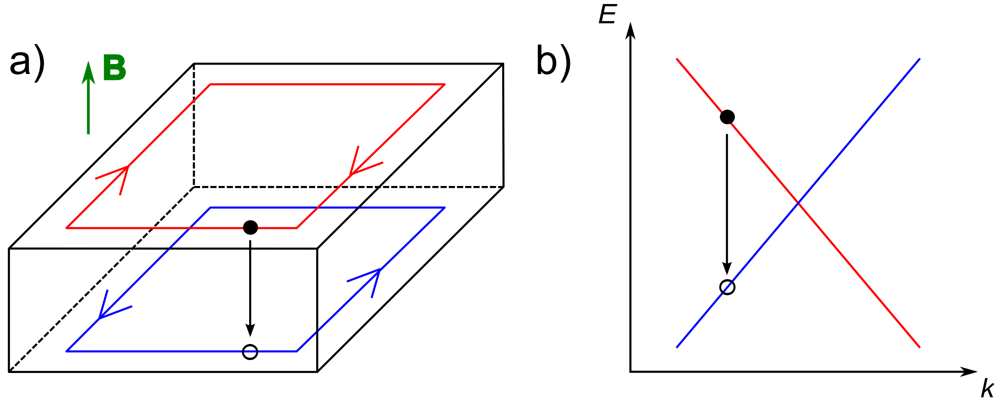

Fig. 4.18.: a) Sketch of the edge channels on the surfaces of a 3DTI, if both surfaces are in the single channel quantum Hall regime with different carrier type. The red line stands for left-moving electrons on one surface of the TI, while the blue one describes right-moving holes hosted by the other surface. At the position of the indicated recombination process, b) gives the dispersion in the quantum Hall edge channels. If carrier exchange between the surfaces is allowed, a recombination of electrons and holes is possible due to matched momentum and spin conditions.

and p-type carriers in the top and bottom surface have energies of $E_{\pm} \approx \pm\hbar\omega/2$. A left-moving electron (red branch) has the same k-value as a right-moving hole (blue branch) in a 1D quantum Hall channel, sketched in Fig. 4.18 b) by the filled and open circle. The dispersion of the 1D quantum Hall edge channels is drawn in analogy to the depiction given in Ref. [QZ11]. In this picture the electrons can lower their energy by $\Delta E \approx \hbar\omega$, if they recombine with a hole. Effectively, the mechanism hinders transport in the device, because it tends to change the system from one n- and one p-type surface to two charge-neutral ones. The resistivity between the zero levels according to this idea depends on the recombination rate in the edge channel system. One can imagine, that it decreases with the thickness of the HgTe layer. A reduction of the recombination rate could also be reached when the Hall bar dimensions are scaled down, because thereby one reduces the total overlap area of opposite edge channels. Finally, one expects a decreasing edge channel width with the magnetic field as derived in Ref. [LG94]. This could lead to a change in resistivity between the zero levels with the magnetic field. These parameters can be varied as a check of the recombination idea. In Fig. 4.17 the overall peak height decreases in magnetic field, however, one can not clearly distinguish between the resistivity on and between the zero levels.
It was shown in this section, that the behaviour of strained bulk HgTe can be ex-

plained by a model, that uses two Dirac cones. The transition to p-type QHE by applying an external gate voltage was demonstrated. There were two possible explanations presented for the observation of clean surface transport from the lower branch of the Dirac cone. Some of the observations still need further investigation, however, a basic understanding of the system could be achieved. Now the focus is set on lower magnetic fields $B < 2\,\mathrm{T}$, where additional features can be found.

4.4. Three carrier behaviour

The interplay of n- and p-type carriers in the energy region between the two neutrality points of the Dirac cones has been investigated above. For lower gate voltages one would expect that the p-type QHE of two independent surfaces with the CNP above the Fermi energy yields a total Hall trace with negative slope only. This situation should for example be found for $V_\mathrm{g} = 1\,\mathrm{V}$ in Fig. 4.16 a), where the two surface states can be identified to have p-type character from the high field behaviour. As evident from the discussion of Eq. 4.3 the Hall trace depends on the ratio of the two surface mobilities. The sign of its slope, however, is only influenced by the charge type of the carriers. In Fig. 4.19 a measurement of Q2584 at $V_\mathrm{g} = 1\,\mathrm{V}$ up to $B = 14\,\mathrm{T}$ is plotted. For low magnetic field a deviation from a perfectly linear Hall behaviour is found. Emphasised by the black circle, a small kink to positive Hall resistance can be observed, while the rest of the trace is in agreement with the two Dirac cone interpretation. It can therefore be supposed, that in addition to the p-conducting surface states, a third component of n-type carriers is active in transport. To further investigate this feature, measurements with higher resolution have to be analysed. A close up in the range of $-0.25\,\mathrm{T} < B < 0.45\,\mathrm{T}$ is plotted in Fig. 4.20, where the traces were measured with a resolution of $\Delta B = 0.2\,\mathrm{mT}$. Since small magnetic field values of several $10\,\mathrm{mT}$ will be analysed, the zero field position was corrected taking into account the hysteresis of the magnet. In the plot one finds, that the Hall resistance rises to $R_{xy} \approx 100\,\Omega$, before it starts to decrease. The red dashed lines at $R_{xy} = 0$ and $B = 0$ emphasise the antisymmetry of the Hall trace. Moreover, both Hall and longitudinal resistance exhibit clear oscillations in the displayed field range. The oscillations are periodic in $1/B$ and one can analyse their period by plotting the minimum index j (minima in R_{xx}) vs. $1/B$.

This is done in Fig. 4.21 for a minimum index reaching from $j = 6$ ($B = 0.4223\,\mathrm{T}$)

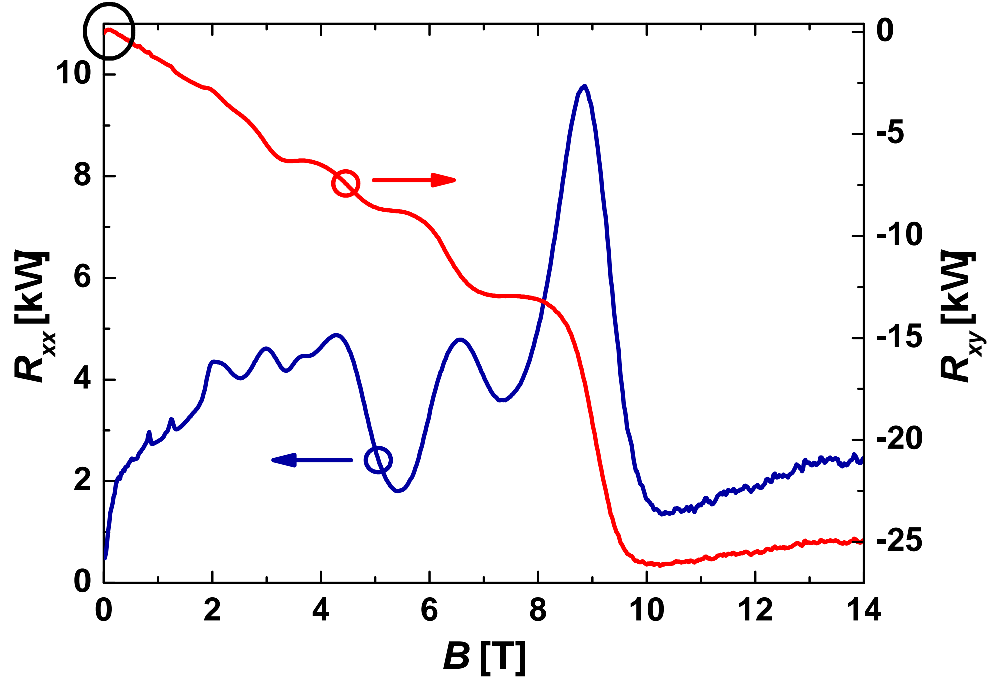

Fig. 4.19.: Hall (red) and longitudinal (blue) resistance of the sample Q2584 at $V_{\mathrm{g}} = 1\,\mathrm{V}$. The Hall trace exhibits the QHE of two p-type surface states for high magnetic fields. At very low magnetic fields one finds non-linear Hall behaviour. This region is highlighted in the plot by the black circle.

to $j = 43$ ($B = 0.0582\,\mathrm{T}$). The red line is a linear fit with the equation

$$j_{\mathrm{fit}} = 2.49\mathrm{T} \cdot \frac{1}{B} + 0.240\,. \tag{4.8}$$

Using a modified version of Eq. 3.11 the corresponding charge carrier density is determined:

$$\frac{\Delta\nu}{\Delta\frac{1}{B}} = \frac{nh}{eg}\,. \tag{4.9}$$

Here the degeneracy factor g is added, because it is a priori not known, from which kind of subsystem the oscillation sequence stems. The most probable values for this degeneracy are $g = 2$ for a spin-degenerate subsystem and $g = 1$ for lifted degeneracy. Because there is no clear splitting of the peaks in magnetic field, $g = 1$ is used and a charge carrier density of $n = 0.602 \cdot 10^{11}\,\mathrm{cm}^{-2}$ is extracted. For $g = 2$ the carrier density would result in twice the given value. Turning to the phase of

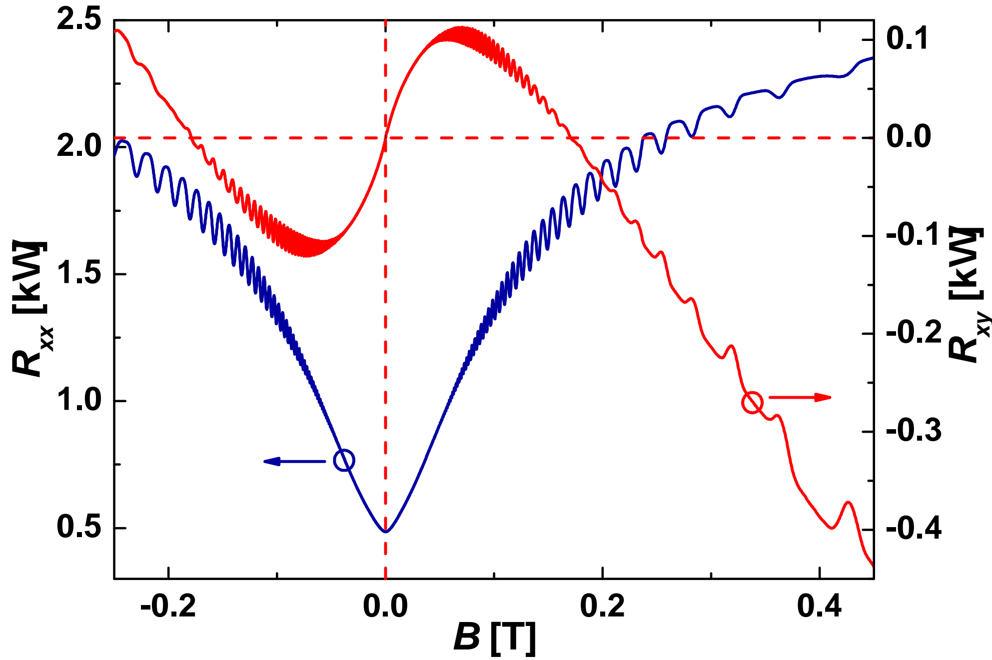

Fig. 4.20.: Close up of Hall and longitudinal resistance with respect to Fig. 4.19. The observable non-linear Hall trace of Q2584 at $V_g = 1\,\mathrm{V}$ is accompanied by clear oscillations on both resistance signals. The dashed red lines mark $R_{xy} = 0$ and $B = 0$, respectively.

the oscillations, the y-intercept is expected to vanish for a conventional 2DEG. For a Dirac band structure, it should yield $y_0 = -\gamma = -0.5$. The result obtained from Fig. 4.21 is inconsistent with either of the two values, making an identification of the charge carriers causing the oscillations difficult.
Therefore, in the inset of Fig. 4.21 the quality of the linear fit is analysed. From the residua $j - j_{\mathrm{fit}}$ it is evident, that the present fit to all data points results in a systematic error for $1/B < 7.1\,\mathrm{T}^{-1}$. By the dashed line, the data is separated into two regions. For $1/B < 7.1\,\mathrm{T}^{-1}$ a linear trend in the deviation $j - j_{\mathrm{fit}}$ is found, indicating, that for this region the slope of the linear fit j_{fit} should be increased. In the second region one more likely requires a smaller slope for the fit. Assuming a constant absolute error ΔB in the data one has to put more trust in data points with large B (small $1/B$), because their absolute error in $1/B$ is smaller. Thus, the fit is repeated for the data points left of the dashed line in the inset of Fig. 4.21, i.e. for $1/B < 7.1\,\mathrm{T}^{-1}$ or $B > 0.14\,\mathrm{T}$. For these one finds

$$j^*_{\mathrm{fit}} = 2.54\mathrm{T} \cdot \frac{1}{B} + 0.011\,, \tag{4.10}$$

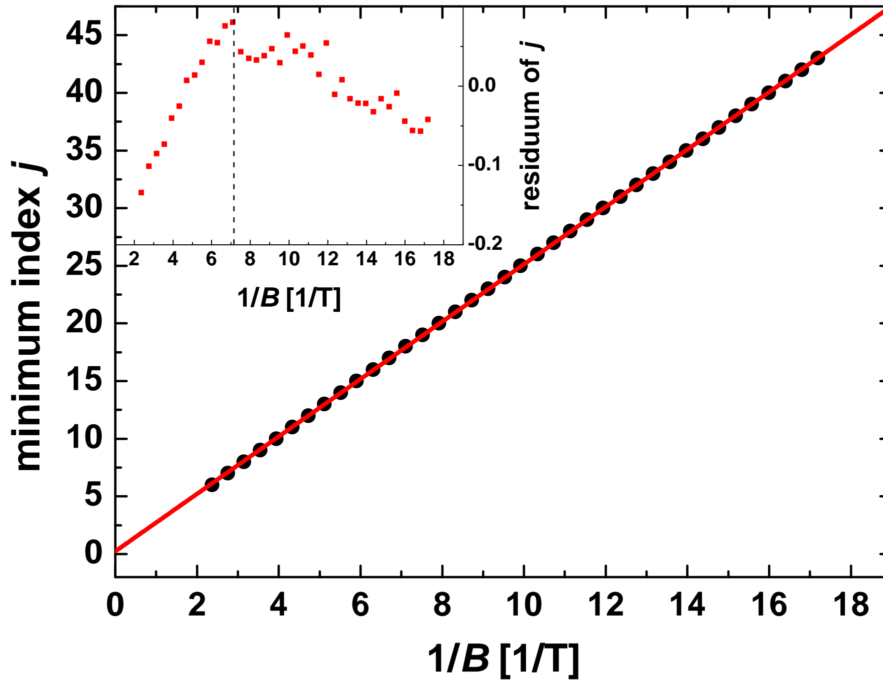

Fig. 4.21.: Minimum index vs. inverse magnetic field for the oscillations resolved in Fig. 4.20. The red line is a linear fit to the data. In the inset the residua of j are given, indicating, that for $1/B < 7.1\,\mathrm{T}^{-1}$ (left of the dashed line) a systematic error is made in the fit.

yielding a corrected charge carrier density of $n = 0.614 \cdot 10^{11}\,\mathrm{cm}^{-2}$. The value for the Berry phase within the uncertainty is consistent with $\gamma = 0$. The deviation from this result for the data at $B < 0.14\,\mathrm{T}$ (right of the dashed line in the inset of Fig. 4.21) can have several reasons. First, as already described, the absolute error $\Delta 1/B$ is increasing with $1/B$. Additionally the R_{xx} trace (see Fig. 4.20) exhibits a bigger slope for low magnetic field. This can lead to systematic errors in determining the $1/B$ position of the minima. Finally a possible remaining offset in the magnetic field after the zero-field correction will result in a bigger relative error for the minima positions at small magnetic field. Regarding all these arguments, the slope and y-intercept ($= -\gamma$) of the second fit j^*_{fit} will be taken as best fit to the data. However, the first fit demonstrates the amount of uncertainty of the extracted values. Therefore the results are $n = (0.61 \pm 0.02) \cdot 10^{11}\,\mathrm{cm}^{-2}$ and $\gamma = -0.01 \pm 0.23$.

It should be emphasised, that this γ-value extracted from j^*_{fit} was obtained for a degeneracy of $g = 1$. To discuss the change in γ for a different degeneracy number, a simple consideration can be made. For a degeneracy of $g \neq 1$ the $1/B$ positions remain unchanged, but all assigned j-values have to be taken g times as big and

therefore have an increment of $\Delta j' = g\Delta j^* = g$. The data is fitted by the rescaled linear function

$$j'_{\text{fit}} = m' \cdot \frac{1}{B} - \gamma', \tag{4.11}$$

where $j'_{\text{fit}} = g\, j^*_{\text{fit}}$. For the slope one has to take

$$m' = \frac{\Delta j'}{\Delta 1/B} = \frac{g\Delta j^*}{\Delta 1/B} = g\, m\,, \tag{4.12}$$

where m stands for the slope obtained for $g = 1$. For γ' one finds from Eq. 4.11

$$\gamma' = m' \cdot \frac{1}{B} - j'_{\text{fit}} = g\,(m \cdot \frac{1}{B} - j^*_{\text{fit}}) = g\,\gamma, \tag{4.13}$$

yielding $\gamma' = -0.02 \pm 0.46$ for $g = 2$. So for both discussed degeneracies the Berry phase γ is negative, whereas for a Dirac type 2DEG one would expect $\gamma = +0.5$. However, concerning the large uncertainty in the linear fit (resulting from the analysis of the residua), one can not exclude that the dispersion of the discussed carriers is linear or has additional linear terms. In this sense the analysis shows that a distinction of Dirac and non-Dirac electron systems is a delicate issue. It can nevertheless be concluded that in addition to the topological surface states there is a third charge carrier type active in transport.

The presence of oscillations in the Hall resistance shall now be qualitatively explained. In Chap. 3 the resistivity matrix of one carrier type in a multi carrier system was given by Eq. 3.2. To find the total resistivity, the single carrier resistivity matrices have to be inverted, added and re-inverted (see Eq. 3.3). Therefore the inverted resistivity matrix $\boldsymbol{\rho}_i^{-1}$ is calculated:

$$\boldsymbol{\rho}_i^{-1} = \frac{1}{(R_i B)^2 + (1/\sigma_i)^2} \begin{pmatrix} 1/\sigma_i & -R_i B \\ R_i B & 1/\sigma_i \end{pmatrix}\,. \tag{4.14}$$

One directly finds, that oscillations in σ_i are influencing every component of $\boldsymbol{\rho}_i^{-1}$ via the prefactor of the matrix, which results from the determinant of the original

resistivity matrix $\boldsymbol{\rho}_i$. Thus, the Hall component of the total resistivity matrix $\rho_{tot;1,2}$ is as well affected by the oscillating σ_i.

Interestingly, the mentioned third carrier type can be observed similarly in all bulk HgTe samples, independent of the thickness d_{HgTe} and of the barrier material enclosing the HgTe layer. As an example, the small field behaviour of the sample Q2451 ($d_{\mathrm{HgTe}} = 128\,\mathrm{nm}$, see Appendix A) is presented in Fig. 4.22. For

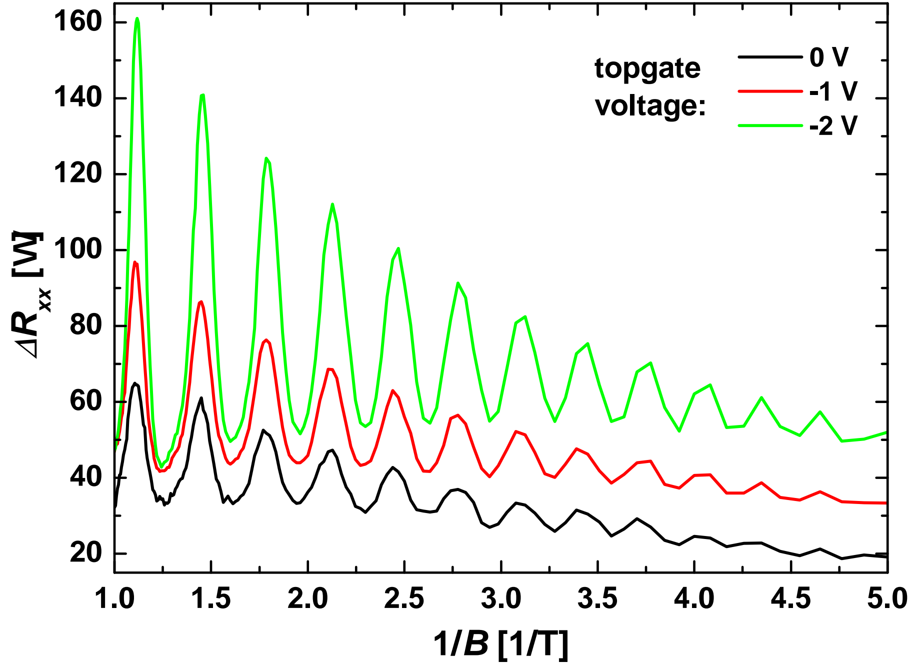

Fig. 4.22.: Oscillations of the longitudinal resistance of Q2451 ($d_{\mathrm{HgTe}} = 128\,\mathrm{nm}$) plotted against inverse magnetic field in the low field region. The zero-field resistance $R_{xx}(0\,\mathrm{T})$ is subtracted for each gate voltage.

a better comparability of the measurements at different gate voltages, the zero field resistance is subtracted. The change in resistance $\Delta R_{xx} = R_{xx}(B) - R_{xx}(0)$ is plotted vs. $1/B$ in the figure. The sample Q2451 has more than twice the thickness of Q2584 and with CdTe/HgTe/SiO_2(multi layer insulator) it has a different layer structure. However, the oscillation period and the associated carrier density ($n = 0.66 \cdot 10^{11}\,\mathrm{cm}^{-2}$ for Q2451) are very similar for both samples. From this one can conclude that the observed low field features go back to a fundamental property of the HgTe system. While the origin of these oscillations is not clear yet, one can speculate about possible reasons.

A simple explanation would be a 2DEG forming at one of the semiconductor-semiconductor interfaces due to a triangular potential well just like in heterostruc-

tures of GaAs/AlGaAs [SDC+79]. A state like this is referred to as band bending 2DEG here. The density in such a 2DEG would be expected to be gate voltage dependent if it was located between the HgTe layer and the gate electrode. Surprisingly, the oscillation frequency in Fig. 4.22 is barely affected by the gate voltage and yields a constant carrier density of $n = 0.66 \cdot 10^{11}\,\mathrm{cm}^{-2}$, while the overall shape of the traces clearly changes. This number can within error margins be treated to be equal for all three investigated gate voltages in Fig. 4.22. Thus, if a band bending 2DEG was the origin of the oscillations, it had to exist below the HgTe layer. Possible semiconductor-semiconductor interfaces are HgCdTe/CdTe and HgTe/HgCdTe for Q2584 as well as HgTe/CdTe for Q2451. The first of the three can explicitly be excluded considering Fig. 4.22: a band bending 2DEG at the HgCdTe/CdTe interface can not be the origin, otherwise Q2451 should not show the oscillations. Furthermore, a band bending 2DEG at interfaces of this kind should be found as well in all samples containing HgTe quantum wells, for which CdTe is used as the substrate and HgCdTe as the material of the lower barrier. So far, oscillations similar to the features in Figs. 4.20 and 4.22 could not be observed in quantum well samples.

Turning to the remaining interfaces, one recognizes that the 2DEG had to exist at HgTe/HgCdTe and HgTe/CdTe interfaces, respectively to explain the oscillations in samples with and without HgCdTe capping layers. From symmetry considerations one in this case would expect a band bending 2DEG at each HgTe interface for samples with HgCdTe barriers on top and bottom (e. g. Q2584). However, the upper of these should show a strong gate dependence which is not observed in the oscillation sequence. Furthermore, a spin splitting should be observed for all conventional band bending 2DEGs which by the measurements could not be substantiated so far. Therefore a bend bending 2DEG at a semiconductor-semiconductor interface does not provide a sufficient explanation of the oscillating feature.

The weak dependence on gate voltage is even more impressive for Q2584. For very low gate voltages leading to high p-type carrier densities in the surface states, one still observes the n-conducting sequence in transport. In Fig. 4.23 a) the Hall and longitudinal resistance is given for Q2584 at $V_\mathrm{g} = -8\,\mathrm{V}$ exhibiting a clear multi carrier behaviour around $B = 0\,\mathrm{T}$ in the Hall trace. In the derivatives dR_{xx}/dB (blue) and dR_{xy}/dB (red) plotted in Fig. 4.23 b) the oscillating signature can be identified. An analysis of the oscillation period yields a value of $n = (0.60 \pm 0.02) \cdot 10^{11}\,\mathrm{cm}^{-2}$ for the carrier density. The calculation is the sa-

me as for $V_\mathrm{g} = 1\,\mathrm{V}$ and the uncertainty in the carrier density is estimated to be the same as above. Remarkably, within error margins the two density values are identical. The same value results for all measurements in the gate voltage interval $-9\,\mathrm{V} < V_\mathrm{g} < 4\,\mathrm{V}$. Thus, the carriers must exist in a region of the sample, where they are very effectively screened from the electric field of the top gate.

Interestingly, a similar effect has been reported for unstrained bulk $\mathrm{Hg_{0.845}Cd_{0.155}Te}$

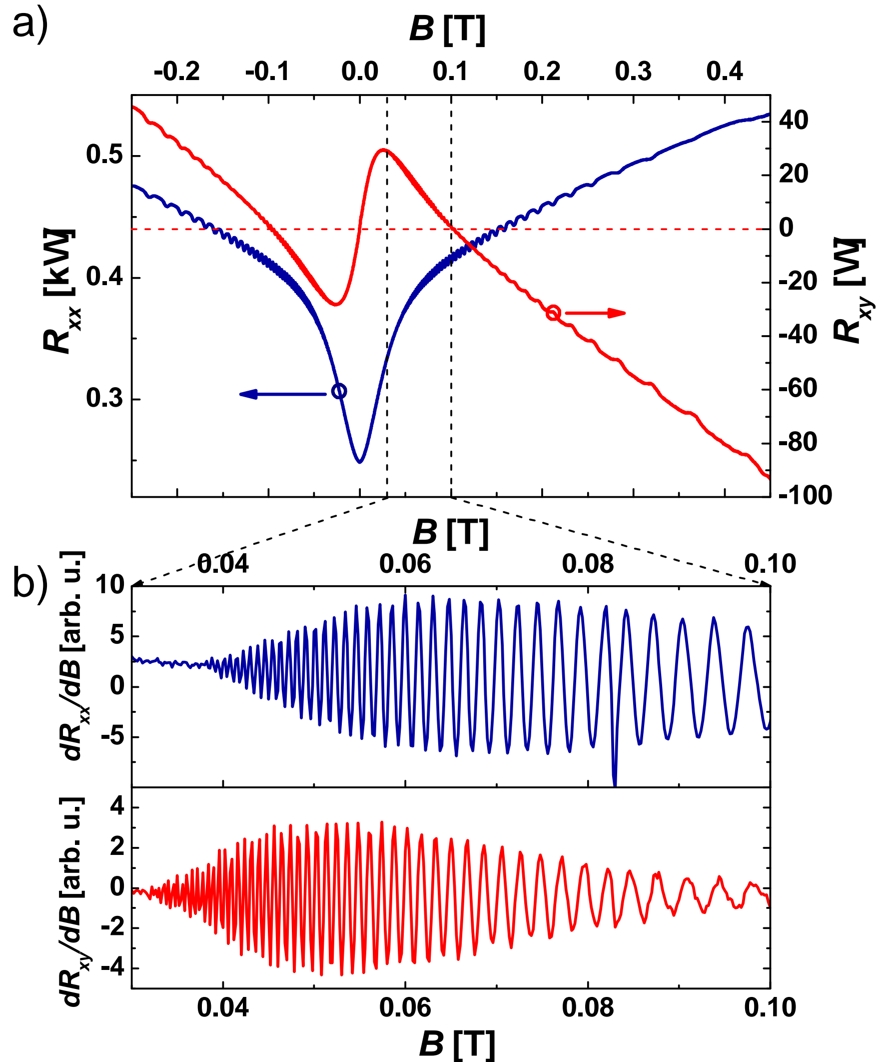

Fig. 4.23.: Hall (red) and longitudinal (blue) resistance of Q2584 at low magnetic field and $V_\mathrm{g} = -8\,\mathrm{V}$ (a). To emphasise the oscillating parts of the signals, the derivatives dR_{xx}/dB (blue) and dR_{xy}/dB (red) are displayed in (b). From the oscillation period a carrier density of $n = 0.60 \cdot 10^{11}\,\mathrm{cm}^{-2}$ can be calculated.

that has been adjusted to be a zero-gap material in Ref. [KOWV76]. The authors used a mixing (CdTe and HgTe) and annealing technique to synthesize the crystal and observed quantum oscillations down to several 10 mT. However, it is hard to judge the crystal quality and to exclude the existence of HgTe islands, that form a TI state. As the origin of the oscillations the authors propose the interaction of conduction electrons with narrow acceptor states at the conduction band edge.
This raises the question if the additional carriers are located in the bulk of the material, possibly screened from the gate by the metallic surface states. If a 3D bulk state was the origin of the observed signal, the oscillations should depend on the absolute magnetic field. Thus, by applying the magnetic field under an angle α with respect to the surface normal of the top and bottom surface state, where $\alpha = 0°$ means out-of-plane magnetic field and $\alpha = 90°$ denotes the parallel configuration, one can distinguish between states extended in 2 and 3 dimensions. While 2D states should respond to the effective out-of-plane field $B_\perp$ only, states with 3D extent should react to the total field B. The effective field can easily be calculated from geometrical considerations:

$$B_\perp = B \cdot \cos(\alpha)\,. \tag{4.15}$$

A measurement of the sample Q2584 with the angle $0° \leq \alpha \leq 80°$ is shown in Fig. 4.24. Due to the need of a sample holder with a rotatable sample the lowest temperature available for this measurement was $T \approx 1.8\,\mathrm{K}$. For all measured angles the effective field was calculated according to Eq. 4.15 and used as x-coordinate in Fig. 4.24. One finds that for all angles the minima positions in R_{xx} are nearly constant in the effective field. Note, that for $\alpha = 80°$ the trace stops at $B_\perp = 1.22\,\mathrm{T}$ according to a maximum total field $B = 7\,\mathrm{T}$. Regarding the minimum around $B_\perp = 0.91\,\mathrm{T}$ it seems, that some deviations in its position are present, which for high angles become stronger. It is estimated now, if this can result from the uncertainty in the rotation angle α.
One finds, that the uncertainty in $B_\perp$ scales with the angle α. Here, the assumption is made, that the uncertainty in the magnetic field can be neglected versus the one in the angle which is not exceeding $\Delta\alpha = 2°$. With only one uncertain entity one finds the relative error

$$\frac{\Delta B_\perp(\alpha)}{B_\perp} = \frac{dB_\perp/d\alpha\,\Delta\alpha}{B_\perp} = \frac{-B \cdot \sin(\alpha)\,\Delta\alpha}{B \cdot \cos(\alpha)} = -\tan(\alpha)\,\Delta\alpha, \tag{4.16}$$

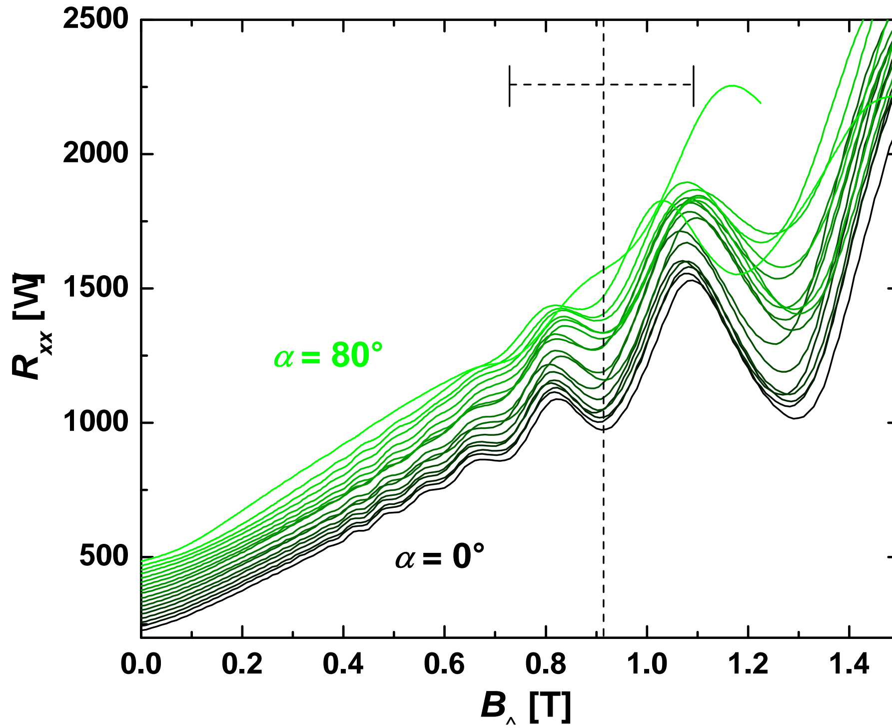

Fig. 4.24.: Oscillations of the longitudinal resistance of Q2584 at low magnetic field and $T \approx 1.8\,\mathrm{K}$. The color scale indicates the increase of α, the abscissa is the effective magnetic field $B_{\perp}$. All traces are successively offset for better visibility. By the horizontal dashed line the error margin of the $\alpha = 80^{\circ}$ trace at $B = 0.91\,\mathrm{T}$ (minimum position, see vertical dashed line) is given.

where the linear expansion in the second term is a good approximation if $\Delta\alpha$ can be treated as small error, which is the case here. For $\alpha = 80^{\circ}$ and $\Delta\alpha = 2^{\circ}$ one finds a relative error of $\Delta B_{\perp}/B_{\perp} \approx 20\%$. Thus for $\alpha = 80^{\circ}$, a shift of minima or maxima by $\Delta B_{\perp} = 0.2\,\mathrm{T}$ around $B_{\perp} = 1\,\mathrm{T}$ within the uncertainty still is consistent with constant minima positions in $B_{\perp}$. This is indicated in Fig. 4.24 by the horizontal dashed line giving the uncertainty of the minimum at $B = 0.91\,\mathrm{T}$ (see vertical dashed line). One can conclude, that the oscillations at low magnetic field originate from a 2DEG somewhere in the sample, which at first sight seems to speak against bulk carriers. However, the 2D character does not necessarily mean, that a bulk state can not be responsible, since due to a layer thickness of $d_{\mathrm{HgTe}} < 200\,\mathrm{nm}$ the bulk bands might still be split far enough by the quantum mechanical confinement to allow for the occupation of a single sub band that has 2D character. This depends on the position of the Fermi energy with respect to the bulk band structure, which could not be accessed in the demonstrated transport

experiments.

To understand the properties of the system, the data can be fitted by a three carrier conductivity model. It was described already in Eqs. 3.2 and 3.3, how the total resistivity tensor $\boldsymbol{\rho}_{\text{tot}}$ of a system with multiple carriers can be constructed from the individual components σ_i and R_i. In the low field region, there is predominantly one frequency of oscillation observable, why a model containing three types of carriers ($i = 1, 2, 3$) is used, of which only σ_3 is modulated by cosine shaped oscillations. These are incorporated along the lines of Ref. [BBB+14], that uses the results of Ref. [AFS82]. For low magnetic fields one finds

$$\sigma_3 = F_0 \left[1 - F_1 \frac{2\pi^2 k_{\text{B}} T m^*}{\hbar e B} \sinh^{-1} \left(\frac{2\pi^2 k_{\text{B}} T m^*}{\hbar e B} \right) \cos \left(\frac{\pi n_3 h}{e B} \right) \right], \tag{4.17}$$

where m^* is the effective mass of the carriers and k_{B} the Boltzmann constant. The factors F_0 and F_1 are given by

$$F_0 = \frac{e n_3 \mu_3}{1 + (\mu_3 B)^2} \tag{4.18}$$

and

$$F_1 = \frac{2 (\mu_3^* B)^2}{1 + (\mu_3^* B)^2} \exp\left[-\pi / (\mu_3^* B) \right]. \tag{4.19}$$

In the term F_1, that gives the amplitude and the exponential damping of the oscillation, the mobility is rescaled to $\mu_3^* = \tau_{\text{c}} / \tau \, \mu_3$ to take into account the possible difference between the relaxation time τ_{c} related to the broadening of Landau levels and the regular transport relaxation time τ (see for example Ref. [FSW88]). However, for practical reasons, in all following fits $\mu_3^* = \mu_3$ is used. Now the influence of temperature and effective mass in Eq. 4.17 shall be discussed. These quantities enter the equation via a prefactor $F^T = x/\sinh(x)$ to the cosine, where $x \propto m^* T$. This makes clear, that the amplitude of the oscillations depends on the product of effective mass and temperature. An estimate for the conduction band edge effective mass of HgCdTe with different Hg contents is given in Ref. [BK11], where a formula based on Ref. [Wei81] is used. The result for HgTe is $m^* = 0.03\, m_e$,

with the electron mass m_e. This result can be used as a first guess for the n-type carriers. More appropriate to the problem, the effective mass is obtained from the temperature dependent decay of the oscillations in conductivity. For the sample Q2584 this is done in Ref. [Wie13]. The author finds $m^* = 0.02\,m_e$. However, the

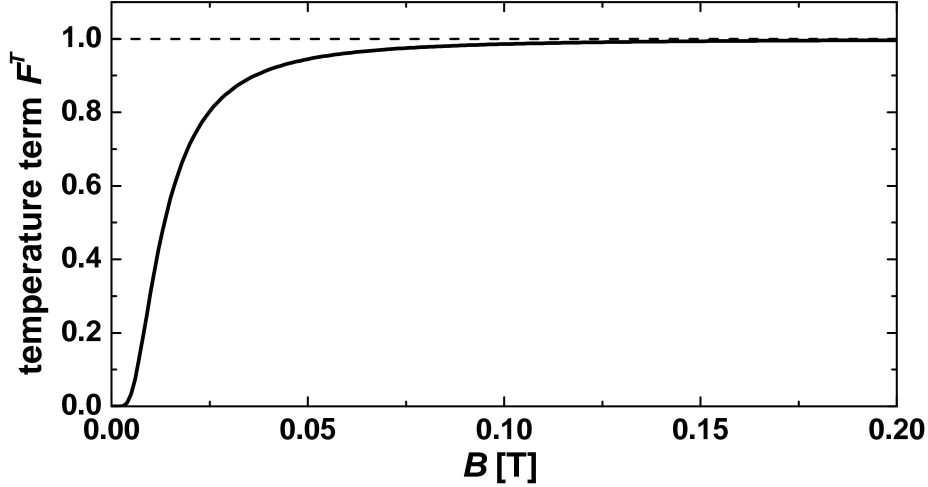

Fig. 4.25.: Temperature dependent part $F^T = x/\sinh(x)$ $(x \propto m^*T/B)$ in Eq. 4.17 for $m^* = 0.02m_e$ and $T = 0.1\,\mathrm{K}$ as a function of magnetic field. The term quickly saturates to 1 below $B = 0.2\,\mathrm{T}$.

exact number seems to be of minor importance for the quality of the fit. This can be understood, when plotting the temperature dependent term $F^T(B)$ for $m^* = 0.02\,m_e$ and $T = 0.1\,\mathrm{K}$, which is used as an estimate for the electronic base temperature of the dilution refrigerator. The dependence on magnetic field is shown in Fig. 4.25. One finds, that the influence of temperature and effective mass to the amplitude of the oscillations quickly saturates to 1 and for $B > 0.1\,\mathrm{T}$ it can already be neglected. All experimental traces fitted in this section are measured at the base temperature of $T = 0.1\,\mathrm{K}$, that is why there is no need to put more effort in a precise determination of m^* and T. For fitting purposes it is reasonable to use $m^* = 0.02\,m_e$ and $T = 0.1\,\mathrm{K}$ as constant parameters. Furthermore, the amplitude of the oscillations is affected by the mobility μ_3^* of the carriers, that influences the amplitude through the term F_1.

In Fig. 4.26 the longitudinal (blue) and Hall (red) resistance are depicted for several gate voltages below $B = 1\,\mathrm{T}$. A fit to the data is plotted in black. Hereby the fitting equations have in principle six free parameters, namely the charge carrier densities n_1, n_2, n_3 and the mobilities μ_1, μ_2, μ_3 of the three components.

From the frequency of the oscillations at small magnetic fields a value of n_3 was extracted for the gate voltages $V_g = 1\,\mathrm{V}$ and $V_g = -8\,\mathrm{V}$ above, which can be done for all gate voltages and eliminates one free parameter. Furthermore, it is assumed that the mobilities of μ_1 and μ_2 are similar. Thus, the sum $n_1 + n_2$ of the gate dependent carrier species can be inferred from the slope of the Hall trace for large magnetic fields, removing another degree of freedom from the fit equations.

Utilizing the known longitudinal resistance at $B = 0\,\mathrm{T}$, one can relate the mobility μ_3 to the others when taking into account the total conductivity as the sum $\sigma_{\mathrm{tot}} = \sigma_1 + \sigma_2 + \sigma_3$:

$$\mu_3 = \frac{\sigma_3}{n_3 e} = \frac{\sigma_{\mathrm{tot}} - \sigma_1 - \sigma_2}{n_3 e} = \frac{1/\rho_{xx}(B=0) - n_1 e \mu_1 - n_2 e \mu_2}{n_3 e}, \tag{4.20}$$

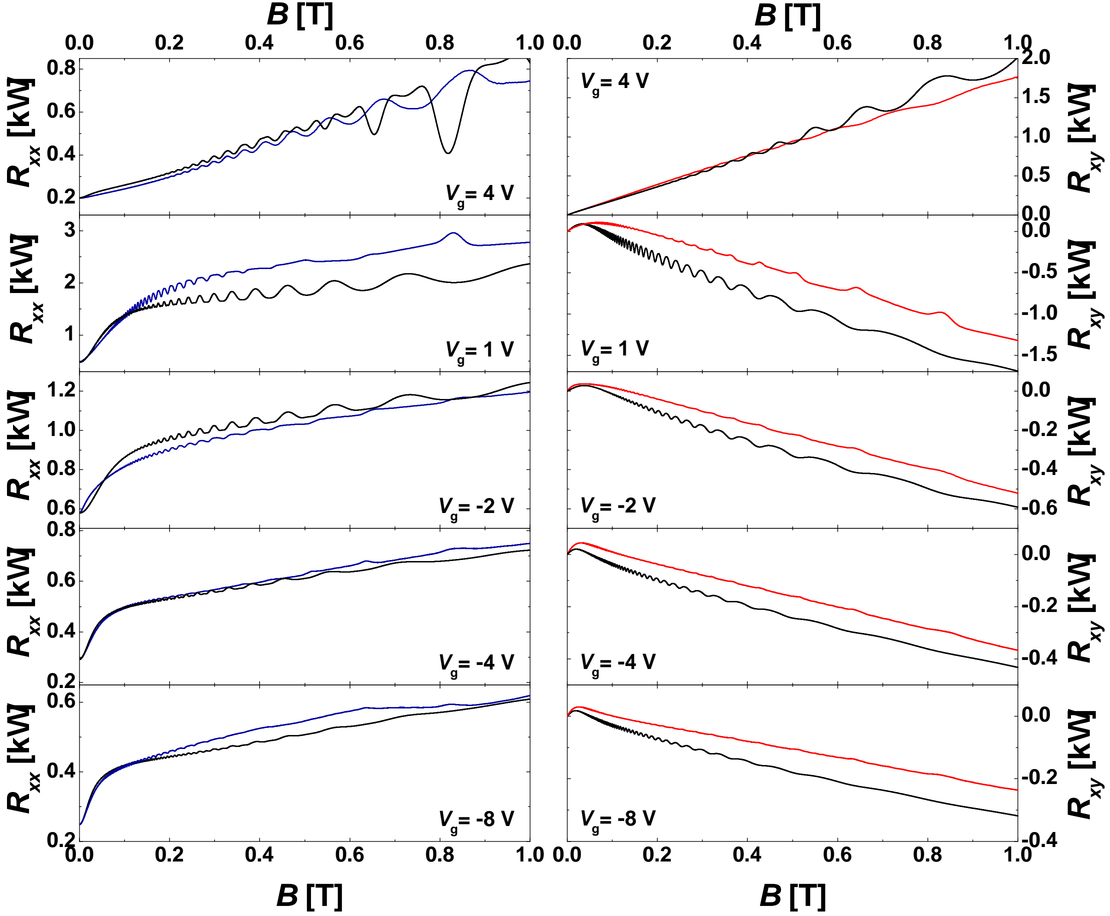

Fig. 4.26.: Longitudinal resistance (left, blue) and Hall resistance (right, red) data for sample Q2584. The black traces are fits to the data obtained by a classical three carrier model, where one component is described by cosine shaped oscillations (see Eq. 4.17).

leaving three free parameters available. Finally it should be mentioned, that the set of three parameters for a given gate voltage is used to fit the Hall and longitudinal resistance, respectively. In Fig. 4.26 it is shown, that the three carrier model can qualitatively be taken as an explanation for the measurement data in the complete gate voltage range. The oscillations in both signals are present also in the fit traces and match in amplitude and phase at low fields $B < 0.5\,\mathrm{T}$. For higher fields, there seems to be a disagreement in the phase relation. This can be a result of the non-classical limit, where the Landau energy gaps ($E_\mathrm{L} = \hbar\omega_\mathrm{c}$) between the levels open far enough to let the description by a cosine function fail. An indication, that the oscillation is not very well described by a cosine function for $B \geq 0.5\,\mathrm{T}$ can be found in Fig. 4.20, where the peak shape is deformed significantly already for magnetic fields below $B = 0.5\,\mathrm{T}$.
Another observation is that the Hall signal of the p-type carriers is over-estimated by the fit function. In the region of strong p-type influence (high B) measurement and fit trace run parallel. A good agreement is also given for very low magnetic fields, where the signal is dominated by the n-type component. However, in the intermediate region, a discrepancy between the experiment and theoretical description is found. One can exclude an n-type density different from $n_3 = 0.61\cdot 10^{11}\,\mathrm{cm}^{-2}$, since the value was obtained from the frequency of the oscillating part in the data. The disagreement in Hall traces could point to a degeneracy of the n-type carriers. This would lead to the same oscillation frequency, but give more weight to the positive Hall contribution. However, fitting attempts with a degeneracy of $g = 2$ did not give a better quantitative result. It turned out, that including a fourth type of carriers of $n_4 = 0.61 \cdot 10^{11}\,\mathrm{cm}^{-2}$ and a mobility $\mu_4 \neq \mu_3$ indeed increased the quality of the Hall fit. Doing so could be motivated by the symmetry of the device in z-direction. If the third carrier species existed on a surface, this symmetry would require a mirror state on the other side (top/bottom) and therefore an even number of carrier species. However, a better fit in the case of assuming a fourth carrier type is not surprising because additional degrees of freedom are provided introducing the additional parameters n_4, μ_4. Therefore, we do not further follow this idea here.

The parameters, that were used in the three carrier model are listed in Tab. 4.1. The robustness of the third carrier type again is visible from the nearly constant value of n_3, that only deviates for the highest gate voltage $V_\mathrm{g} = 4\,\mathrm{V}$. For this voltage, however, there are other n-type components with very high mobilities

Fit parameter	V_g= 4 V	V_g= 1 V	V_g= -2 V	V_g= -4 V	V_g= -8 V
n_1 / 10^{11} cm^{-2}	2.2	-1.3	-5.5	-8.0	-12.0
μ_1 / 1000 cm^2/Vs	220	7.0	8.0	9.0	7.0
n_2 / 10^{11} cm^{-2}	0.8	-2.8	-6.0	-8.0	-11.0
μ_2 / 1000 cm^2/Vs	500	40	27	37	32
n_3 / 10^{11} cm^{-2}	0.79	0.61	0.61	0.61	0.61
μ_3 / 1000 cm^2/Vs	88	440	210	460	520

Tabelle 4.1.: Parameters used for the fit in Fig. 4.26. A positive sign of the charge density corresponds to n-type carriers.

present in addition. The model assumes that for low magnetic fields only n_3 leads to oscillations in the resistance signals because it has the highest mobility. This assumption can not be hold for $V_g = 4\,\text{V}$ considering the parameters given in Tab. 4.1, that indicate a massive increase in the mobilities μ_1 and μ_2. Therefore, the numbers for this gate voltage can not be taken as very reliable and a modified model would be needed to correctly describe the data. It can not even be excluded that the assignment of carrier species for this gate voltage is erroneous.
For the gate voltages $V_g < 4\,\text{V}$ we can identify two contributions n_1 and n_2 with slightly different gate influence and approximately constant mobilities. A mobility ratio of about $\mu_2/\mu_1 \approx 4$ can be determined. From the behaviour at high magnetic fields we expect contributions of two Dirac surface states, for which the density and mobility parameters (n_1, n_2, μ_1, μ_2) of Tab. 4.1 are reasonable. The evolution of the two densities with the gate voltage is plotted in Fig. 4.27. Hereby the gate influence onto the carrier density n_1 is stronger. Therefore, this density has to be associated with the upper TI surface. This is consistent with the mobility μ_1 being the lower one of (μ_1,μ_2). Due to the assumption $\tau_c = \tau$ we made above, the given mobility values have a huge uncertainty and should only be considered a qualitative evidence, that the presented understanding of the physics is correct.
One can conclude that qualitatively the multi carrier physics in the sample is confirmed by the model. The occurrence of pronounced oscillations in the Hall and longitudinal resistance down to very low magnetic fields of several 10 mT can be related to an additional n-type carrier species with low carrier density $n_3 = 0.61 \cdot 10^{11}\,\text{cm}^{-2}$ and high mobility $\mu_3 \approx 450 \cdot 10^3\,\text{cm}^2/(\text{Vs})$.

Now the rise of the longitudinal resistance shall be commented, visible in Fig. 4.26

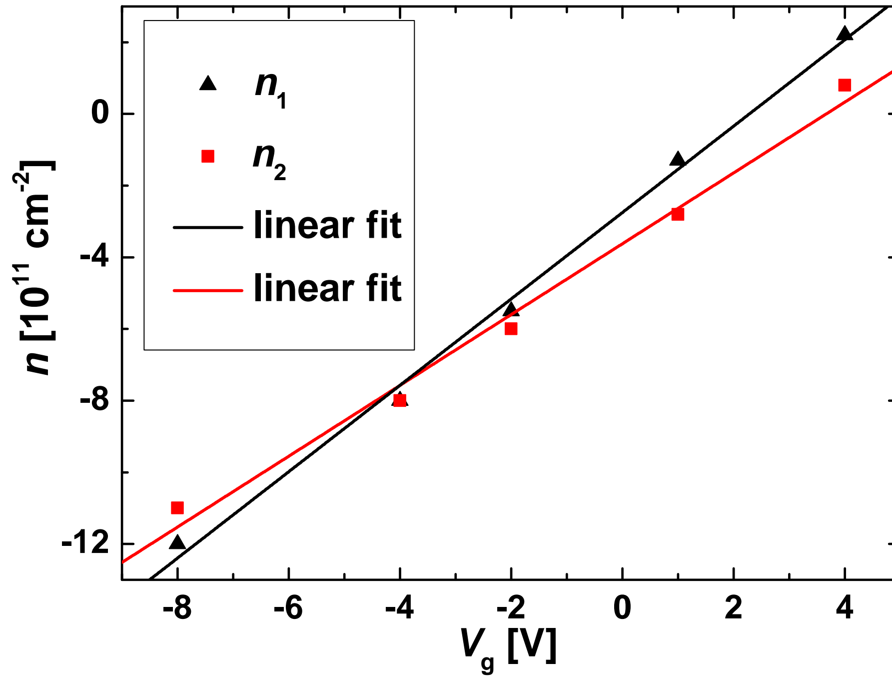

Fig. 4.27.: Carrier densities of the surface states of Q2584, which result from a fit of the magneto-resistance with a three carrier model (values in Tab. 4.1). The black and red line are linear fits.

e.g. for $V_g = -4\,\mathrm{V}$. In the range of $0.2\,\mathrm{T} < B < 1\,\mathrm{T}$ the magneto-resistance seems to be linearly depending on the magnetic field. A linear magneto-resistance for instance in Ref. [ZYF+11] is related to the properties of topological insulators. However, it is possible to reproduce the linear behaviour quite closely by a classical multi carrier fit. One can show, that the linear expansion coefficient of the calculated $R_{xx}(B)$ for the used parameters (see Tab. 4.1) indeed exceeds the higher order coefficients for an expansion around $B_0 \neq 0$. Nevertheless, if one plots the calculated longitudinal resistance for a larger range, a saturation of the trace is observed. In Fig. 4.28 the fit function and the measurement data for $V_g = -4\,\mathrm{V}$ are compared up to a magnetic field of $B = 5\,\mathrm{T}$. Here the linear behaviour in the range of $0.2\,\mathrm{T} < B < 1\,\mathrm{T}$ is visible in both traces. For higher magnetic field the fit function seems to saturate a bit earlier and lower than the measured data. This can be an effect of the breakdown of the classical description used for the fit. One finds the breakdown confirmed by the onset of SdH oscillations from the surface states, clearly visible for $B > 4\,\mathrm{T}$. It also has to be mentioned that the fit parameters were not adapted to optimize the fit for $B > 2\,\mathrm{T}$. Nevertheless the comparison in Fig. 4.28 gives rise to understand the linear part of the trace as to result from the interplay of multiple carrier types, nicely described by classi-

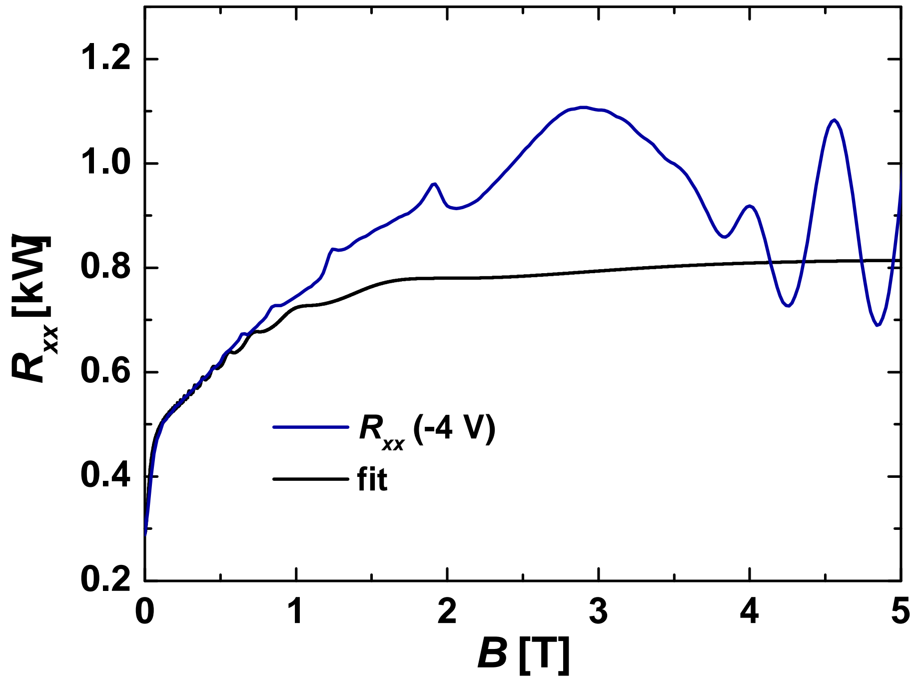

Fig. 4.28.: Longitudinal resistance (blue) and fit function (black) for sample Q2584 at the gate voltage $V_g = -4\,\mathrm{V}$. A region of magneto-resistance dominated by linear behaviour is observable in the range of $0.2\,\mathrm{T} < B < 1\,\mathrm{T}$, followed by saturation of both traces.

cal transport equations. The extent of the linear region obviously depends on the density and mobility parameters of the involved carriers. Therefore, one can have serious concerns about any correlation between linear magneto-resistance features and the topological nature of the host material.

In this section it was phenomenologically explained, how the presence of a third carrier species can lead to the observed longitudinal and transverse resistance signals and mobility and density parameters were found to fit the experimental traces. However, the origin of the additional carriers is not clear. With the evaluation of the experiments presented above one can imagine two possibilities, both not in perfect agreement with the picture constructed so far.
First, the oscillations corresponding to n_3 can result from a bulk state. The stability against top gate voltage is explainable via screening of the bulk by the metallic surface states. This is also substantiated by the nearly unperturbed QHE physics observable in n- and p-type transport. The reduced dimensionality of the state must result from the confinement by the finite layer thickness d_{HgTe}. Problematic in this interpretation is the strong dependence of the lower surface state on the ga-

te voltage. If a strong screening of the top gate was present, the lower surface state should not be affected as well. Additionally, a clear spin splitting of the oscillating signal is not observed in the data. This, however, is expected for any trivial bulk state. For the very high mobility μ_3 and the high g-factor of HgTe (values range between 15 and 55 for HgTe 2DEGs, see Refs. [WCC95],[ZOPJ$^+$04],[BLT$^+$10]) a spin-degenerate band should split in the investigated range of magnetic field due to the Zeeman effect. Furthermore, the two samples shown above have thicknesses of $d_{\text{HgTe}} = 60\,\text{nm}$ and $d_{\text{HgTe}} = 128\,\text{nm}$, respectively. A change in d_{HgTe} by a factor of 2 changes the confinement energy drastically and one would expect a dependence of the signature of the bulk state on d_{HgTe}. However, the observed feature is very similar for these two samples.
The alternative explanation of the origin of the high mobility component connects it to the bottom topological surface state. In this model the screening by the top surface is responsible for the independence on gate voltage. A spin splitting should not be observable for a Dirac surface state and the state is 2D naturally. It is also reasonable, that a high mobility is possible close to the clean, protected, lower HgCdTe/HgTe interface. Finally, the weak dependence of the associated density on the thickness of the HgTe layer supports this hypothesis. However, the odd integer sequence in QHE data and the Landau level fan charts are interpreted to originate from two independent Dirac type surfaces with carrier concentrations controllable by the gate voltage. Therefore, the alternative explanation contradicts these ideas and one would have to find a different description of the high field data, to make the association of the oscillating feature with the lower surface state stick.

A fundamental difference between the two hypotheses is the response of the oscillation frequency to a back gate voltage. While in the first case, the frequency was constant, it would be changeable by back gate voltage in the latter. Therefore, in the next chapter we want to focus on back gating attempts.

5. Back gate measurements

In this thesis the well-pronounced Landau levels observed in HgTe devices are interpreted to originate from the topological surface states. A large fraction of the presented measurements are nicely described by this hypothesis. However, the gating behaviour and the observation of a third, gate voltage independent carrier species legitimate the request for an unambiguous association of Landau levels to the corresponding surface. Therefore, devices equipped with top and back gate electrode are focussed on in this chapter. The intention is to study the effect of each gate on the two sets of Landau levels and on the oscillation of the resistance signals in low magnetic fields (see Ch. 4).
To realize back gate electrodes in transport devices a simple approach is the use of an oxidized silicon substrate on that the investigated material is deposited. Applying voltage to the silicon substrate enabled control over the charge carrier density e.g. for graphene devices [NGM+04]. For strained HgTe, the commercially available, insulating CdTe substrates are rather thick (around 800μm), such that the deposition onto a gateable substrate yields very low gate efficiencies. Although, in principle, the CdTe substrate could be thinned down from the back side to solve this problem, another approach seems more promising: It is known that with some effort the growth of HgTe is possible starting with a GaAs substrate. This can be doped and used as a back gate electrode. Due to the huge lattice mismatch between GaAs and HgTe, intermediate layers are required. The goal is to continue growing strained HgTe on top of (001)-oriented CdTe. To do so, first a thin layer of ZnTe (relaxed after several nanometres, see Ref. [ESSP+93]) is deposited. The lattice constant of ZnTe lies between the ones of CdTe and GaAs ($a_{ZnTe} = 0.6103\,\text{nm}$, see Ref. [SHDN96]). On top of the ZnTe one can grow (001)-oriented CdTe in decent quality, relaxed to its lattice constant a_{CdTe}. Thus, all structures grown on CdTe substrates can be build as well starting with a GaAs wafer (for details see Ref. [Ame15]). The doping to high n-type carrier densities in the GaAs substrate is achieved by the implementation of Si. The insulating layer between GaAs substrate

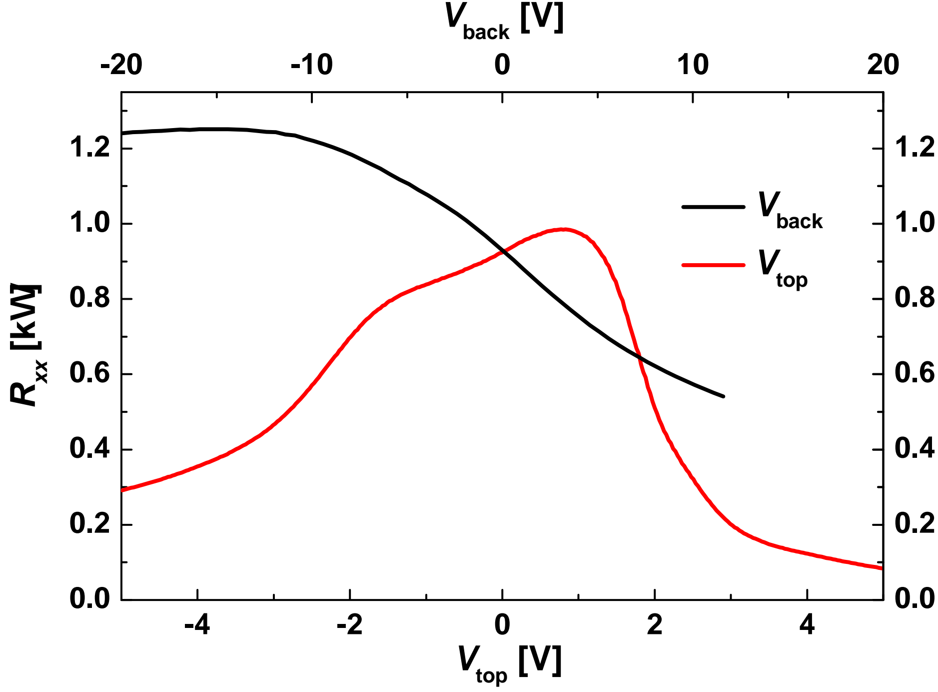

Fig. 5.1.: Longitudinal resistance of the sample Q2780 for a variation of top (red) and back gate voltage (black). Measurements are taken at 1.8 K each with the remaining gate grounded. The zero positions of both gate voltage axes coincide in the plot.

and HgTe layer is provided by the ZnTe/CdTe barrier. However, the band gap in these materials is $E_g < 2.3\,\text{eV}$ (see Ref. [Ada11]). Thus, a finite voltage depending on the exact barrier configuration is expected to lead to a leakage through the ZnTe/CdTe barrier. This can be investigated by an analysis of the current flowing between back gate electrode and HgTe layer while applying a back gate voltage. As a proof of principle, Fig. 5.1 shows a measurement of the longitudinal resistance of Q2780 under variation of the back gate voltage V_{back} (black) and the top gate voltage V_{top} (red) at $B = 0\,\text{T}$. The back gate leak current was confirmed to be $< 1\text{nA}$ in the range $-25\,\text{V} < V_{\text{back}} < 11.6\,\text{V}$, determining the cut-off on the positive voltage side in Fig. 5.1. The two traces were measured each with the complementary gate grounded. One finds, that the resistance traces besides the point at zero gate voltage do not match. Also by rescaling the back gate axis to correct for the difference in top and bottom gate efficiency the two measurements cannot be aligned. This is obvious from the different slope at $V_{\text{top}} = V_{\text{back}} = 0\,\text{V}$ as well as the unequal resistance values of the maxima. For a completely symmetric structure one can expect a similar influence of top and bottom gates to the resistance traces. Here, the unequal mobilities and densities of the surface

states break the spacial inversion symmetry. However, one can conclude from Fig. 5.1 that both gates affect the transport properties of the device.

5.1. Top gate - back gate map

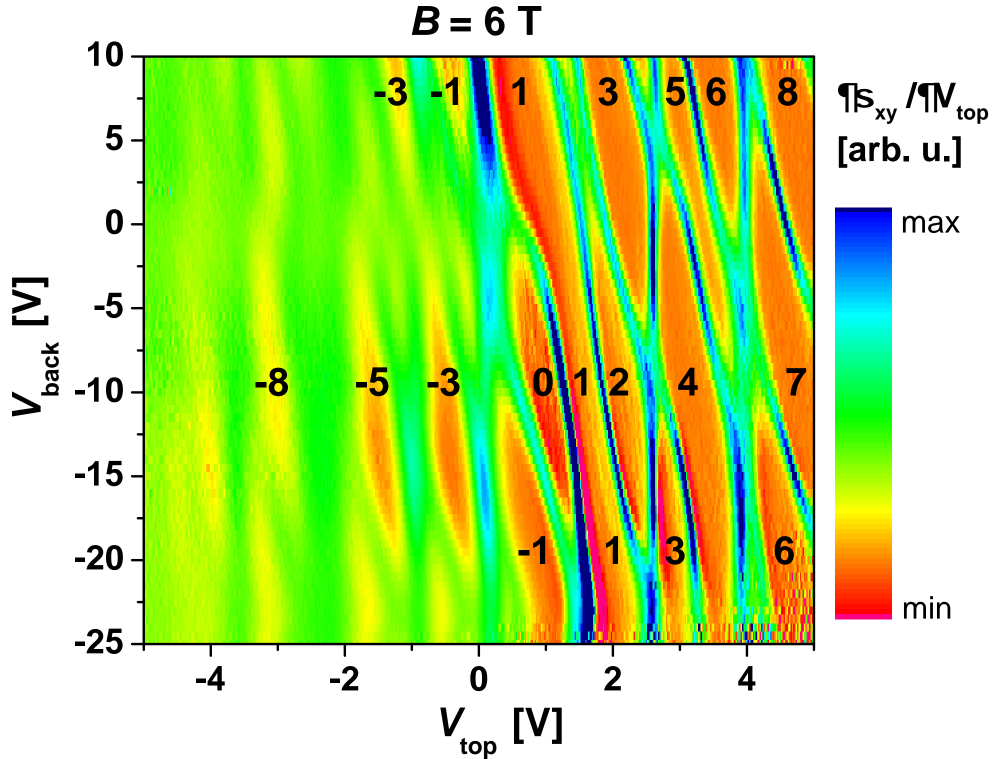

Fig. 5.2.: Top gate vs. back gate map: Derivative of the Hall conductivity with respect to the top gate voltage for Q2780 at $B = 6\,\mathrm{T}$. Blue/green areas mark the position of Landau levels, red areas correspond to plateaus in the Hall conductivity. Numbers denote the quantum Hall index i.

To get a more detailed understanding of the gating behaviour, in the following the response of the sample is investigated at different constant magnetic fields and dilution refrigerator temperatures, where Landau levels are well resolved. In Fig. 5.2 a map of Landau levels is shown for varied top and back gate voltage. The positions of the Landau levels (blue/green areas) are accompanied by high values of the derivative $\partial\sigma_{xy}/\partial V_{\mathrm{top}}$. Between the Landau levels one finds plateaus in the Hall conductivity, with quantum Hall indices i, as indicated in Fig. 5.2. Plateaus in σ_{xy} yield a zero derivative in the map (red/orange areas). As a general trend, the Landau levels are much narrower in the n-conducting region, where the plateaus

are labelled by positive integers. In the p-conducting region there are only a few plateaus, for which the quantum Hall index can be clearly assigned.
Interestingly, one finds different slopes $\partial V_{\text{back}}/\partial V_{\text{top}}$ for different Landau levels in Fig. 5.2. Since the magnetic field is fixed, the slopes of the levels only reflect the gating situation in the device. Levels that run parallel to a gate axis are independent of the corresponding gate voltage. To illustrate this, the expected behaviour for perfectly separated gate influence on top and bottom Landau levels (100% screening) is sketched in Fig. 5.3 a). There, the levels form a pattern of perpendicular lines, because a change of carrier density and thus a transition between Landau levels of the top surface state (red levels) is only caused by the top gate and vice versa. Assuming an identical gate influence of both gates on each surface (no screening), one obtains a behaviour as demonstrated in Fig. 5.3 b). Here, both surfaces are affected in the same way by the gates, making Landau levels of top and bottom surface run parallel in the plot.
However, none of the two extreme cases displayed in Fig. 5.3 seems to apply to the measurements presented in Fig. 5.2. To discuss the Landau level traces it makes sense to focus on the n-conducting part of the measurement, since the levels are much better resolved in this region. In Fig. 5.4 sets of black and red lines were drawn as a guide to the eye into the map. In each set all lines are parallel to each other. To first order, the data can be described by the two groups of lines. The slopes of the lines imply that the top gate influences the black and

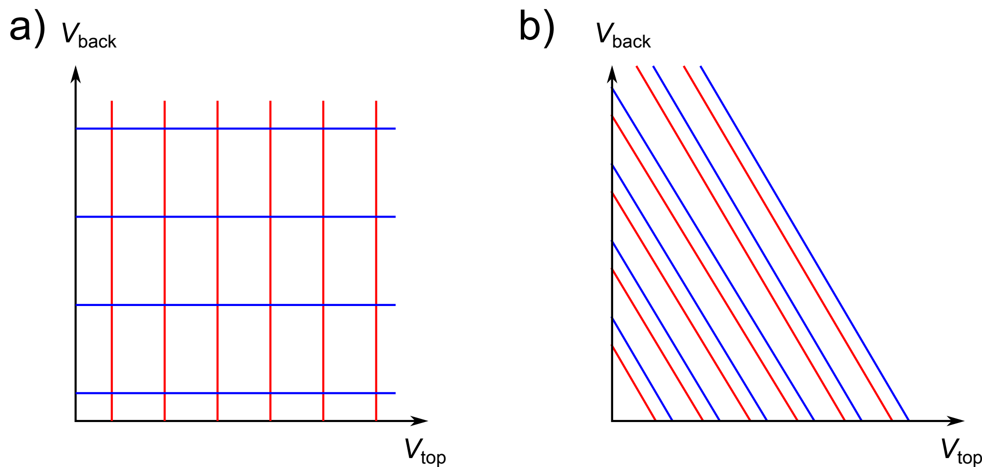

Fig. 5.3.: Sketch of the expected behaviour for 100% screening (a) and zero screening (b) in a double gated 3D TI at finite magnetic field. Red lines represent LLs of the top surface state, blue stand for the bottom surface. The voltages V_{top} and V_{back} denote the top and back gate voltage, respectively.

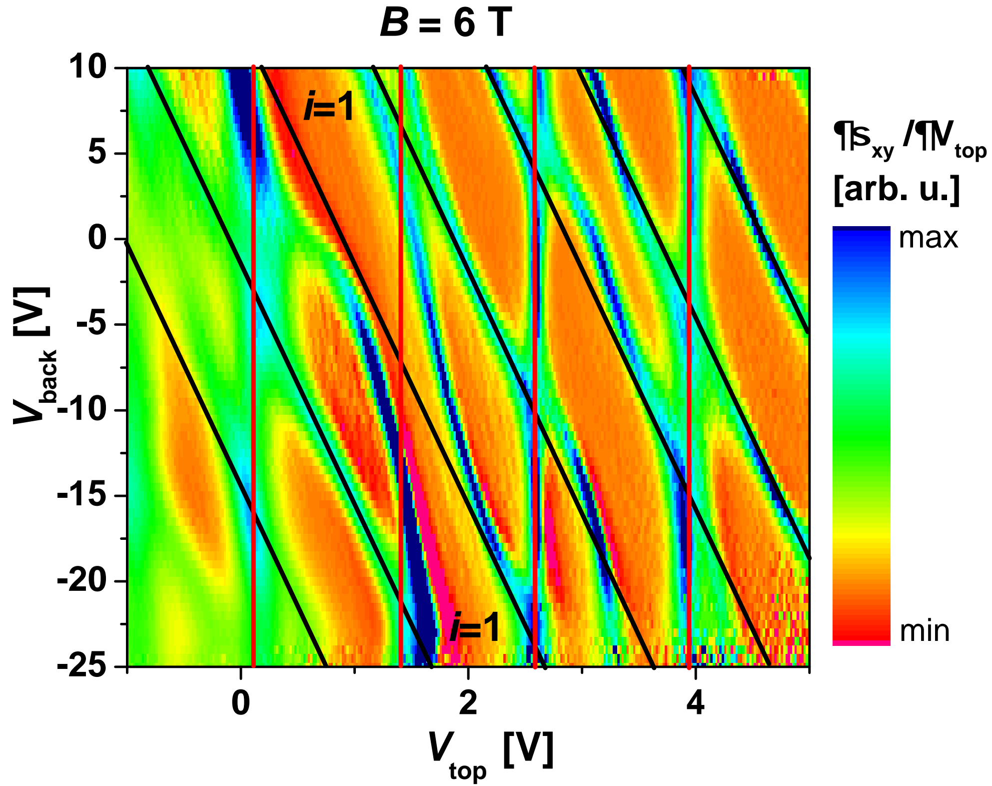

Fig. 5.4.: Top gate vs. back gate map: n-region of Fig. 5.2 at $B = 6\,\mathrm{T}$. Red and black sets of parallel lines are guides to the eye.

red set of Landau levels, while the back gate only affects the black series. A possible explanation is a difference in the screening properties of top and bottom surface states. It is plausible, that different mobilities in top and bottom surface influence the screening behaviour. Further, it has been demonstrated above that the bottom surface state compared to the top one by tendency exhibits a higher mobility. As a result, the larger screening by the bottom surface inhibits the back gate influence onto the top layer. This is consistent with the experiment, where the red series of Landau levels is mostly unaffected by the back gate. The finite top gate influence onto the bottom 2DEG (black lines) thus is an indication for non-perfect screening by the top surface state. An alternative explanation might be the top gate profile, which deviates from the shape of a perfect plate capacitor. The profile is sketched in Fig. 5.5. For simplicity, cap and buffer layers were omitted in the sketch. The top gate profile results from the evaporation process. From the sketch it can be seen that the top gate influences the lower surface state due to stray fields at the mesa edge. However, comparing the width of the Hall bar $W = 200\,\mu\mathrm{m}$ to the mesa height, that including the insulator does not exceed $h = 300\,\mathrm{nm}$, it is questionable, if this effect is strong enough to be detectable in

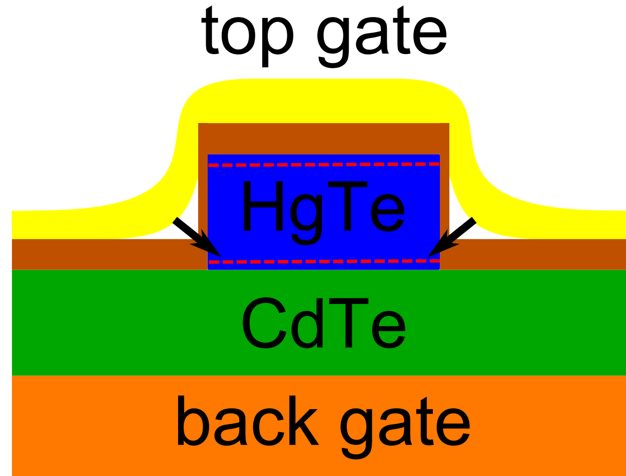

Fig. 5.5.: Sketch of the top and back gate profile. Surface states are represented by red dashed lines. The insulator of the top gate electrode is depicted as brown layer. By black arrows a possible influence of the top gate to the lower surface state is indicated.

transport experiments. Nevertheless, it might be interesting to investigate the top gate influence on the lower surface state in a test sample, where the structure is planarized before the gate is deposited.
In Fig. 5.4 a clear deviation from the first order description given above is visible for the quantum Hall index $i = 1$. Here, the expected crossing of a black and a red level at the coordinates ($V_{top} = 1.4\,\mathrm{V}$,$V_{back} = -7.2\,\mathrm{V}$) is not observed in the dataset. In contrast, the levels seem to anti-cross and run parallel in a finite region. This, according to Fig. 5.3 b), points to a reduced screening. It can be concluded, that the screening properties of the surface states change with the carrier density. Especially for low occupation (around the zero levels) the screening brakes down. Also the higher levels do not perfectly follow the black and red lines drawn as a guide to the eye in Fig. 5.4. Therefore, the screening properties are likely to change depending on the position of the Fermi energy with respect to the last occupied Landau level. This idea can be motivated by the results obtained in Ref. [WGG88], where the screening properties of a 2DEG are investigated depending on the DOS and the magnetic field.
A further observation concerns the period of the black level sequence. Here, a deviation of the expected behaviour is found. The distance between the levels is decreased for higher quantum numbers. Especially the levels going through the points ($V_{top} = 4\,\mathrm{V}$,$V_{back} = -4.5\,\mathrm{V}$) and ($V_{top} = 4\,\mathrm{V}$,$V_{back} = -16\,\mathrm{V}$) seem to be too close to each other. Considering the changes in the screening properties, one can

imagine, that the broken periodicity results from a non-linear dependence of the carrier density of the black sequence on the applied gate voltages.
Since the map in Fig. 5.4 was measured at a constant magnetic field of $B = 6\,\mathrm{T}$ the degeneracy is constant in each occupied Landau level. Counting the Landau levels that cross the Fermi energy in a certain gate voltage interval a gate efficiency can be calculated for the top and back gate. One obtains

$$\frac{\Delta n}{\Delta V_{\mathrm{top}}} = \frac{11 \cdot eB/h}{6\,\mathrm{V}} = 2.7 \cdot 10^{11}\,\mathrm{cm}^{-2}/\mathrm{V} \tag{5.1}$$

and

$$\frac{\Delta n}{\Delta V_{\mathrm{back}}} = \frac{3.5 \cdot eB/h}{35\,\mathrm{V}} = 1.5 \cdot 10^{10}\,\mathrm{cm}^{-2}/\mathrm{V}. \tag{5.2}$$

Here, Landau levels from both sets were taken into account, to estimate the total density change caused by each gate. As a result, there is roughly a factor of 20 between the gate efficiencies of top and back gate, confirmed by measurements on HgTe quantum wells with identical gate arrangement. Comparing the influence of the top gate on the red and black levels, one makes a peculiar observation: The number of black levels crossing the Fermi energy along a line of constant V_{back} in Fig. 5.4 (i.e. during a top gate sweep) is larger than the number of red levels. At constant magnetic field this means that the top gate influence on the lower surface state is even larger than the influence on the top surface. This result is confusing, since for metallic systems such a behaviour is electrostatically unintuitive. In further measurements the top and back gate influence should be studied in detail. Unfortunately, the investigation of back and top gate dependent transport of Q2780 could not contribute to a clarification of the association of the two Landau level sequences to top and bottom surface state. In contrast, it rises further questions about the interplay of these 2D electron gases, which must be non-trivial, if the discussed association is correct.

5.2. Higher magnetic fields

So far the discussion was concentrated on the map at the magnetic field value $B = 6\,\mathrm{T}$. However, also measurements at higher constant magnetic field are available. In Fig. 5.6 the Landau levels in the gate voltage range investigated in Fig. 5.4 are depicted for higher magnetic fields. The values are $B = 8\,\mathrm{T}$ in Fig. 5.6 a) and $B = 11\,\mathrm{T}$ in Fig. 5.6 b). Besides the expected increase of level spacing with the magnetic field due to an increased degeneracy, another interesting observation

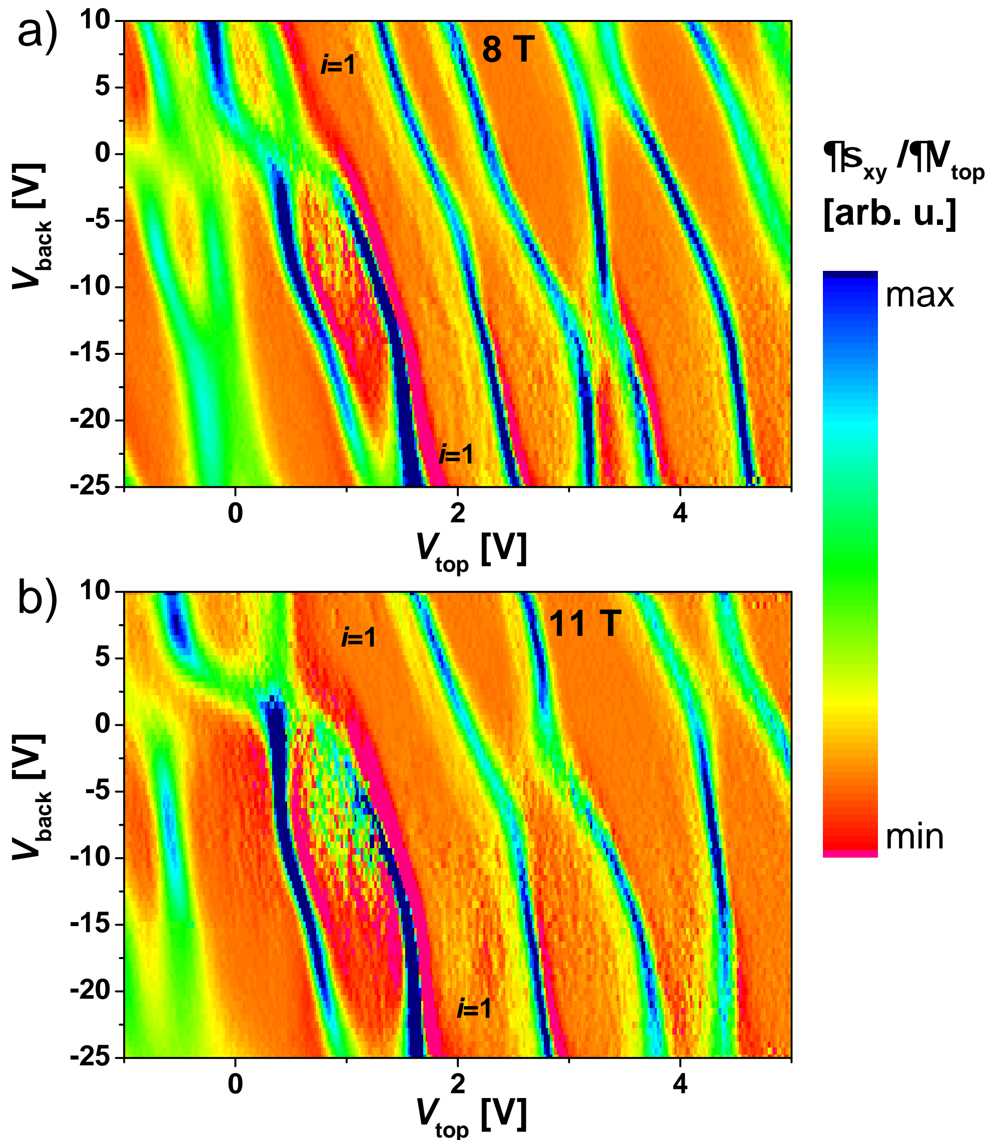

Fig. 5.6.: Top gate vs. back gate map: Evolution of Landau level behaviour for increasing magnetic field. Displayed are $B = 8\,\mathrm{T}$ in a) and $B = 11\,\mathrm{T}$ in b). The gate voltage range is identical to the one in Fig. 5.4.

can be made. Several Landau level crossings observed in Fig. 5.4 are turned into anti-crossings. This can be substantiated in Fig. 5.6 a) by continuous orange areas representing regions of Landau level indices $i = 1$ (marked in the graph) and $i = 2$. At 11 T areas of equal quantum Hall index are connected in the complete gate range investigated. Thus, for higher fields one finds enhanced anti-crossings of Landau levels for all indices. One can assume that the screening has become poorer with increasing field, moving the Landau levels of different sets closer to a parallel configuration similar to the sketch in Fig. 5.3 b).

Another possible reason for an influence of both top and bottom gate onto the black series of Landau levels in Fig. 5.4 must be discussed. If the sequence of Landau levels stemmed from a bulk state, it could easily be explained, that the influence of top and bottom gate is equal (if rescaled to equal efficiency). Following the data one had to assume that a single sub band is occupied for the investigated gate voltages. Irregularities in the periodicity of the black series of levels in Fig. 5.4 could then result from a spin splitting, expected for bulk sub bands. However, some questions can not be answered within this hypothesis. One can ask why the lower surface state shows no transport signature at all. Although only a limited back gate range could be accessed in the experiment, the influence on the lower surface state should be bigger than on the bulk state. Therefore one would expect at least one of the Landau levels of the lower surface to be resolved in Fig. 5.4. Furthermore, a larger top gate influence onto a bulk state (black) than onto the top surface state (red) is also not reasonable. Therefore, explaining the two independent series of Landau levels by the presence of the topological surface states yields a better agreement with the data even with some problems unresolved.

Now the behaviour is investigated for small magnetic field. The idea was to find a top gate voltage that allows for an unambiguous observation of the oscillations described in Ch. 4 and to test the influence of the back gate voltage. In Fig. 5.7 the longitudinal resistance of Q2780 is plotted for different top gate voltages. Unfortunately, oscillations in the signal are only present for magnetic fields $B > 1\,\mathrm{T}$ and top gate voltages $V_{\mathrm{top}} > 1\,\mathrm{V}$. These can not be clearly identified to result from the third carrier species (see Ch. 4), since for high positive gate voltages a mixing between oscillations of different origin is setting in. An observation of oscillations at very low magnetic field has turned out to be complicated, presumably due to a higher roughness of samples with GaAs substrate (see Ref. [Ame15]). Therefore, an answer to the question if the back gate can change the

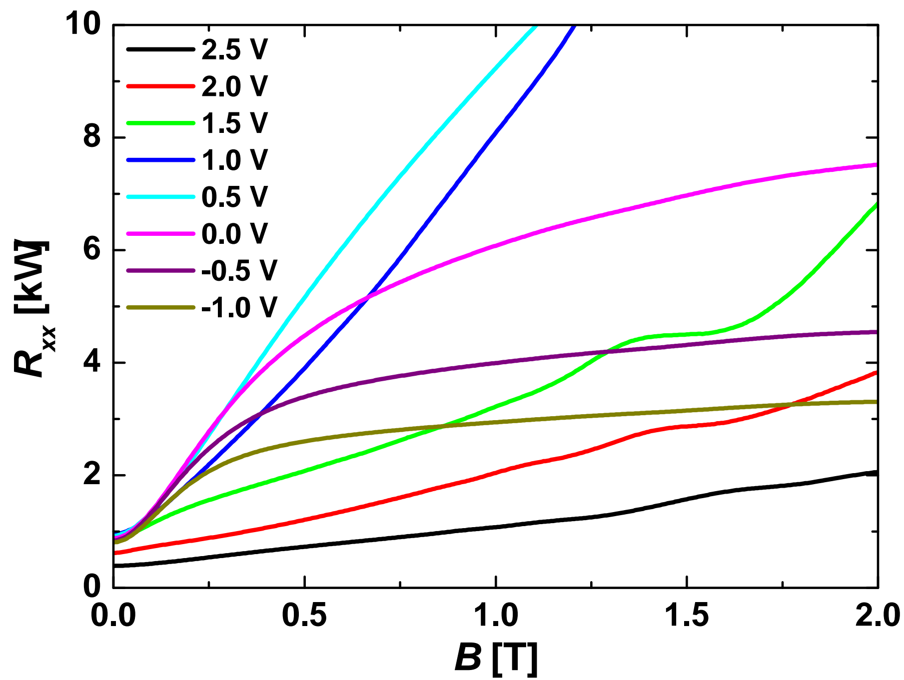

Fig. 5.7.: Longitudinal resistance of Q2780 for low magnetic field and different top gate voltages.

frequency of the low field oscillations remains wanting until a sample is available which is equipped with a back gate and where the low field oscillations are well resolved.

6. Surface Landau level spectrum and in-plane magnetic field

In the previous chapters the transport in strained HgTe Hall bar structures has been investigated for n-type as well as for p-type Dirac carriers. The influence of top and back gate electrode on the properties of the system has been demonstrated. Information has been gathered by interpreting the Landau levels that form in a finite magnetic field perpendicular to the largest two surface areas. In addition to probing the system one can ask, if the dispersion of these levels can be manipulated in an experiment. In this chapter the in-plane magnetic field is utilized as an additional parameter to influence the system. To generate these in-plane field components, a basic experimental technique, namely the rotation of the sample in a magnetic field, will be utilized to change the Landau level dispersion of the top and bottom surface states. A simple model qualitatively reproduces the observed features resulting from the in-plane field.

6.1. Hall resistance for rotated sample

A sample stick with the ability to rotate the sample in a magnetic field was already utilized in Ch. 4 for measurements in small magnetic fields. However, also for high field values the samples can be investigated in a magnetic field applied under different angles. Here, the notation that was introduced to describe Eq. 4.15 is retained, where α measures the angle between the surface normal and the magnetic field. For the 2D surface states one expects the Hall resistance to depend on the perpendicular component of the magnetic field only. At the high magnetic field laboratory in Nijmegen the sample Q2451$^{\mathrm{Nij}}$ was cooled to a temperature

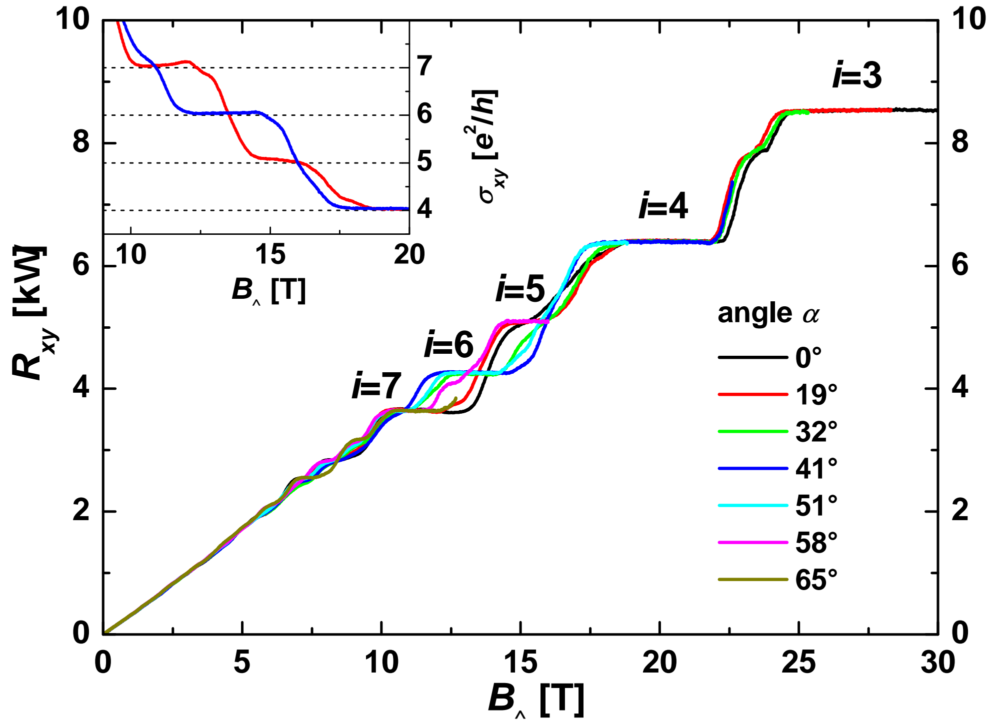

Fig. 6.1.: Hall resistance of Q2451[Nij] for different angles α between surface normal and magnetic field. As the abscissa the effective magnetic field perpendicular to the sample surface is calculated. The quantum Hall index i is indicated for the plateaus. Inset: Hall conductivity of the trace at $\alpha = 19°$ and $\alpha = 41°$, respectively.

of $T \approx 300\,\mathrm{mK}$ and measured at successively increased angle α. In Fig. 6.1 the resulting Hall traces are plotted against the effective magnetic field (see Eq. 4.15). One recognizes that indeed for low magnetic field the Hall traces have identical slopes. Also for higher magnetic field the traces coincide. However, the plateau sequence of traces measured at different angles α is different in the interval $7\,\mathrm{T} < B_\perp < 20\,\mathrm{T}$. Irregularities in the steps of the quantum Hall index for different top and bottom surface carrier densities have already been described above. If two Landau levels are energetically degenerate, by a change of the perpendicular magnetic field an increase of $\Delta i = 2$ might be found for neighbouring Hall plateaus (see Ch. 3). This is e.g. the case for the transition from the plateau at $i = 7$ to the plateau at $i = 5$ in the red trace ($\alpha = 19°$) in Fig. 6.1. For the blue trace the angle and, therefore, the in-plane field is different. At $\alpha = 41°$ one observes a strong plateau at $i = 6$, directly followed by $i = 4$ if the magnetic field is enhanced. To compare these two measurements in detail, a plot of σ_{xy} is presented in the inset of Fig. 6.1. Clearly the relative energetic position of at least some of the Landau levels is modified by a change of α, since the step sequence is altered. The

difference between the two measurements is the bigger in-plane component of the magnetic field at higher angle (at a given perpendicular magnetic field $B_\perp$). It is accompanied by an increased total magnetic field B, which can be understood from basic vector addition considerations. Thus, one can assume that the equation describing the Landau level spectrum for all angles contains a term proportional to either the total or the in-plane magnetic field.

6.2. Isotropic Zeeman contribution

In a first order explanation one can assume that the Zeeman contribution in Eq. 2.9 isotropically depends on the (total) magnetic field B, while the other term in the 2D Dirac spectrum only reacts to the effective field $B_\perp(\alpha) = B \cdot \cos(\alpha)$. Implementing these dependencies and following Ref. [BLN+11b] one finds

$$E^N = \pm\sqrt{2e\hbar v_F^2 B_\perp(\alpha)\, N + (g^* \mu_\mathrm{B} B)^2}\,,\; N = 1, 2, 3\ldots\,. \tag{6.1}$$

In this equation a constant effective field but changing total field will directly influence the energetic positions of the spectrum of a single Dirac cone. Note that the zero levels are excluded from the considerations, since they only see the Zeeman contribution (as described in the explanation of Eq. 2.9 for $N = 0$). In detail the levels are forced apart by the Zeeman contribution, since it increases the absolute value of the energy E^N for all levels with $N > 0$. However, the shift of the energetic positions of levels resulting from a single cone is not sufficient to explain the differing σ_{xy} traces in the inset of Fig. 6.1. Instead, the interplay of two sets of Landau levels is needed to explain the appearance of suppressed plateaus under addition of an in-plane field. The origin (i.e. the CNP) of these sets must lie at different energy values, which means that the corresponding 2DEGs need to have unequal carrier densities. If the two densities were equal, the degeneracy could not be lifted by the external field. In contrast to this, the crossing point of two levels with different individual Landau level indices will shift towards higher magnetic fields, if a Zeeman term is switched on for both levels.
To reproduce this, a minimalistic model is set up, that assumes $T = 0\,\mathrm{K}$ and a digital filling of Landau levels as soon as the condition $E_\mathrm{F} > E^N$ is fulfilled for a given level with index N. For each level that is filled, the Hall conductivity

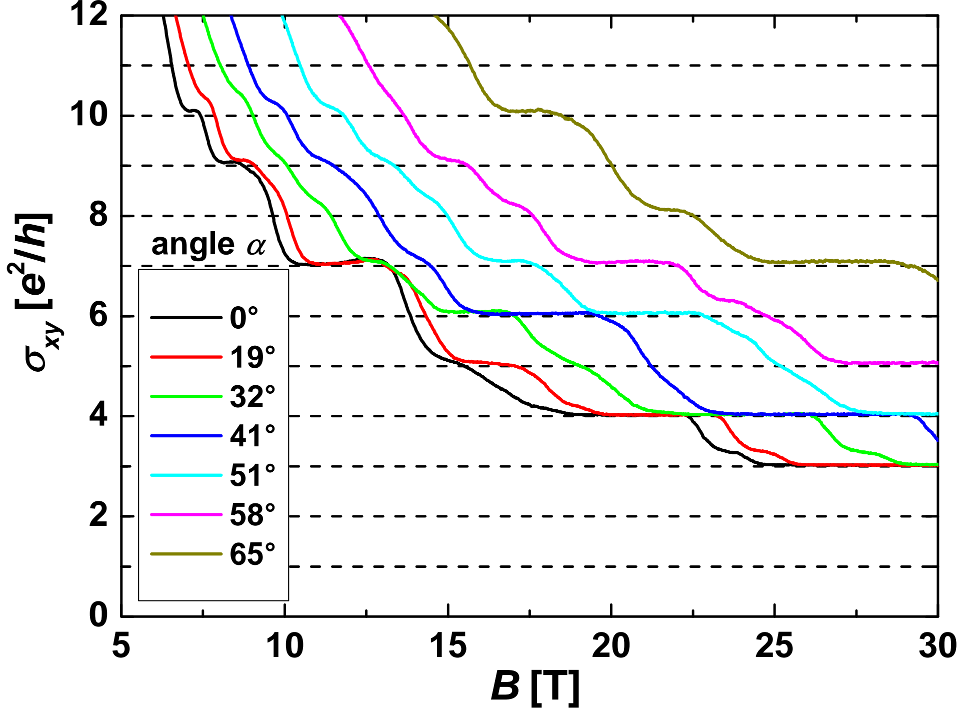

Fig. 6.2.: Hall conductivity of sample Q2451$^{\mathrm{Nij}}$. The magnetic field is applied under an angle α as indicated by the legend.

is increased by $\Delta\sigma_{xy} = e^2/h$ starting from $\sigma_{xy} = 2e^2/2h$ for the combined Hall conductivity of the two zero levels. Therefore, the outcome of the model is $\sigma_{xy}(B)$ for different angles, which can be compared to the experimental data. From the dataset the Hall conductivity for all angles is calculated and shown in Fig. 6.2. Here, the Hall conductivity is plotted against the total magnetic field B, because changes for plateaus at quantum Hall indices $i > 6$ can be demonstrated more clearly. For nearly all values of σ_{xy} the appearance or disappearance of a plateau can be observed along the line of constant σ_{xy}. In the model we assume the charge carrier densities to be $n_1 = 13.1 \cdot 10^{11}\,\mathrm{cm}^{-2}$ and $n_2 = 6.9 \cdot 10^{11}\,\mathrm{cm}^{-2}$, that add up to the total carrier density $n_{\mathrm{tot}} = 20 \cdot 10^{11}\,\mathrm{cm}^{-2}$, consistent with the slope of the Hall trace at low magnetic field.
For each Dirac system the energetic distance of the Fermi energy to the CNP individually is determined by the equation

$$E_{\mathrm{F}} - E_{\beta} = \hbar v_{\mathrm{F}}\, k_{\mathrm{F}} = \hbar v_{\mathrm{F}} \sqrt{4\pi n_{\beta}}, \tag{6.2}$$

where $\beta = 1, 2$ describes the different Dirac systems and $v_{\mathrm{F}} = 5 \cdot 10^5\,\mathrm{m/s}$ (value

motivated by Ref. [BLN+11b]) is assumed. Without loss of generality one can set $E_\mathrm{F} = 0$, since it is assumed to be constant. Therefore, the energetic dispersion for the two sets of n-type Landau levels can be written as

$$E_\beta^N = \sqrt{2e\hbar v_F^2 B_\perp(\alpha)\, N + (g^* \mu_\mathrm{B} B)^2} - E_\beta\,,\ N = 1, 2, 3\ldots\,, \tag{6.3}$$

where Eqs. 6.2 (for $E_\mathrm{F} = 0$) and 6.1 are combined. Motivated by the values found in Refs. [WCC95], [ZOPJ+04] and [BLT+10] and to obtain a strong effect in the qualitative model the effective g-factor is set to $g^* = 40$ in Eq. 6.3. From

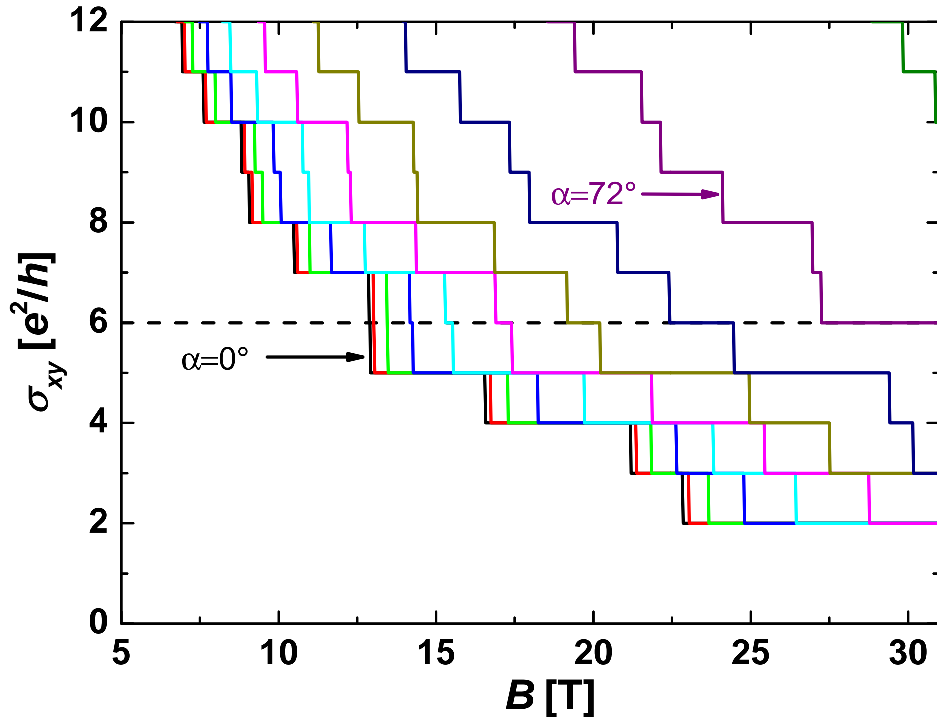

Fig. 6.3.: Modelled combined Hall conductivity of two topological surface states with charge carrier densities $n_1 \neq n_2$. The magnetic field is applied under an angle α which is increased in steps of $\Delta\alpha = 9°$. By the dashed line $\sigma_{xy} = 6\, e^2/h$ is highlighted.

Eq. 6.2 and the carrier densities n_1 and n_2 the energy shift between the two CNPs of the surfaces can be determined to be $E_1 - E_2 = 37\,\mathrm{meV}$. The combined Hall conductivity σ_{xy} is found as the number of all levels with $E_\beta^N < 0$, since $E_\mathrm{F} = 0$. This condition can be applied for all values of the magnetic field, such that $\sigma_{xy}(B)$ traces are found for different angles α. The Mathematica code is given in Appendix B.2. The resulting σ_{xy} traces are plotted in Fig. 6.3 in steps

of $\Delta\alpha = 9°$. It is clearly reproduced, that plateaus in σ_{xy} are missing for small angles and reappear for finite angle. An example is the plateau at $i = 6$ (see dashed line in Fig. 6.3) that becomes very strong at $B = 30\,\mathrm{T}$. Also consistent with the experiment is the behaviour of the neighbour plateau $i = 7$, that vanishes in the region, where $i = 6$ is most pronounced. Thus, the model is qualitatively describing the observed plateau changes well. A deviation from the data is evident from the minimal plateau value in σ_{xy} at maximum field. While the experiment yields $i = 3$ as the lowest plateau value, the simulation predicts $i = 2$. One reason might be a considerable error in n_{tot}, since the total carrier density can only be calculated reliably from the combined Hall response of two surface states for perfectly matched carrier mobilities, which we do not expect for this system. However, for $B = 10\,\mathrm{T}$ the experimental and theoretical trace both reach the $i = 7$-plateau for $\alpha = 0$. It can be deduced from this that especially for high magnetic fields deviations occur. One has to keep in mind that the simulated σ_{xy} is the result of an oversimplified model. For example does the value assumed for the g-factor influence the lowest plateau index. The model assumes $T = 0$ and a constant Fermi energy, while in the experiment the gate voltage and therefore the carrier density in the device is held constant. When adding a Zeeman contribution, the degeneracy of the Landau levels is unaffected. In case of a constant Fermi energy, at high magnetic fields Landau levels can be depleted by the Zeeman term due to an increased energy (reducing the lowest plateau value). In contrast, in the experiment a constant carrier density and Landau level degeneracy lead to a lowest plateau value that does not depend on the g-factor. It also has to be considered, that the model parameters are not measured, but assumed in a plausible way. Nevertheless, the model is able to demonstrate the observed change in the plateau sequence to possibly result from the isotropic Zeeman contribution with a high g-factor.

Summary

In the present thesis the transport properties of strained bulk HgTe devices are investigated. Strained HgTe forms a 3D TI and is of special interest for studying topological surface states, since it can be grown by MBE in high crystal quality. The low defect density leads to considerable mobility values, well above the mobilities of other TI materials. However, strained HgTe has a small band gap of ca. 20 meV. With respect to possible applications the question is important, under which conditions the surface transport occurs. To answer this question, the HgTe devices are investigated at dilution refrigerator temperatures in high magnetic fields of different orientation. The influence of top and back gate electrodes as well as surface protecting layers is discussed. On the basis of an analysis of the quantum Hall behaviour it is shown that transport is dominated by the topological surface states in a surprisingly large parameter range. A dependence on the applied top gate voltage is presented for the topological surface states. It enables the first demonstration of an odd integer QHE sequence from the surfaces perpendicular to the magnetic field. Furthermore, the p-type QHE from the surface states is observed for the first time in any 3D TI. This is achieved in samples of high surface quality. It is concluded from the gate response that the screening behaviour in 3D TI devices is non-trivial. The transport data are qualitatively analysed by means of intuitive theoretical models.
In intrinsically semi-metallic HgTe bulk crystals applied strain opens a gap in the bulk band structure. Combined with the inverted band structure of HgTe the requirements for a TI are fulfilled. The band structure details and the expected Landau level energy spectrum are covered in Ch. 2. After the discovery of the QHE from the surface states of strained HgTe [BLN+11a], the next generations of Hall bar devices, presented in this thesis, are designed with top or back gate electrodes as well as surface-protecting capping layers. These capping layers give rise to higher mean carrier mobilities and enhance the symmetry of the device. The use of a top gate electrode enables the control of the density mismatch between top and

bottom topological surface states, since the gate efficiency is different for these. Therefore, an odd integer sequence of quantum Hall plateaus can be presented in Ch. 3. This sequence is expected for a two-fold degenerate Dirac system with equal surface densities. The Dirac nature of carriers is sustained by an analysis of the Berry phase, that clearly yields a non-zero value. From the full gate dependent dataset two subsets of Landau levels can be identified, that confirm the existence of top and bottom surface state. Further, the unaltered quality of the Hall quantization even for high surface carrier densities represents the low bulk influence in transport. Therefore, a model of separated surfaces is used to fit the longitudinal resistance data, taking into account only transport through the topological states. Benefiting from improved surface mobilities due to HgCdTe capping layers it is demonstrated in Ch. 4 that the observed QHE has ambipolar nature. The gate dependent transition from quantum Hall plateaus of positive quantum Hall index to negative indices has not been reported before for any 3D TI. However, this is an expected feature for pure Dirac systems like the TI surface states, reflecting the gapless band structure. An analysis of the Berry phase and the presence of crossings in a Landau level fan chart confirm that the p-type QHE originates from the topological surface states. It is discussed how the p-type QHE can occur for large hole densities ($n \approx -10^{12}\,\mathrm{cm}^{-2}$ for an individual surface). Considering the small energy gap, the bulk valence band states for high p-type densities could be expected to pin the Fermi energy and to keep the density in the surface states constant. Since this is not observed, a simple model with artificially chosen potential is discussed. Within this model the surface states are shifted with respect to the bulk states, enabling the Fermi energy to reside in the bulk band gap, while the surface carrier densities are increased to high values. The band structure calculated in a $k \cdot p$ approach correctly describes the pronounced p-type QHE for large hole densities. However, since the potential is not computed self-consistently the description of the gating behaviour is not sufficient yet.

An interesting observation is the finite longitudinal resistance in the gate voltage region, where n- and p-type Landau levels coexist on top and bottom surface, respectively. It is suggested, that a recombination mechanism can take place via the conducting side surfaces, suppressing net current flow through the device.

An analysis of the low field ($B < 1\,\mathrm{T}$) behaviour especially for low surface carrier densities unveils further transport signatures. For the longitudinal and Hall-resistance an oscillating feature with top gate independent frequency is found. It can be attributed to a third carrier species with low density and high mobility. Since it is observed for many samples of different thickness and barrier material,

this n-type carrier species must be related to fundamental properties of strained HgTe. An angle-dependent measurement yields a 2D character for the additional carriers. Since the oscillating feature does not depend on the top gate voltage, this rises the question if the corresponding 2DEG is located at the lower HgTe interface. Therefore, it is interesting to study the influence of a back gate electrode onto the system. This is possible by the use of doped GaAs substrates, as presented in Ch. 5. At constant magnetic fields a pattern of two different species of Landau levels can be identified for a sample exposed to top and back gate electric fields. The screening properties of topological surface states are found to depend on the magnetic field and the quantum Hall index.
However, the low field oscillations can not be observed clearly in the investigated sample, such that the dependence on back gate voltage can not be determined. This issue can be addressed by future projects, if samples on GaAs substrates showing this feature become available. This would allow to test the hypothesis that the oscillations originate from the lower topological surface state or other 2D states below the HgTe. Another way of accessing the lower surface state exclusively could be an intentional degradation of the top surface by e.g. argon ion bombardment. Finally, tunnel contacts could enable contact to the top surface only. Combining the outcome of these suggested experiments, further insight to the different components of the multi carrier system could be achieved.
After analysing the Landau level spectrum in magnetic fields perpendicular to the top and bottom topological surface, it is shown that the effect of an additional in-plane magnetic field can be modelled by an isotropic Zeeman contribution. This contribution shifts the energetic position of all Landau levels and therefore can change the observed quantum Hall plateau sequence from the surface states. Therefore, the in-plane magnetic field is identified as a parameter to externally manipulate the spectrum of Dirac surface states.
In this thesis it is shown that strained bulk HgTe is a TI in which the transport is dominated by the surface states. The Dirac nature of the surface states is demonstrated and the p-type QHE is analysed for the first time in a 3D TI. The investigations of the HgTe properties enable further interesting experiments involving superconducting and magnetic proximity effects. However, some observations presented in this thesis require an explanation beyond the model of two non-interacting surface states. For the ongoing study of strained HgTe as a multi carrier system there are experiments suggested in this thesis that might clarify the open issues.

Zusammenfassung

In der vorliegenden Dissertation werden die Transporteigenschaften von verspannten HgTe-Volumenkristallen untersucht. Verspanntes HgTe stellt einen dreidimensionalen topologischen Isolator dar und ist zur Erkundung von topologischen Oberflächenzuständen von speziellem Interesse, da es mit Hilfe von Molekularstrahlepitaxie in hoher Kristallqualität gewachsen werden kann. Die niedrige Defektdichte führt zu beachtlichen Ladungsträgerbeweglichkeiten, die deutlich über denen anderer topologischer Isolatoren liegen. Verspanntes HgTe hat jedoch eine kleine Energielücke von ca. 20 meV. Deshalb ist es für eine mögliche Verwendung des Materials ein wichtiger Aspekt, in welchem Parameterbereich Oberflächentransport stattfindet. Um dieser Frage nachzugehen, werden die HgTe-Proben bei tiefen Temperaturen ($T < 100\,\mathrm{mK}$) und unter dem Einfluss hoher Magnetfelder in verschiedenen Orientierungen untersucht. Der Einfluss von Gate-Elektroden ober- und unterhalb der Struktur sowie von Deckschichten, die die Oberflächen schützen, wird diskutiert. Basierend auf einer Analyse des Quanten-Hall-Effekts wird gezeigt, dass der Transport in diesem Material von topologischen Oberflächenzuständen dominiert ist. Die Abhängigkeit der topologischen Oberflächenzustände von der Gate-Spannung wird dargestellt. Durch diese Abhängigkeit ist es zum ersten Mal möglich, eine ungerade ganzzahlige Quanten-Hall-Plateau Sequenz nachzuweisen, die von den Oberflächen senkrecht zum Magnetfeld stammt. Des Weiteren wird im Rahmen dieser Arbeit in Proben hoher Oberflächenqualität zum ersten Mal für einen 3D TI der p-Typ QHE der Oberflächenzustände beobachtet. Aus der Gate-Abhängigkeit der Messungen wird geschlossen, dass das Abschirmverhalten in 3D TIs nicht trivial ist. Die Transportdaten werden mit Hilfe von intuitiven theoretischen Modellen auf qualitative Weise analysiert.
In HgTe Volumenkristallen, welche ohne zusätzliche externe Einflussnahme halbmetallischen Charakter zeigen, öffnet eine Verspannung des Kristalls eine Bandlücke in der Volumen-Bandstruktur. Zusammen mit der invertierten Bandstruktur des HgTe werden damit die Voraussetzungen für einen topologischen Isolator er-

füllt. Eine detaillierte Darstellung der Bandstruktur sowie der erwartete Verlauf des Landau-Level-Spektrums werden in Kapitel 2 dargestellt. Nach der Entdeckung des QHE in den Oberflächenzuständen von verspanntem HgTe [BLN+11a] sind die weiterentwickelten Hallbar-Proben, die in dieser Arbeit diskutiert werden, um Gate-Elektroden (oberhalb und unterhalb der aktiven HgTe Schicht) sowie zusätzliche Deckschichten und damit einer erhöhten Symmetrie bezüglich der Barrieren ausgestattet. Durch eine Elektrode oberhalb der HgTe-Schicht kann der Unterschied in den Ladungsträgerdichten des oberen und unteren Oberflächenzustandes variiert werden, da diese unterschiedliche Gate-Effizienzen aufweisen. Damit ist es in Kapitel 3 möglich, die ungerade ganzzahlige Sequenz der Quanten-Hall-Plateaus nachzuweisen, die für ein zweifach entartetes Dirac-System (mit identischen Dichten auf beiden Oberflächen) erwartet wird. Das Dirac-artige Verhalten der Ladungsträger wird durch eine Analyse der Berry-Phase bestätigt, die deutlich von Null verschieden ist. In dem vollständigen Datensatz Gate-abhängiger Messungen können zwei Teilsysteme von Landau-Niveaus identifiziert werden, die die Existenz von oberem und unterem Oberflächenzustand verifizieren. Außerdem weist die auch für hohe Ladungsträgerdichten auf den Oberflächen unveränderte Qualität der Hall-Quantisierung auf einen geringen Anteil an Transport durch den Volumenkristall hin. Deshalb wird zur Beschreibung der Längswiderstandsdaten ein Modell zweier unabhängiger Oberflächen genutzt, das nur den Transport durch die topologischen Zustände berücksichtigt.
Durch gesteigerte Beweglichkeitswerte, die auf HgCdTe Deckschichten zurückzuführen sind, kann in Kapitel 4 gezeigt werden, dass der beobachtete QHE ein ambipolares Verhalten aufweist. Der Gate-abhängige Übergang von Quanten-Hall-Plateaus mit positivem Quanten-Hall-Index zu negativen Indices konnte bisher für keinen 3D TI nachgewiesen werden. Dies wird jedoch für reine Dirac-Systeme wie die Oberflächenzustände eines TIs erwartet und spiegelt die verschwindende Bandlücke wider. Eine Analyse der Berry-Phase und das Auftreten von Kreuzungen in einem Landau-Level-Diagramm bestätigen, dass der p-Typ QHE von den topologischen Oberflächenzuständen stammt. Es wird diskutiert, wie der p-Typ QHE für hohe Loch-Dichten ($n \approx -10^{12}\,\mathrm{cm}^{-2}$ für eine einzelne Oberfläche) auftreten kann. Zieht man die kleine Energielücke in Betracht, so könnte man erwarten, dass die Valenzbandzustände des Volumenkristalls die Fermi-Energie für große p-Typ Ladungsträgerdichten konstant halten und somit Änderungen der Oberflächenladungsträgerdichten verhindert werden. Da dies nicht beobachtet wird, wird ein einfaches Modell diskutiert, in dem das Potential in der Probe von Hand angepasst wird. Im Rahmen dieses Modells werden die Oberflächenzustände gegen

die Volumenbandstruktur verschoben, sodass die Fermi-Energie in der Volumen-Bandlücke verbleiben kann und zugleich die Oberflächen-Ladungsträgerdichten erhöht werden. Durch die Bandstrukturrechnung nach dem $k \cdot p$-Ansatz kann der ausgeprägte p-Typ QHE erklärt werden. Da das Potential allerdings nicht selbstkonsistent berechnet wird, ist diese Beschreibung des Gate-Verhaltens noch nicht ausreichend.
Eine interessante Beobachtung ist der endliche Längswiderstand in dem Bereich der Gatespannung, in dem ein n-Typ Landau-Niveau auf der oberen und ein p-Typ Landau-Niveau auf der unteren Oberfläche zugleich existieren. Als Erklärung wird vorgeschlagen, dass in diesem Fall Rekombination entlang der leitenden Seitenflächen stattfinden kann, die den Stromfluss durch die Probe unterdrückt.
Durch eine Analyse des Niedrig-Feld-Verhaltens ($B < 1\,\mathrm{T}$) speziell für niedrige Oberflächen-Ladungsdichten werden weitere Transport-Eigenschaften der HgTe-Proben aufgezeigt. Für den Längs- und Hallwiderstand findet man einen oszillierenden Anteil, dessen Frequenz von der oberen Gate-Elektrode unabhängig ist. Dieser kann qualitativ auf eine dritte Ladungsträger-Spezies mit niedriger Ladungsdichte und hoher Beweglichkeit zurückgeführt werden. Da die Oszillation für viele Proben mit unterschiedlichen Dicken und Barrieren-Materialien beobachtet wird, muss die n-Typ Ladungsträgerspezies mit fundamentalen Eigenschaften von verspanntem HgTe verknüpft sein. Eine winkelabhängige Messung zeigt, dass die zusätzlichen Ladungsträger wie ein 2DEG reagieren. Da die Oszillation nicht von der Spannung der oberen Gate-Elektrode abhängt, muss man sich fragen, ob das zugehörige 2DEG an der unteren HgTe Grenzschicht existiert. Deshalb ist es interessant, den Einfluss einer Gate-Elektrode zu untersuchen, die unterhalb des HgTe-Systems angebracht ist. Dies ist möglich, indem man ein dotiertes GaAs-Substrat nutzt, wie es in Kapitel 5 beschrieben ist. In einer Messung, in der die Probe dem elektrischen Feld zweier Elektroden ober- und unterhalb ausgesetzt ist, kann bei konstantem Magnetfeld ein Muster von zwei verschiedenen Arten von Landau-Niveaus identifiziert werden. Es wird außerdem gezeigt, dass die Abschirm-Eigenschaften der topologischen Oberflächenzustände vom Magnetfeld sowie dem Quanten-Hall-Index abhängen. Die Oszillationen für niedrige Magnetfelder können jedoch in dieser Probe nicht eindeutig beobachtet werden, sodass eine Abhängigkeit von der unteren Gate-Elektrode nicht untersucht werden kann. Diese Fragestellung kann von zukünftigen Projekten aufgegriffen werden, wenn Proben mit GaAs-Substrat verfügbar werden, die die Oszillationen deutlich aufweisen. So könnte die Hypothese überprüft werden, dass diese vom unteren topologischen Oberflächenzustand oder einem anderen 2DEG unterhalb der

HgTe-Schicht stammen. Eine andere Möglichkeit, den unteren Oberflächenzustand separat zu vermessen, könnte die gezielte Verschlechterung der Oberflächeneigenschaften des oberen Zustands sein, z.B. durch Argon-Ionen-Beschuss. Außerdem könnten möglicherweise Tunnelkontakte genutzt werden, um die obere Oberfläche des TI separat zu kontaktieren. Aus dem kombinierten Wissensgewinn durch diese vorgeschlagenen Experimente könnte ein weiterreichendes Verständnis des Systems mit mehreren Ladungsträgerarten gewonnen werden.
Nach der Analyse des Spektrums der Landau-Niveaus von oberem und unterem Oberflächenzustand im senkrechten magnetischen Feld wird gezeigt, dass der Einfluss eines zusätzlichen parallelen Magnetfelds durch einen isotropen Zeeman-Beitrag beschrieben werden kann. Dieser Beitrag verschiebt die energetische Position aller Landau-Niveaus und kann deshalb die beobachtete Sequenz der Quanten-Hall-Plateaus von den Oberflächenzuständen verändern. Demnach kann das parallele Magnetfeld als ein Parameter bestätigt werden, durch den das Spektrum der Dirac-Oberflächenzustände zusätzlich manipuliert werden kann.
In dieser Arbeit wird gezeigt, dass ein verspannter HgTe einen topologischen Isolator darstellt, in dem der Transport durch die Oberflächenzustände dominiert wird. Die Dirac-Physik der Oberflächenzustände wird gezeigt und es wird zum ersten Mal der p-Typ Quanten-Hall-Effekt in einem dreidimensionalen topologischen Isolator analysiert. Die Untersuchung der Eigenschaften von HgTe ermöglichen nachfolgende interessante Experimente, die supraleitende und magnetische Proximity-Effekte behandeln. Für einige Beobachtungen, die im Rahmen dieser Arbeit präsentiert werden, müssen jedoch auch Erklärungen gefunden werden, die über ein Modell von zwei nicht wechselwirkenden Oberflächen hinausgehen. Für weitere Untersuchungen von verspanntem HgTe als System mehrerer Ladungsträger werden in dieser Arbeit Experimente vorgeschlagen, die die zur Klärung der offenen Fragen beitragen können.

A. Sample overview

A list of all used samples with their relevant parameters is given here. Note that two different substrate types are used: The commercially available (001)-oriented CdTe substrates (called 'Nikko CdTe') and a highly n-doped GaAs substrate. In the latter the active HgTe structure is also strained to a_{CdTe}, since a thick layer of (001)-oriented CdTe that is relaxed is grown underneath. These samples allow for back gating if the GaAs substrate is contacted.
All samples are $600\,\mu$m $\times$ 200μm Hall bars. The addend $^{\mathrm{Nij}}$ is denoting samples, that had to be rebuilt and connected differently for measurement at the HFML in Nijmegen.
HgCdTe as part of the layer structure stands for $\mathrm{Hg}_{1-x}\mathrm{Cd}_x\mathrm{Te}$ with $x = 0.7$, which is a direct semiconductor with an energy gap of $\Delta E \approx 1\,\mathrm{eV}$ [BK11].

Sample	Substrate	Layer structure	Layer thicknesses [nm]
Q2424	Nikko CdTe	CdTe/HgTe/insulator	substrate/70/110
Q2451_2	Nikko CdTe	CdTe/HgTe/insulator	substrate/128/110
Q2761	Nikko CdTe	HgCdTe/HgTe/HgCdTe	50/90/10
Q2763	Nikko CdTe	HgCdTe/HgTe/HgCdTe	50/111/13
Q2584$^{\mathrm{Nij}}$	Nikko CdTe	HgCdTe/HgTe/HgCdTe	100/60/5
Q2584	Nikko CdTe	HgCdTe/HgTe/HgCdTe	100/60/5
Q2451	Nikko CdTe	CdTe/HgTe/insulator	substrate/128/110
Q2780	GaAs:Si	HgCdTe/HgTe/HgCdTe	45/75/4
Q2451$^{\mathrm{Nij}}$	Nikko CdTe	CdTe/HgTe/insulator	substrate/128/110

Tabelle A.1.: List of all samples described in this thesis. Layers denoted by substrate are thicker than 500 μm. Insulator layers are $\mathrm{SiO_2/Si_3N_4}$ multilayer stacks.

B. Mathematica code

B.1. DOS calculation

This code (see [Nov10]) calculates the DOS pattern for a Dirac 2DEG. It is written in unusual units to avoid very small numerical values and to enable the convergence of FindRoot. All length scales are given in nm, energies in meV. The variable Kb stands for the Boltzmann constant in these units, while lb $= \sqrt{\hbar/e}$.

$A = 280;$

$\mathrm{n2DEG} = -3.7\,10^{-3};$

$T = 1;$

$\mathrm{Kb} = 0.086173343323;$

$\mathrm{lb} = 25.6557461261;$

$\mathrm{nmax} = 50;$

$\mathrm{G0} = 1.0;$

$\mathrm{nB} = 600; \mathrm{Bi[i_]}{:=}1 + i/40;$

$G[\mathrm{Bi_}]{:=}\mathrm{G0}\sqrt{\mathrm{Bi}};$

$\mathrm{Ec}[\mathrm{n_}, \mathrm{Bi_}]{:=}A\sqrt{0.00304\mathrm{Bi}n};$

$\mathrm{Ev}[\mathrm{n_}, \mathrm{Bi_}]{:=} - A\sqrt{0.00304\mathrm{Bi}n};$

$\mathrm{fermi}[\mathrm{En_}, \mathrm{Ef_}]{:=}$

$\mathrm{Module}\left[\{x\}, x = \mathrm{Which}\left[\frac{\mathrm{En}-\mathrm{Ef}}{\mathrm{Kb}T} > 300, 300, \frac{\mathrm{En}-\mathrm{Ef}}{\mathrm{Kb}T} < -300, -300, \mathrm{True}, \frac{\mathrm{En}-\mathrm{Ef}}{\mathrm{Kb}T}\right];\right.$

$\frac{1}{1+\text{Exp}[x]}\Big]$;

$\text{filfac[Bi_]:=Floor}\left[2\pi \text{lb}^2\text{Abs[n2DEG]/Bi}\right]$;

$\text{Gauss[En_, Ef_, Bi_]:=}\frac{1}{\sqrt{\pi}G[\text{Bi}]}\text{Exp}\left[-\left(\frac{\text{En}-\text{Ef}}{G[\text{Bi}]}\right)^2\right]$;

GaussFermi[En_, Ef_, Bi_]:=

$\frac{1}{\sqrt{\pi}G[\text{Bi}]}\int_{\text{En}-6G[\text{Bi}]}^{\text{En}+6G[\text{Bi}]}\text{Exp}\left[-\left(\frac{\text{Ei}-\text{En}}{G[\text{Bi}]}\right)^2\right]\text{fermi[Ei, Ef]}d\text{Ei}$;

GaussFermiS[En_, Ef_, Bi_]:=

$\frac{12/180}{\sqrt{\pi}}\sum_{i=0}^{180}\text{Exp}\left[-\left(\frac{1}{G[\text{Bi}]}((\text{En}-6G[\text{Bi}]+i12G[\text{Bi}]/180)-\text{En})\right)^2\right]$

$\text{fermi}[(\text{En}-6G[\text{Bi}]+i12G[\text{Bi}]/180),\text{Ef}]$;

density[Ef_, Bi_]:=

$\frac{\text{Bi}}{2\pi\text{lb}^2}\left(-\frac{(2\text{fermi}[\text{Ec}[0,\text{Bi}],\text{Ef}]-1)}{2}-\sum_{n=1}^{\text{nmax}}\text{fermi}[\text{Ec}[n,\text{Bi}],\text{Ef}]\right)$;

$\text{Efermi}=\text{Table}[i,\{i,1,\text{nB}\}]$;

Do[

$\text{Efermi}[[i]]=$

$\text{Ef/.FindRoot}[(\text{n2DEG}-\text{density}[\text{Ef},\text{Bi}[i]])==0,$

$\left\{\text{Ef},0,\left(A\sqrt{0.00304\ 2\pi\text{lb}^2\text{Abs[n2DEG]}}\right)\right\}\Big],\{i,1,\text{nB}\}\Big];\text{Efermi}[[1]]//N$

densityG[Ef_, Bi_]:=

$\frac{\text{Bi}}{2\pi\text{lb}^2}\Big(-\frac{1}{2}(2\text{GaussFermiS}[\text{Ec}[0,\text{Bi}],\text{Ef},\text{Bi}]-1)-$

$\sum_{n=1}^{\text{nmax}}\text{GaussFermiS}[\text{Ec}[n,\text{Bi}],\text{Ef},\text{Bi}]\Big)$;

$\text{EfermiG}=\text{Table}[i,\{i,1,\text{nB}\}]$;

Do[

$\text{EfermiG}[[i]]=$

$\text{Ef/.FindRoot}[(\text{n2DEG}-\text{densityG}[\text{Ef},\text{Bi}[i]])==0,$

$\{\text{Ef},\text{Efermi}[[i]]-5,\text{Efermi}[[i]]+5\}],\{i,1,\text{nB}\}]$;

```
DOS[Ef_, Bi_]:= Bi/(2π lb^2) (Sum_{n=0}^{nmax} Gauss[Ec[n, Bi], Ef, Bi]) ;
```

```
ListLinePlot[Table[Table[{Bi[i], f}, {i, 1, nB, 1}],
{f, {Efermi[[i]], EfermiG[[i]],
 Ec[0, Bi[i]],  Ec[1, Bi[i]],  Ec[2, Bi[i]],  Ec[3, Bi[i]],
Ec[4, Bi[i]],  Ec[5, Bi[i]],  Ec[6, Bi[i]],  Ec[7, Bi[i]],
Ec[8, Bi[i]],  Ec[9, Bi[i]],
 Ec[10, Bi[i]], Ec[11, Bi[i]], Ec[12, Bi[i]], Ec[13, Bi[i]],
Ec[14, Bi[i]], Ec[15, Bi[i]], Ec[16, Bi[i]], Ec[17, Bi[i]],
Ec[18, Bi[i]], Ec[19, Bi[i]],
 Ec[20, Bi[i]], Ec[100, Bi[i]]} }],
 PlotRange → {−5, 100}, Frame → True, Axes → False,
FrameLabel → {B, “E (meV)”}]
```

```
ListLinePlot[Table[{Bi[i], filfac[Bi[i]]}, {i, 1, nB}], PlotRange → {0, 20},
Frame → True, Axes → False, FrameLabel → {B, “filling factor”}]
```

```
ListLinePlot[Table[{Bi[i], DOS[EfermiG[[i]], Bi[i]]}, {i, 1, nB}],
Frame → True, Axes → False, FrameLabel → {B, “DOS”}]
```

```
Export[“out.dat”, Table[{N[Bi[i]], DOS[EfermiG[[i]], Bi[i]]}, {i, 1, nB}]] ;
```

B.2. Hall conductivity in rotated magnetic field

The small Mathematica code presented here is based on the code by A. Novik and is a simplified version, that uses SI units. It outputs the Hall conductivity of two TI surfaces for several angles of the magnetic field and $T = 0$.

```
ClearAll["Global`*"]

(*Constants*)
n2DEG = 13.1 * 10^15;
nDC1 = 6.9 * 10^15;
nDC2 = n2DEG − nDC1;
g = 40;
el = ElectronCharge[[1]];
v_F = 5 * 10^5;
hbar = PlanckConstantReduced[[1]];
μ = −ElectronMagneticMoment[[1]];

(*Fermi wave vektor*)
k_F[n2D_] = √(4πn2D);

(*Fermi energy*)
E_F[n2D_] = hbar * v_F * k_F[n2D];

(*Distance of the Dirac cones to the Fermi energy*)
(*Assumption : linear dispersion → E = A × k*)
E01 = E_F[nDC1];
E02 = E_F[nDC2];
```

```
(*Landau levels of Dirac cone including Zeeman contribution*)

EL[B_, α_, n_, Es_]:=If[n == 0, −gμB − Es,
√(2 ∗ el ∗ hbar ∗ v_F^2 ∗ B ∗ Cos[α] ∗ n + (gμB)^2) − Es];

(*discretizeB − field*)

Bi[u_] = 1 + u/40;

sigmaxy = Array[sig, 10];

For[l = 1, l < 11, l++,
fillfac1 = Array[f, 1199];
fillfac2 = Array[h, 1199];
For[i = 0, i < 1200, i++,
k = 0; f[i] = k − 1/2; While[EL[Bi[i], 90° − l ∗ 9°, k, E01] < 0, k++; f[i] = k − 1/2]];
For[i = 0, i < 1200, i++,
k = 0; h[i] = k − 1/2; While[EL[Bi[i], 90° − l ∗ 9°, k, E02] < 0, k++; h[i] = k − 1/2]];
sig[l] = Table[{Bi[i], f[i] + h[i]}, {i, 0, 1199}]; ]

Export[angle_all.dat, N[Flatten/@Transpose[sigmaxy]]];

ListLinePlot [sigmaxy,PlotRange → {{5,30},{0,12}},Frame → True,
FrameLabel → { "B / T","σxy  / e/h" },
PlotStyle -> {Magenta,Pink,Cyan,Gray,Purple,Red,Green,Blue,Black, Navy}]
```

Bibliography

[Ada11] S. Adachi. *in: Mercury Cadmium Telluride (eds P. Capper and J. W. Garland), p. 51.* John Wiley and Sons, LTD., Chichester (2011).

[AFS82] T. Ando, A. B. Fowler, and F. Stern. Electronic properties of two-dimensional systems. *Reviews of Modern Physics*, **54**, 437 (1982).

[Ame15] C. Ames. Dissertation, Würzburg, to be published (2015).

[BBB+14] Y. Baum, J. Böttcher, C. Brüne, C. Thienel, L. W. Molenkamp, A. Stern, and E. M. Hankiewicz. Self-consistent $k \cdot p$ calculations for gated thin layers of 3D Topological Insulators. *Physical Review B*, **89**, 245136 (2014).

[BF89] G. Bahir and E. Finkmann. Ion beam milling effect on electrical properties of $Hg_{1-x}Cd_xTe$. *Journal of Vacuum Science & Technology A: Vacuum, Surfaces, and Films*, **7**, 348 (1989).

[BHG+94] E. Belas, P. Höschl, R. Grill, J. Franc, P. Moravec, K. Lischka, H. Sitter, and A. Toth. Ultrafast diffusion of Hg in $Hg_{1-x}Cd_xTe$ ($x \approx 0.21$). *Journal of Crystal Growth*, **138**, 940 (1994).

[BHZ06] B. A. Bernevig, T. L. Hughes, and S.-C. Zhang. Quantum spin Hall effect and topological phase transition in HgTe quantum wells. *Science*, **314**, 1757 (2006).

[BK11] C. R. Becker and S. Krishnamurthy. *in: Mercury Cadmium Telluride (eds P. Capper and J. W. Garland), p. 275.* John Wiley and Sons, LTD., Chichester (2011).

[BLN+11a] C. Brüne, C. X. Liu, E. G. Novik, E. M. Hankiewicz, H. Buhmann, Y. L. Chen, X. L. Qi, Z. X. Shen, S. C. Zhang, and L. W. Molenkamp. Quantum Hall Effect from the Topological Surface States of Strained Bulk HgTe. *Physical Review Letters*, **106**, 126803 (2011).

[BLN+11b] C. Brüne, C. X. Liu, E. G. Novik, E. M. Hankiewicz, H. Buhmann, Y. L. Chen, X. L. Qi, Z. X. Shen, S. C. Zhang, and L. W. Molenkamp. Quantum Hall Effect from the Topological Surface States of Strained Bulk HgTe, supplementary online material. *Physical Review Letters*, **106**, 126803 (2011).

[BLT+10] B. Büttner, C. X. Liu, G. Tkachov, E. G. Novik, C. Brüne, H. Buhmann, E. M. Hankiewicz, P. Recher, B. Trauzettel, S. C. Zhang, and L. W. Molenkamp. Single valley Dirac fermions in zero-gap HgTe quantum wells. *Nature Physics*, **7**, 418 (2010).

[BP74] G. Bir and G. Pikus. *Symmetry and strain-induced effects in semiconductors*. John Wiley and Sons, LTD., Chichester (1974).

[BvH91] C. W. J. Beenakker and H. van Houten. Quantum Transport in Semiconductor Nanostructures. *Solid State Physics*, **44**, 1 (1991).

[COB+13] O. Crauste, Y. Ohtsubo, P. Ballet, P. Delplace, D. Carpentier, C. Bouvier, T. Meunier, A. Taleb-Ibrahimi, and L. L. P. Topological surface states of strained Mercury-Telluride probed by ARPES. *arXiv preprint arXiv:1307.2008*, 1–5 (2013).

[CPNG09] A. H. Castro Neto, N. M. R. Peres, K. S. Novoselov, and A. K. Geim. The electronic properties of graphene. *Reviews of Modern Physics*, **81**, 109 (2009).

[CS75] R. Cottam and G. Saunders. The elastic behaviour of mercury telluride. *Journal of Physics and Chemistry of Solids*, 187–192 (1975).

[CSB+85] Y.-C. Chang, J. N. Schulman, G. Bastart, Y. Guldner, and M. Voos. Effects of quasi-interface states in HgTe-CdTe superlattices. *Physical Review B*, **31**, 2557 (1985).

[CSLS11] R.-L. Chu, W.-Y. Shan, J. Lu, and S.-Q. Shen. Surface and edge states in topological semimetals. *Physical Review B*, **83**, 075110 (2011).

[CWC+72] D. J. Chadi, J. P. Walter, M. L. Cohen, Y. Petroff, and M. Balkanski. Reflectivities and Electronic Band Structures of CdTe and HgTe. *Physical Review B*, **5**, 3058 (1972).

[DHQ+08] X. Dai, T. Hughes, X.-L. Qi, Z. Fang, and S.-C. Zhang. Helical edge and surface states in HgTe quantum wells and bulk insulators. *Physical Review B*, **77**, 125319 (2008).

[ESSP+93] V. H. Etgens, M. Sauvage-Simkin, R. Pinchaux, J. Massies, N. Jedrecy, A. Waldhauer, S. Tatarenko, and P. H. Jouneau. ZnTe/GaAs (001): growth mode and strain evolution during the early stages of molecular-beam-epitaxy heteroepitaxial growth. *Physical Review B*, **47** (1993).

[FK07] L. Fu and C. L. Kane. Topological insulators with inversion symmetry. *Physical Review B*, **76**, 045302 (2007).

[FK08] L. Fu and C. L. Kane. Superconducting Proximity Effect and Majorana Fermions at the Surface of a Topological Insulator. *Physical Review Letters*, **100**, 096407 (2008).

[FKM07] L. Fu, C. Kane, and E. Mele. Topological Insulators in Three Dimensions. *Physical Review Letters*, **98**, 106803 (2007).

[FS83] F. F. Fang and P. J. Stiles. Quantized magnetoresistance in two-dimensional electron systems. *Physical Review B*, **27**, 6487 (1983).

[FSW88] F. F. Fang, T. P. Smith III, and S. L. Wright. Landau-level broadening and scattering time in modulation doped GaAs/AlGaAs heterostructures. *Surface Science*, **196**, 310 (1988).

[FT22] M. Faraday and J. Tyndall. *Experimental Researches in Electricity*. J. M. Dent & Sons, London (1922).

[Ger76] R. R. Gerhardts. Cumulant approach to the two-dimensional magneto-conductivity problem. *Surface Science*, **58**, 227 (1976).

[HBS+06] J. Hinz, H. Buhmann, M. Schäfer, V. Hock, C. R. Becker, and L. W. Molenkamp. Gate control of the giant Rashba effect in HgTe quantum wells. *Semiconductor Science and Technology*, **21**, 501 (2006).

[HK10] M. Z. Hasan and C. L. Kane. Topological insulators. *Reviews of Modern Physics*, **82**, 3045 (2010).

[HQW+08] D. Hsieh, D. Qian, L. Wray, Y. Xia, Y. S. Hor, R. J. Cava, and M. Z. Hasan. A topological Dirac insulator in a quantum spin Hall phasel. *Nature*, **452**, 970 (2008).

[HXW+09] D. Hsieh, Y. Xia, L. Wray, D. Qian, A. Pal, J. H. Dil, J. Osterwalder, F. Meier, G. Bihlmayer, C. L. Kane, Y. S. Hor, R. J. Cava, and M. Z. Hasan. Observation of Unconventional Quantum Spin Textures in Topological Insulators. *Science*, **323**, 919 (2009).

[Jac75] J. D. Jackson. *Classical electrodynamics*. John Wiley and Sons, LTD., New York (1975).

[KDP80] K. v. Klitzing, G. Dorda, and M. Pepper. New Method for High-Accuracy Determination of the Fine-Structure Constant Based on Quantized Hall Resistance. *Physical Review Letters*, **45**, 494 (1980).

[Kit03] A. Y. Kitaev. Fault-tolerant quantum computation by anyons. *Annals of Physics*, **303**, 2 (2003).

[KOWV76] A. Kozacki, S. Otmezguine, G. Weill, and C. Verie. *Quantum transport properties associated with resonant acceptor states in zero-gap HgCdTe alloys. in: Physics of Semiconductors - Proceedings of the 13th international conference, p. 467.* North-Holland Publishing Company, Rome (1976).

[KS05] E. Kooi and A. Schmitz. *in: High dielectric constant materials (eds H. R. Huff and D. C. Gilmer), p. 54.* Springer, Berlin (2005).

[KWB+07] M. König, S. Wiedmann, C. Brüne, A. Roth, H. Buhmann, L. W. Molenkamp, X.-L. Qi, and S.-C. Zhang. Quantum Spin Hall Insulator State in HgTe Quantum Wells. *Science*, **318**, 766 (2007).

[LG94] K. Lier and R. R. Gerhardts. Self-consistent calculations of edge channels in laterally confined two-dimensional electron systems. *Physical Review B*, **50**, 7757 (1994).

[MDF11] M. Martyniuk, J. M. Dell, and L. Faraone. *in: Mercury Cadmium Telluride (eds P. Capper and J. W. Garland), p. 153.* John Wiley and Sons, LTD., Chichester (2011).

[NGM+04] K. S. Novoselov, A. K. Geim, S. Morozov, D. Jiang, Y. Zhang, S. V. Dubonos, I. V. Grigorieva, and A. A. Firsov. Electric Field Effect in Atomically Thin Carbon Films. *Science*, **306**, 666 (2004).

[NGM+05] K. S. Novoselov, A. K. Geim, S. V. Morozov, D. Jiang, M. I. Katsnelson, I. V. Grigorieva, S. V. Dubonos, and A. A. Firsov. Two-dimensional gas of massless Dirac fermions in graphene. *Nature*, **438**, 197 (2005).

[Nov10] A. Novik. Code was developed by A. Novik (2010).

[Nye57] J. F. Nye. *Physical properties of crystals.* Oxford University Press, Oxford (1957).

[Pan90] O. A. Pankratov. Electronic properties of band-inverted heterojunctions: supersymmetry in narrow-gap semiconductors. *Semiconductor Science and Technology*, **5**, 204 (1990).

[QZ11] X.-L. Qi and S.-C. Zhang. Topological insulators and superconductors. *Rev. Mod. Phys.*, **83**, 1057 (2011).

[SDC+79] H. L. Störmer, R. Dingle, A. C. Cossard, W. Wiegmann, and M. D. Sturge. Two-dimensional eletron gas at a semiconductor-semiconductor interface. *Solid State Communications*, **29**, 705 (1979).

[SHDN96] M. Schenk, I. Hähnert, L. T. H. Duong, and H.-H. Niebsch. Validity of the Lattice-Parameter Vegard-Rule in $Cd_{1-x}Zn_xTe$ Solid Solutions. *Crystal Research and Technology*, **31**, 665 (1996).

[TA11] A. A. Taskin and Y. Ando. Berry phase of non-ideal Dirac fermions in topological insulators. *Physical Review B*, **84**, 6 (2011).

[TKNdN82] D. J. Thouless, M. Kohmoto, M. P. Nightingale, and M. den Nijs. Quantized Hall Conductance in a Two-Dimensional Periodic Potential. *Physical Review Letters*, **49**, 405 (1982).

[TOT79] K. Takita, K. Onabe, and S. Tanaka. Anomalous magnetoresistance and band crossing in uniaxially compressed HgTe. *physica status solidi (b)*, **297** (1979).

[WCC95] M. Willatzen, M. Cardona, and N. E. Christensen. Spin-orbit coupling parameters and electron g factor of II-VI zinc-blende materials. *Physical Review B*, **51**, 17992 (1995).

[Wei81] M. H. Weiler. *in: Semiconductors and semimetals, Volume 16 (eds R. K. Willardson and A. C. Beer), p.119.* Academic Press, New York (1981).

[WGG88] U. Wulf, V. Gudmundsson, and R. Gerhardts. Screening properties of the two-dimensional electron gas in the quantum Hall regime. *Physical Review B*, **38**, 4218 (1988).

[Wie13] J. Wiedenmann. Quanten-Hall-Effect eines relativistischen Systems. Master thesis, Würzburg (2013).

[Zim60] J. M. Ziman. *Electrons and phonons.* Oxford University Press, Oxford (1960).

[ZOPJ$^+$04] X. C. Zhang, K. Ortner, A. Pfeuffer-Jeschke, C. R. Becker, and G. Landwehr. Effective g factor of n-type HgTe/$Hg_{1-x}Cd_xTe$ single quantum wells. *Physical Review B*, **69**, 115340 (2004).

[ZYF$^+$11] W. Zhang, R. Yu, W. Feng, Y. Yao, H. Weng, X. Dai, and Z. Fang. Topological Aspect and Quantum Magnetoresistance of β-Ag_2Te. *Physical Review Letters*, **106**, 156808 (2011).

List of publications

Full papers - published

* BACKSCATTERING OF DIRAC FERMIONS IN HGTE QUANTUM WELLS WITH A FINITE GAP.
  G. Tkachov, **C. Thienel**, V. Pinneker, B. Büttner, C. Brüne, H. Buhmann, L. W. Molenkamp, and E. M. Hankiewicz,
  Physical Review Letters **106**, 076802 (2011).

* SELF-CONSISTENT K·P CALCULATIONS FOR GATED THIN LAYERS OF 3D TOPOLOGICAL INSULATORS.
  Y. Baum, J. Böttcher, C. Brüne, **C. Thienel**, L. W. Molenkamp, A. Stern, and E. M. Hankiewicz,
  Physical Review B **89**, 245136 (2014).

Manuscripts in preparation

* DIRAC-SCREENING STABILIZED SURFACE-STATE TRANSPORT IN A TOPOLOGICAL INSULATOR.
  C. Brüne, **C. Thienel**, M. Stuiber, J. Böttcher, H. Buhmann, E. G. Novik, C.-X. Liu, E. M. Hankiewicz, and L.W. Molenkamp,
  Manuscript accepted by *Physical Review X* (06.11.2014), arXiv:1407.6537.

* AMBIPOLAR DIRAC FERMION TRANSPORT IN HIGH MOBILITY STRAINED BULK HGTE.
  C. Thienel, S. Wiedmann, J. Wiedenmann, A. Jost, F. Chiappini, C. Brüne, C. Ames, J. Böttcher, E. M. Hankiewicz, U. Zeitler, J.-C. Maan, H. Buhmann, and L.W. Molenkamp,
  Manuscript in preparation.

* TEMPERATURE-DRIVEN TRANSITION FROM A SEMICONDUCTOR TO A TOPOLOGICAL INSULATOR.
S. Wiedmann, A. Jost, **C. Thienel**, C. Brüne, P. Leubner, H. Buhmann, L.W. Molenkamp, J. C. Maan, and U. Zeitler,
Manuscript in preparation.

Acknowledgements

Finally, I want to thank everyone who contributed to the success of this work. My thanks go to

- Prof. Dr. Hartmut Buhmann for giving me the opportunity to work in his Quantum Transport group and for supervising my doctoral dissertation.
- Prof. Dr. Laurens W. Molenkamp for accepting me at his chair of Experimental Physics III,
- Christoph Brüne for many discussions about the properties of 3DTIs,
- Philipp Leubner and Christopher Ames for the growth of a variety of samples,
- Jonas Wiedenmann, Linus Elsässer, David Mahler, Thomas Khouri, Johannes Mutterer and Mirko Trabel for their work as Master students,
- Jan Böttcher, Yuval Baum, Dr. Alena Astakhova, Prof. Dr. Ady Stern and Prof. Dr. Ewelina M. Hankiewicz for band structure calculations,
- Steffen Wiedmann for the nice time at the HFML in Nijmegen and his patience during the publication process,
- Roland Ebert and Cornelius Ziga for the supply with helium and sharing their knowledge on cryostat technology,
- Holger Thierschmann, Luis Maier, Philipp Leubner and Rebekka Pfeuffer for daily ice cream and Klugscheiße,

- All members of the Quantum Transport group and most other members of EPIII for a good work climate.

Special thanks go to my family that always showed interest in my work and supported me in many ways.